UNIVERSITÀ
DI PAVIA

FACULTY OF ENGINEERING

Department of Electrical, Computer and Biomedical Engineering

Ph.D. School in Micoelectronics
Cycle XXXIII

Integrated Interface Circuits for MEMS Contact-less Temperature Sensors

Supervisors:
Prof. Edoardo Bonizzoni
Prof. Piero Malcovati

Ph.D Coordinator:
Prof. Piero Malcovati

Ph.D. thesis of
Elisabetta Moisello

Academic Year 2020/2021

Acknowledgements

First of all I want to thank my supervisors, Prof. Edoardo Bonizzoni and Prof. Piero Malcovati, for their patience, their guidance, and most of all for the opportunities they have given me: I tried and will continue to try my best to deserve the trust they have placed in me. In particular, I want to thank Edo for his inspiring attitude towards research, towards teaching and towards colleagues: I can only hope that it rubbed off on me at least a little and that I will be able to follow his example; and I want to thank Piero for his practical approach and for the way he always almost immediately proposes a solution when a problem is encountered: I hope someday to be able to perform problem solving with the same immediacy.

Then, of course, my gratitude goes to the people in STMicroelectronics and TODOS/Technion: without their cooperation this work would not have been possible. In particular I want to thank Yael Nemirovsky and her group, Sandro Dalle Feste, Giuseppe Bruno, Michele Vaiana, Maria Eloisa Castagna, Rosario Cariola, Antonella La Malfa, Angelo Recchia, Antonio Farruggia, Pierpaolo Lombardo, Germano Nicollini and Daniele De Vecchi, and all the people who have made me feel welcomed during my visits to ST Catania.

Furthermore, I want to thank Prof. Franco Maloberti for the opportunity he has given me to be involved in IEEE and the CAS Society.

My Ph.D. experience would not have been the same without the colleagues from the IMS Lab, who have increasingly become more like friends and family: for this I have to thank Edo again, Ale, Philippo, Antonio, Phlavio, Riccardo, Alper, Mac, Nico, Arun, Yilkal, Waqar, the latest additions and the guests we had along the way. I will always be fond of memories from “mas fuertate”, “pheste”, “mondiali” and “male male nights” and I look forward to creating new ones.

I then, of course, want to thank my (other) friends and my family for always being there, rejoicing with me when things went well and putting up with me when I got a little obsessed when things went less well. In particular, I want to thank my parents, whose constant support has made me able to pursue the

career I truly desired.

Contents

Introduction **1**

1 Integrated contact-less temperature sensors **3**
1.1 Bolometers 3
1.2 Pyroelectric detectors 4
1.3 Thermopiles 6
1.3.1 Thermopile theoretical model 7
1.3.2 Thermopile *Cadence* model 9
1.4 TMOS 11
1.4.1 TMOS theoretical model 12
1.4.2 TMOS *Cadence* model 14

2 Integrated micromachined thermopile **18**
2.1 Thermopile characterization measurements 22

3 Thermopile sensor readout circuit **27**
3.1 Readout circuit description 27
3.2 Readout circuit measurement results 32
3.3 Sensor-readout circuit system measurements 39
3.3.1 Fever measurement application 41
3.3.2 Presence and motion detection application 47

4 TMOS sensor **57**
4.1 TMOS configuration analysis 57
4.2 TMOS bias circuit 62
4.3 TMOS characterization measurements 64

5 TMOS readout circuit **70**
5.1 Readout circuit description 70
5.2 Readout circuit measurement results 73

5.3 Sensor-readout circuit system measurement results 76
5.3.1 Fever measurement application 77
5.3.2 Presence and motion detection application 83

Conclusions **87**

Bibliography **90**

List of Figures

1.1 Conceptual representation of a pyroelectric material. 5
1.2 Conceptual representation of a thermocouple. 6
1.3 Conceptual representation of a micromachined thermopile sensor. 6
1.4 Schematic representation of the considered detector-source object system geometry (© 2019 IEEE) [23]. 9
1.5 Thermopile-based sensor model. 10
1.6 VerilogA script for the thermopile-sensor model. 10
1.7 Modeled response, as a function of the target object temperature, of a thermopile sensor with 100-μV/K sensitivity and a 540-kΩ output resistance, at an ambient temperature of 25°C. . 11
1.8 (a) TMOS symbol and (b) small-signal equivalent circuit for the TMOS. 13
1.9 TMOS temperature variation around room temperature (27°C), for a target object temperature varying from 7 to 47°C, calculated employing 1.21. 15
1.10 Simulated TMOS current I_{DS} as a function of a $\pm$0.4 °C TMOS temperature variation around room temperature, which corresponds to a $\pm$ 20°C target object temperature variation. 16

2.1 (a) Schematic cross section view and (b) schematic longitudinal view of the thermopile legs and the connection to the aluminum plate. The schematic is not in scale (© 2019 IEEE) [23]. 19
2.2 Microphotograph of the proposed micromachined thermopile sensor (© 2019 IEEE) [23]. 19
2.3 Schematic representation of the FOV angle detrmined by the cap on the detector (© 2019 IEEE) [23]. 20
2.4 Packaged thermopile sensor, without and with the perforated metal cap [29]. 22

2.5 Measured thermopile output signal for different black body radiation chopping frequencies. The signal is normalized to its steady-state value. The sensor FOV is 120° (© 2019 IEEE) [23]. 23
2.6 Measurement results considering different distances between the sensor and the black body radiator. The FOV is 120° (© 2019 IEEE) [23]. 23
2.7 Measurement results considering different distances between the sensor and the black body radiator, with a thermopile cap determining a 51.64° FOV angle (© 2019 IEEE) [23]. 24
2.8 Schematic representation of the measurement setup employed for characterizing the sensor responsivity as a function of the radiation incident angle [29]. 25
2.9 (a) Considered orientations of the thermopile sensor, (b) photometric diagram [29]. 26

3.1 Proposed single-ended chopper amplifier architecture (© 2019 IEEE) [23]. 29
3.2 Schematic diagram of (a) first stage, (b) second stage, and (c) bias circuit (© 2019 IEEE) [43]. 30
3.3 Schematic diagram of the interface circuit test-chip prototype and its connection to the thermopile sensor (© 2019 IEEE) [23]. 31
3.4 Microphotograph of the proposed interface circuit (© 2019 IEEE) [23]. 32
3.5 Measured offset at the interface circuit output when the chopper is off. σ is the output offset standard deviation (© 2019 IEEE) [23]. 33
3.6 Measured offset at the interface circuit output when the chopper is on. σ is the output offset standard deviation (© 2019 IEEE) [23]. 33
3.7 Measured gain for the 29 chip samples (© 2019 IEEE) [23]. . . 34
3.8 Input-output characteristic of the proposed chopper amplifier circuit (sample # 29) (© 2019 IEEE) [23]. 35
3.9 Measured output noise power of the proposed amplifier using a Hewlett Packard 3589A Spectrum Analyzer with 4.5 Hz resolution bandwidth (© 2019 IEEE) [23]. 36
3.10 Simulated input referred noise density of the proposed amplifier (© 2019 IEEE) [23]. 38
3.11 Simulated output noise power of the proposed test-chip prototype (© 2019 IEEE) [23]. 38

3.12 Measured thermopile sensor-interface circuit system output with the black body at 10-cm distance and the ambient temperature at 20 °C. The black body temperature is varied in ramp fashion from 20 °C to 50 °C. The buffer offset was not subtracted from the output signal (© 2019 IEEE) [23]. 40
3.13 Measured thermopile sensor-interface circuit system output with the black body at 10-cm distance and the ambient temperature at 35 °C. The black body temperature is varied in ramp fashion from 20 °C to 50 °C. The buffer offset was not subtracted from the output signal (© 2019 IEEE) [23]. 40
3.14 Measurement setup with the heater. When measurements are performed the box is closed and heater and sensor are aligned (© 2019 IEEE) [23]. 41
3.15 Comparison between the thermopile sensor-interface circuit system measured output and the measured thermopile output multiplied by the interface circuit gain. The measurements are performed with the target object at 3 cm distance (© 2019 IEEE) [23]. 42
3.16 Repeated measurements of the thermopile sensor-interface circuit system output with the target object at 3-cm distance. R^2 is the squared linear correlation coefficient (© 2019 IEEE) [23]. 43
3.17 Measured thermopile sensor-interface circuit system output with the target object at different distances. The FOV is 120°C (© 2019 IEEE) [23]. 44
3.18 Measured thermopile sensor-interface circuit system output with the black body at 5-cm distance, with a cap determining a 51.64° FOV angle. The black body temperature is varied as a ramp from 20 to 50 °C. The buffer offset was not subtracted from the output (© 2019 IEEE) [23]. 45
3.19 Measured thermopile sensor-interface circuit system output with the target object at 3-cm distance, with a cap determining a 51.64° FOV angle. The standard deviation σ associated to each measure is expressed in mV (© 2019 IEEE) [23]. 45
3.20 Measured thermopile sensor-interface circuit system output with the black body at 5-cm distance, with a cap determining a 51.64° FOV angle. The black body temperature is varied from 30 to 40 °C with 1 °C steps. The buffer offset was not subtracted from the output (© 2019 IEEE) [23]. 46

3.21 Room used for presence detection testing of a stationary subject. The signs on the floor identify the various considered person's locations [29]. 47
3.22 Person's locations in the room considered for presence detection testing of a stationary subject [29]. 48
3.23 Schematic view of the measurement setup [29]. 49
3.24 Signal in the case of a person standing at d = 1 m from the sensor for different values of α [29]. 50
3.25 Person's locations in the room considered for presence detection testing of stationary subjects, applying the angle correction [29]. 50
3.26 Graphical comparison between the derived fit and the measured data in the case of 1-m fixed distance [29]. 51
3.27 Graphical comparison between the derived fit and the measured data in the case of 6.5° fixed angle [29]. 52
3.28 Graphical comparison between the derived fit and the ideal fit [29]. 52
3.29 3-D graphical representation of the derived fit in cartesian coordinates [29]. 53
3.30 2-D representation of the sensor detection range, obtained from the derived fit. The reported lines are the isolines corresponding to an output signal equal to 10 mV, 5 mV, 2 mV and 1 mV [29]. 54
3.31 Measuremets results in the case of a subject walking at 1 m in front of the sensor. The sensor is located at a 132-cm height from the ground. 55
3.32 Measurement results in the case of a subject walking at 2.5 m in front of the sensor, for different sensor heights. 56
3.33 Measurement results in the case of a subject running at 2.5 m in front of the sensor, for different sensor heights. 56

4.1 2T TMOS voltage-mode readout configuration. 58
4.2 Simulated differential output voltage for a 2T voltage readout configuration, in the case of a ±0.4 °C TMOS temperature variation around room temperature, which corresponds to a ±20 °C target object temperature variation. 59
4.3 3T TMOS voltage-mode readout configuration. 60
4.4 Simulated differential output voltage for a 3T voltage readout configuration, in the case of a ±0.4 °C TMOS temperature variation around room temperature, which corresponds to a ±20 °C target object temperature variation. 60

4.5 Simulated voltage sensitivity $S_{V,\,TMOS}$ for a 3T voltage readout configuration, in the case of a ±0.4 °C TMOS temperature variation around room temperature, which corresponds to a ±20 °C target object temperature variation. 62
4.6 Optimal TMOS voltage-mode readout configuration. 63
4.7 TMOS bias circuit with current DAC for mismatch correction. 65
4.8 Packaged TMOS sensor micrograph. 66
4.9 Schematic view of the setup for the response time measurements. 67
4.10 Measured TMOS differential voltage for different DAC codes. . 68
4.11 Employed measurement setup. 68
4.12 Measured TMOS differential drain voltage with the target at 3-cm distance and ambient temperature equal to 30 °C 69

5.1 TMOS readout circuit chain. 71
5.2 (a) Timing diagram of the filter input signal, (b) employed filter single-ended version. 71
5.3 Interface circuit test-chip micrograph. 73
5.4 Measured offset at the analog interface circuit output. 74
5.5 Measured input-output characteristic of the analog part of the proposed interface circuit with gain equal to 40. 75
5.6 Measured input-output characteristic of the analog part of the proposed interface circuit with gain equal to 60. 75
5.7 Measured input-output ADC characteristic (sample # 1 and sample # 2). 76
5.8 Photograph of the packaged test-chip. 77
5.9 Measurement setup. 78
5.10 Comparison between the TMOS sensor-interface circuit system measured analog output and the measured TMOS output multiplied by the interface circuit gain. The measurements are performed with the target object at 3-cm distance. 79
5.11 Measured TMOS sensor-interface circuit system analog output with the target object at different distances. The FOV is 120°. 79
5.12 Perforated metal cap determining a FOV equal to 50.33°. . . . 80
5.13 Measured TMOS sensor-interface circuit system analog output with the target object at 3-cm distance for different gain values. The FOV is 50.33°. 80
5.14 Measured TMOS sensor-interface circuit system analog output with the target object at different distances. The FOV is 50.33°. 81

5.15 Repeated measurements of the TMOS sensor-interface circuit system analog output with the target object at 3-cm distance. The FOV is 50.33°. R^2 is the squared linear correlation coefficient. 82
5.16 Measured TMOS sensor-interface circuit system digital output with the target object at 3-cm distance. The FOV is 50.33°. . . 82
5.17 Schematic view of the employed measurement setup. 83
5.18 Measurement results for different subject distances. 84
5.19 Measurement results in the case of a subject walking in front of the sensor at different distances. 85
5.20 Measurement results in the case of a subject running in front of the sensor at different distances. 86
5.21 Measurement results in the case of a hand placed in front of the sensor at different distances. 86

List of Tables

2.1 Comparison with state-of-the-art thermopile sensors (© 2019 IEEE) [23] 21
2.2 Goodness of the fit for the proposed thermopile sensor response model at different source distances 25

3.1 DC linearity characterization for randomly selected samples (© 2019 IEEE) [23] 35
3.2 Comparison with state-of-the-art amplifiers suitable for thermocouple-based sensors (© 2019 IEEE) [23] 37
3.3 Derived sensitivity for the thermopile sensor-interface circuit system output for different target object distances (© 2019 IEEE) [23] 43
3.4 Comparison between measurement results and the expected results considering the thermopile sensor model at different target object distances (© 2019 IEEE) [23] 44

4.1 Comparison with Other Readout Configurations for the TMOS 61

5.1 DC linearity and gain characterization for randomly selected samples 74
5.2 Comparison between the proposed thermopile-based and TMOS-based systems 89

Introduction

Thermal sensors, exploiting the relation between the thermal radiation emitted by an object and its temperature, as expressed by the Stefan-Boltzmann law [1, 2], allow realizing contact-less temperature measurements, required in a wide range of applications, ranging from fever measurements to presence detection for security and climate control systems.
With the advent of smart homes and Internet of Things (IoT) and the wide spreading of mobile and wearable devices, the need for low-cost low-power thermal sensors has arisen, therefore moving the focus of the research away from standard bolometers and pyroelectric detectors and towards uncooled infrared (IR) sensors solutions that can be easily integrated. Bolometers and pyroelectric detectors, which are the main types of thermal sensors found nowadays on the market, in fact, do not comply with the low-cost and easy integration specifications.
Integration of thermal sensors is possible through Micro-Electro Mechanical Systems (MEMS) technology, which allows combining on the same substrate or chip both electrical and mechanical structures with dimensions in the micrometer range, thus providing structures with high thermal isolation and low thermal mass. The micromachining processes that are required to thermally isolate the sensing element from the substrate are versatile and include anisotropic wet etching, dry and wet etching, electrochemical etch stop, or the use of silicon-on-insulator (SOI).
In this scenario, STMicroelectronics has fabricated two different novel thermal sensors, which fulfill the low-cost low-power specifications for smart homes, IoT and mobile and wearable devices, while also being compatible with CMOS processes and thus easily integrated: a polysilicon thermopile and a micromachined CMOS transistors, from now on referred to as TMOS.
This Ph.D. activity has been carried out in the frame of a cooperation between the STMicroelectronics Analog MEMS and Sensors R&D group and the University of Pavia, that led to the design of two readout circuits, one for the thermopile sensor and one for the TMOS (developed by the Technion-Israel

Institute of Technology) which were integrated in two test-chip prototypes.
This thesis presents the characterization of both the integrated polysilicon thermopile detector and the TMOS, the design of the readout circuits specifically tailored for the considered thermal sensors and the measurements results obtained characterizing the readout circuits both as stand-alone devices and as systems together with the thermal sensor they were designed for.
This thesis is organized as follows. Chapter 1 describes the different types of thermal detectors. Chapter 2 focuses on the proposed thermopile sensor, while Chapter 3 illustrates the design and experimental results of the thermopile readout circuit. Chapter 4 motivates the choice of the adopted TMOS configuration and details the sensor characteristics, while Chapter 5 illustrates the design and measurements results for its readout circuit. In Conclusions a comparison between the two proposed thermal sensor-readout circuit systems is proposed.

Chapter 1

Integrated contact-less temperature sensors

There exist different types of thermal sensors: bolometers, pyroelectric detectors, thermopiles and active devices such as the TMOS.
In the following sections each type is described and the suitability for integration in low-cost low-power devices for smart homes, IoT and mobile and wearable applications is investigated. The two types of thermal sensors proposed and employed in this work, namely a polysilicon micromachined thermopile and a TMOS, will be analyzed in detail in Chapter 2 and Chapter 4, respectively.

1.1 Bolometers

Bolometers and their miniaturized version (microbolometers) are made of materials whose resistance varies with temperature [3,4]. The resistance variation is expressed by the temperature coefficient of resistance (TCR)

$$\alpha = \frac{1}{R}\frac{dR}{dT} \tag{1.1}$$

where R is the resistance and T the temperature [3].
The variation in the resistance, ΔR, determines in turn a voltage variation which, according to the Ohm law, is

$$\Delta V = I\ \Delta R\ \alpha\ \Delta T \tag{1.2}$$

where I is the bolometer biasing current. Biasing is necessary in order to allow the measurement of the resistance variation.

The basic microbolometer device, typically employed in IR imaging, consists of a thermally isolated IR absorbing membrane with an embedded resistor, which should have high value of TCR. The incident IR radiation absorbed by the bolometer membrane warms up the embedded resistor and as a result, its resistance is changed [5].
At present, the embedded resistors are typically made of vanadium oxide or amorphous silicon, which feature high resistances and TCR parameters. Those materials, however, are not compatible with CMOS technologies: they should be added by surface micromachining in a special fabrication facility on top of the CMOS wafers, significantly increasing the complexity of the design and the cost. Alternatively, bolometers could be mounted on the printed circuit board (PCB) as discrete components, increasing again the overall cost of the system and its area. Therefore, bolometer-based sensors, while being the solution of choice for bulky thermal imagers, are not suited to low-cost and portable applications.

1.2 Pyroelectric detectors

Pyroelectric detectors are made of crystals which display a variation in polarization depending on their temperature: when the crystal temperature changes, charges originate on its faces, as illustrated in the conceptual representation of Fig. 1.1. This mechanism, known as pyroelectric effect, is analogous to the one that occurs in piezoelectric materials when a mechanical stress is applied. The pyroelectric effect is expressed through the so-called pyroelectric coefficient

$$p = \frac{dP}{dT} \tag{1.3}$$

where P is the polarization and T the temperature [3].
In the presence of changes in the temperature, the variation in the polarization and the resulting variation in the charge Q can be, therefore, expressed in terms of the pyroelectric coefficient as follows

$$P = p\Delta T \tag{1.4}$$

$$Q = pAT \tag{1.5}$$

where A is the detector area.
The variation in the charge causes a current

$$I = \frac{dQ}{dt} = Ap\frac{dT}{dt} \tag{1.6}$$

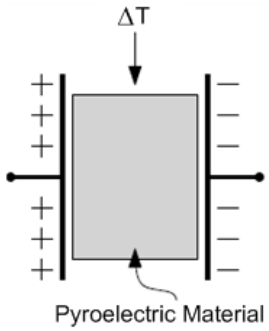

Figure 1.1: Conceptual representation of a pyroelectric material.

Pyroelectric detectors thus display a current transient in response to temperature variations and need a constant current biasing: they are AC devices and cannot provide measurements at DC. This characteristic makes them unsuitable for absolute contact-less temperature measurements applications, such as fever detection, as absolute temperature behaves as a very low-frequency, practically DC, signal.
Pyroelectric IR (PIR) sensors [6–10] are the current choice for occupancy and presence detection applications. However, as they respond to the variation of incident IR radiation, they only detect motion and not stationary occupants, unless some additional expedient, such as optical and mechanical chopping, is employed. Optical chopping [9] employs an array of Fresnel lenses in order to divide the sensor field-of-view (FOV, defined as the solid angle through which the detector is sensitive to radiation) into several optically separated cones: in this way, a subject moving from one cone to the other can be detected; otherwise, as a subject moves through the FOV of the PIR only, especially if it covers a wide area, negligible changes in input IR radiation would be sensed. Mechanical chopping [11–13], instead, employs a shutter to modulate the radiation received by the sensor. The shutter must be moved, therefore a motor is needed, adding significantly to the power consumption the sensor intrinsically requires. Furthermore, the motor can be a source of acoustic noise. Both optical and mechanical chopping, therefore, enhance the system complexity, thus increasing its cost as well as its size. Hence, PIR sensors are not suited for the applications targeted by this work.

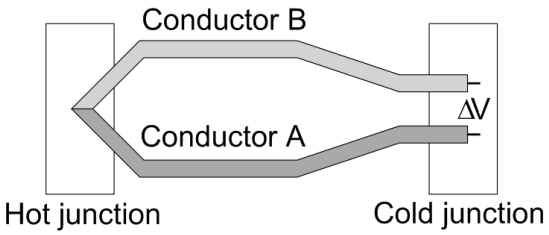

Figure 1.2: Conceptual representation of a thermocouple.

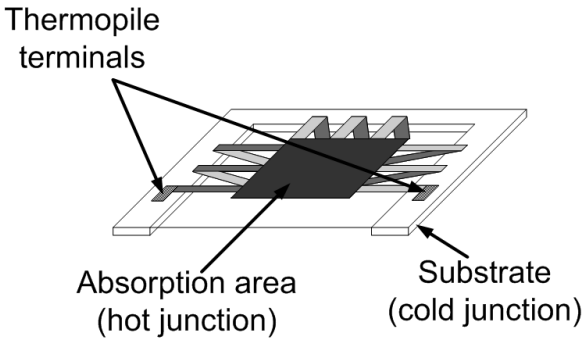

Figure 1.3: Conceptual representation of a micromachined thermopile sensor.

1.3 Thermopiles

Thermopiles [14] consist of N thermocouples connected in series: this allows increasing the sensor output voltage to N times the one of the single thermocouple element. Thermocouples consist of two different conductor materials joined at one end. The two junctions are referred to as hot and cold junction, as indicated in Fig. 1.2. When the junctions are at different temperatures, a voltage difference ΔV originates between the two conductors thanks to the Seebeck effect [15–17], as shown in the following expression:

$$\Delta V = \alpha \Delta T \tag{1.7}$$

where ΔT is the temperature difference between the hot and the cold junction, and α the Seebeck coefficient which depends on the conductor materials.
In miniaturized micromachined thermopiles, as illustrated in Fig. 1.3, the hot junctions are located in the central region of a released dielectric membrane, which absorbs the IR radiation emitted by the target object, while the cold

junction is located on the silicon substrate in order to thermally dissipate and act as a temperature reference. The incident thermal radiation involves a heating of the membrane and then a temperature difference between the hot and cold junction, proportional to the object temperature, which gives rise to the voltage signal.
Thermopiles measure a temperature difference between the junctions. Hence, in order to perform an absolute temperature measurement, as for example is required in the case of human body temperature detection, the temperature of the cold junction should be known, so that proper compensation can be provided.
Unlike bolometers and PIR sensors, thermopiles do not require any biasing. The advantage of being self-powered makes thermopile-based sensors the simplest and most inexpensive thermal sensors. Furthermore, they are fully compatible with standard CMOS processes, as they can be realized by micromachining using MEMS technology [3, 18–20]. Moreover, they are very versatile, as they can be employed in a wide range of applications: medical devices (ear, tympanic and contactless forehead thermometers), security systems (thermal alarms, motion and presence detection sensors), appliances and consumer products (microwave ovens, clothes driers, laser printers), automotive applications (car climate control, seat occupancy, pedestrian detection), climate control systems, continuous temperature monitoring in manufacturing processes, absorbing measurements for gas analysis.
In particular, being self-powered and easily integrated, thermopile-based thermal sensors are ideal for integration in mobile devices. For example, they could be easily integrated in a smartphone to allow fever measurements. The thermal radiation emitted by the body, in fact, could be collected through the phone camera, suitably adapted and paired with an appropriate optical system, and directed on the thermopile-based detector. Then, the sensor output voltage could be processed, in order to provide the user with the body temperature measurement through a software application.
The output voltage signal generated by a thermopile is of the order of hundreds of μV, a few mV at most: hence, an appropriate amplification is required so that the subsequent circuitry can correctly handle the signal.

1.3.1 Thermopile theoretical model

Thermopile sensors respond to the thermal radiation emitted by any object located in the solid angle determined by their field-of-view (FOV) by producing a voltage that is proportional to the incident power, with the FOV being defined as the difference of the incidence angles that allow the sensor to receive

50% relative output signal. The fundamental figure-of-merit for characterizing a thermopile detector is, therefore, its responsivity [21], defined as

$$\mathfrak{R} = \frac{V_{out}}{P_{in}} \tag{1.8}$$

where V_{out} is the thermopile output voltage signal and P_{in} the incident radiant power falling on the detector, which corresponds to the net power exchange between the detector and the radiation source object.
Knowing the detector and source temperatures, T_d and T_s, the thermopile responsivity $\mathfrak{R}$ and the net power exchange from the source P_{in}, the output signal V_{out} can be estimated as follows:

$$V_{out}(T_d, T_s) = \mathfrak{R}\ P_{in}(T_d, T_s) \tag{1.9}$$

P_{in}, and therefore V_{out}, depend on several factors, apart from the detector and the source object temperatures: the detector and source emissivity, the presence of additional objects in the path (e.g. optics), the shape and area of detector and source, as well as the orientation and the distance between them, the detector FOV and the medium between detector and source object.
Taking into consideration all these factors and supposing that the medium is air, the intrinsic FOV of the thermopile is not reduced and, hence, the source object is seen in its entirety by the detector, P_{in} can be expressed as

$$P_{in}(T_d, T_s) = \frac{\sigma \epsilon_s \epsilon_d A_s F_{sd}}{\pi}(T_s^4 - T_d^4) \tag{1.10}$$

where σ is the Stefan-Boltzmann constant, equal to $5.67{\cdot}10^{-12}\frac{\mathrm{W}}{\mathrm{cm^2K^4}}$, ϵ_s the source object emissivity, ϵ_d the detector emissivity, A_s the source area and F_{sd} a transfer factor which takes into account the detector-source system geometry [22].
Assuming a geometrical configuration as the one illustrated in Fig. 1.4, where detector and source are coaxial disks, the transfer factor F_{sd} is given by

$$F_{sd} = \frac{2\pi r_d^2}{r_s^2 + r_d^2 + d_{sd}^2 + \sqrt{\left(r_s^2 + r_d^2 + d_{sd}^2\right)^2 - 4r_s^2 r_d^2}} \tag{1.11}$$

where r_d is the detector radius, r_s the source object radius and d_{sd} the distance between detector and source [22]. The relationship given by (1.11) still holds if the detector and the target object are rectangular in shape: in this case a circular detector and source object of equivalent area must be considered.

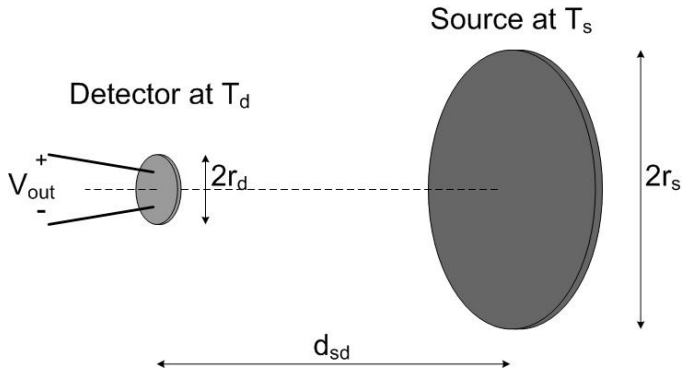

Figure 1.4: Schematic representation of the considered detector-source object system geometry (© 2019 IEEE) [23].

The electronic noise of the thermopile is due to the thermal noise determined by its output resistance $R_{thermopile}$. The noise density, therefore, is

$$V_N = \sqrt{4kTR_{thermopile}} \tag{1.12}$$

where k is the Boltzmann constant, equal to $1.38{\cdot}10^{-23}\frac{\mathrm{m^2kg}}{\mathrm{s^2K}}$, and T the ambient temperature expressed in kelvin [21].
The equivalent noise power (NEP) [21] correlates responsivity and noise and is defined as

$$NEP = \frac{V_N}{\mathfrak{R}} \tag{1.13}$$

Thermopile sensors, as any other thermal detector, exhibit a characteristic transient response when the input IR power changes abruptly. The thermal response time, which consists of the time required for the transient output signal to reach $2^{-1/2}$ of its steady-state value, is determined by the required accumulation of heat in the detector active area [21]. The response time constant τ, in fact, depends on the sensor heat capacitance and effective thermal conductance, i.e. the thermal conductance between the active area and the support structure, which takes into account the heat loss mechanisms in the detector. For thermal detectors, τ ranges between 0.001 to 0.1 seconds.

1.3.2 Thermopile *Cadence* model

A thermopile-based sensor can be modeled as a voltage source with an output resistance, as illustrated in Fig. 1.5: the voltage source output depends on the

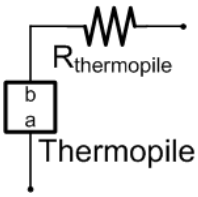

Figure 1.5: Thermopile-based sensor model.

```
`include "constants.vams"
`include "disciplines.vams"

module thermopile_model(a,b);

   inout a,b;
   electrical a,b;

   parameter real Sensitivity=3.606*pow(10,-5);
   parameter real Object_Temperature=37;
   parameter real q_amb20=-8.493*pow(10,-4);

   real m;
   real q;
   real temp_amb;


   analog begin

      m=Sensitivity;
      temp_amb=$temperature;
      temp_amb=temp_amb-273.15;

      q=-m*temp_amb;

      V(b,a)<+m*Object_Temperature+q;


   end

endmodule
```

Figure 1.6: VerilogA script for the thermopile-sensor model.

thermopile sensitivity and on the measured temperature difference between the junctions, while the output resistance depends on the material constituting the thermocouple elements.

In this work, the illustrated model was employed for circuit design and simulations: the voltage source was implemented through a verilogA block and the

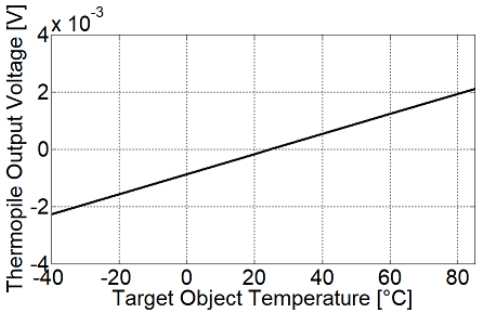

Figure 1.7: Modeled response, as a function of the target object temperature, of a thermopile sensor with 100-μV/K sensitivity and a 540-kΩ output resistance, at an ambient temperature of 25°C.

output resistance was modeled through a standard resistance component from the *Cadence analogLib*. As the standard *analogLib* resistor is inclusive of noise models, no additional modeling was required for the noise of the thermopile, which is substantially limited by its output resistance to the thermal noise contribution.
The output voltage of the verilogA block is described as

$$V_{b,a} = s \cdot T_{obj} + OS \tag{1.14}$$

where s is the thermopile sensitivity, T_{obj} the temperature of the target object and OS an offset which depends on the considered ambient temperature in order to get zero output voltage when the object temperature equals the ambient temperature, modeling the fact that the thermopile measures a temperature difference between the junctions.
Fig. 1.6 reports the verilogA script, while Fig. 1.7 shows the sensor modeled response when the thermopile sensitivity is 100 μV/K.

1.4 TMOS

A new type of uncooled thermal detector has been developed in the last decade thanks to the work of the Technion-Israel Institute of Technology in Haifa, Israel. This novel sensor, referred to as "TMOS" [24], is based on a transistor, made in a standard CMOS-SOI technology, which undergoes MEMS post-processing in order to obtain a suspended and thermally isolated structure by releasing it through dry etching. SOI technology is preferred over regular CMOS processes as it allows achieving good thermal isolation more easily. The

obtained thermally isolated suspended transistor is able to absorb thermal radiation from a target object, inducing an increase of the transistor temperature and, therefore, generating a signal by changing the transistor I-V characteristics.
The sensor employs a mosaic structure [25], featuring a large pixel consisting of a certain number of sub-pixels electrically connected in parallel but thermally isolated. The mosaic design provides enhanced performance and facilitates manufacturing using micro-fabrication methods. Since the sub-pixels are thermally isolated, the thermal time constant of the large pixel is determined by that of the sub-pixel.
With respect to conventional thermal sensors, as the TMOS is an active sensing element, it features advantages in terms of internal gain, resulting in high temperature sensitivity, which makes the TMOS particularly appealing. Furthermore, the TMOS, when employed in subthreshold region, can feature very low power: therefore, it looks promising for applications such as smart homes, IoT and mobile and wearable devices, which require very low power consumption in order to extend the battery life.
The TMOS performance depends on the transistor operating region, as well as on its configuration (2 terminals diode-like, 3 terminals with bulk and source connected together or no bulk employing SOI, 4 terminals). In order to maximize the TMOS performance, therefore, the optimal operating region and transistor configuration must be chosen. The subthreshold region is preferred as operating region for the TMOS as it yields the highest sensitivity value [24,26]. In subthreshold region, in fact, the transistor current operation is based on diffusion and, therefore, is more sensitive to temperature. Furthermore, lower noise is contributed by the transistor and self-heating effects are drastically reduced [27].
The TMOS considered in this work, developed by Technion, is fabricated in a 130-nm CMOS-SOI process by STMicroelectronics and consists of 64 sub-pixel transistors connected in parallel, each with 15.8-μm length and 77.4-μm width.

1.4.1 TMOS theoretical model

The TMOS, whose symbol is reported in Fig. 1.8(a), can be modeled as a standard CMOS transistor, employing the classical transistor small-signal equivalent circuit, as shown in Fig. 1.8(b), with the addition of a current source, i_{sig}, to account for the temperature dependent signal generated by the sensor [28].

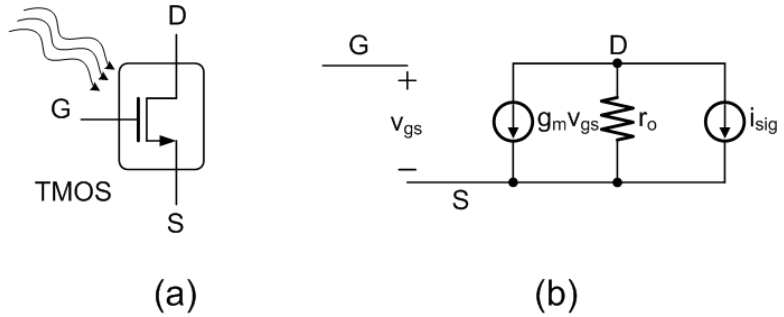

Figure 1.8: (a) TMOS symbol and (b) small-signal equivalent circuit for the TMOS.

i_{sig} can be expressed as

$$i_{sig} = \Delta T_{TMOS} \frac{dI_{DS}}{dT} \tag{1.15}$$

where ΔT_{TMOS} is the temperature variation induced on the TMOS sensor by the radiation absorbed from the target object and $\frac{dI_{DS}}{dT}$ is the transistor current variation with respect to the TMOS temperature for the considered operating point.
For the subthreshold region operation, preferred for its benefits regarding sensitivity to temperature, the transistor drain current is

$$I_{DS} = I_{D0}\, e^{\frac{q(V_{GS}-V_T)}{nkT}} (1 - e^{\frac{-qV_{DS}}{kT}}) \tag{1.16}$$

where I_{D0} is a pre-factor, V_{GS} the gate-to-source voltage, V_{DS} the drain-to-source voltage, V_T the threshold voltage, k the Boltzmann constant, q the magnitude of the electron charge and n a process-dependent parameter.
For V_{DS} larger than a few $\frac{kT}{q}$ (i.e. the thermal voltage), the expression can be simplified to

$$I_{DS} = I_{D0}\, e^{\frac{q(V_{GS}-V_T)}{nkT}} \tag{1.17}$$

and the current sensitivity with respect to the TMOS temperature variation, $S_{I,TMOS}$=$\frac{dI_{DS}}{dT}$, can be derived:

$$S_{I,\,TMOS} = \frac{dI_{DS}}{dT} = I_{D0}\, e^{\frac{q(V_{GS}-V_T)}{nkT}} \frac{q}{nk} \frac{\frac{d(V_{GS}-V_T)}{dT} T - (V_{GS} - V_T)}{T^2} \tag{1.18}$$

$$S_{I,\,TMOS} = I_{DS} \frac{q}{nkT} (-\frac{dV_T}{dT} - \frac{V_{GS} - V_T}{T}) \tag{1.19}$$

$$S_{I,\,TMOS} = -I_{DS} \frac{q}{nkT} (\frac{dV_T}{dT} + \frac{V_{GS} - V_T}{T}) \tag{1.20}$$

The temperature variation induced on the TMOS, ΔT_{TMOS}, can be calculated as

$$\Delta T_{TMOS} = \frac{P_{in}}{G_{th}} \tag{1.21}$$

where P_{in} is the incident radiant power falling on the detector and G_{th} the TMOS thermal conductance.
The expression for P_{in} is

$$P_{in}(T_s, T_d) = \frac{\sigma \epsilon_s \epsilon_d A_s F_{sd}}{\pi N}(T_s^4 - T_d^4) \tag{1.22}$$

where σ is the Stefan-Boltzmann constant, ϵ_s the source object emissivity, ϵ_d the TMOS emissivity, A_s the source object area, F_{sd} the transfer factor which takes into account the detector-source system geometry and N the number of sub-pixels for the employed TMOS. Considering a geometrical arrangement of detector and source such as the one of Fig. 1.10 , as for the thermopile sensor F_{sd} is defined by (1.11).
Relying on the TMOS small-signal equivalent circuit, the current sensitivity with respect to the TMOS temperature variation, $S_{I,\ TMOS}$, is converted into the voltage sensitivity with respect to the TMOS temperature variation, $S_{V,\ TMOS}$, according to

$$S_{V,\ TMOS} = -Z_{out}\ S_{I,\ TMOS} \tag{1.23}$$

where Z_{out} is the TMOS output impedance.
As for the thermopile, the fundamental figure-of-merit to characterize the sensor performance is its responsivity, defined as

$$\mathfrak{R} = \frac{V_{out}}{P_{in}} = \frac{S_{V,\ TMOS}\ \Delta T_{TMOS}}{P_{in}} = \frac{-Z_{out}\ S_{I,\ TMOS}\ \Delta T_{TMOS}}{P_{in}} \tag{1.24}$$

1.4.2 TMOS *Cadence* model

The "virgin" (not released) TMOS characteristics are nearly the same as the post-MEMS-processed one [24]: it is, therefore, possible to simulate in *Cadence* the TMOS performance relying on standard 130-nm CMOS process design kits (PDK).
The TMOS intrinsic sensitivity to temperature was evaluated through DC *Cadence* simulations considering the TMOS biased at 600-mV drain voltage and 287-mV gate voltage, with the source terminal connected to ground. The drain voltage was chosen equal to 600 mV in order to match the common-mode voltage value, equal to half the supply voltage, desired for the readout circuit. The

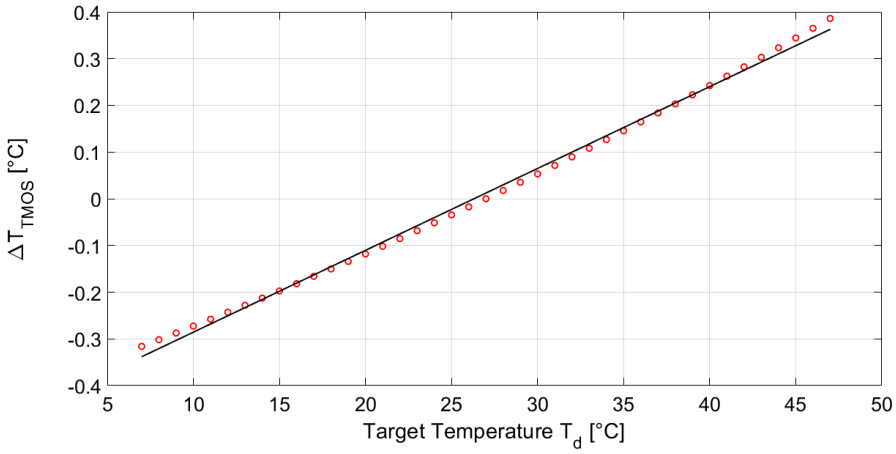

Figure 1.9: TMOS temperature variation around room temperature (27°C), for a target object temperature varying from 7 to 47°C, calculated employing 1.21.

gate voltage, instead, was set in order to have 1-μA drain-to-source current, I_{DS}, at room temperature, which corresponds to a transistor operating point in the subthreshold region.
Although the TMOS is fabricated in a 130-nm CMOSO-SOI process, a standard 130-nm CMOS PDK was employed for simulations: however, connecting source and bulk together, the model was a good fit also for the SOI technology.

The TMOS was modeled through a multi-technology mode (MTM) block, consisting of a transistor of a standard 130-nm technology with the source and bulk terminals connected together. Thanks to the multi-technology simulation (MTS) option, enabled by the use of a MTM block, it was possible to define the TMOS block temperature independently from the one of the rest of the circuit and vary it to simulate the sensor temperature variation in response to the absorption of thermal radiation from a target object.
Each TMOS consists of 64 fingers, modeling the sub-pixels, of width and length equal to 77.4 μm and 15.8 μm, respectively.
The simulation was performed considering a room temperature equal to 27°C and a TMOS temperature variation around room temperature corresponding to a target object temperature ranging from 7 to 47°C, i.e. a $\pm$20°C variation around room temperature. In order to derive the TMOS temperature variation corresponding to the desired target temperature variation, the TMOS

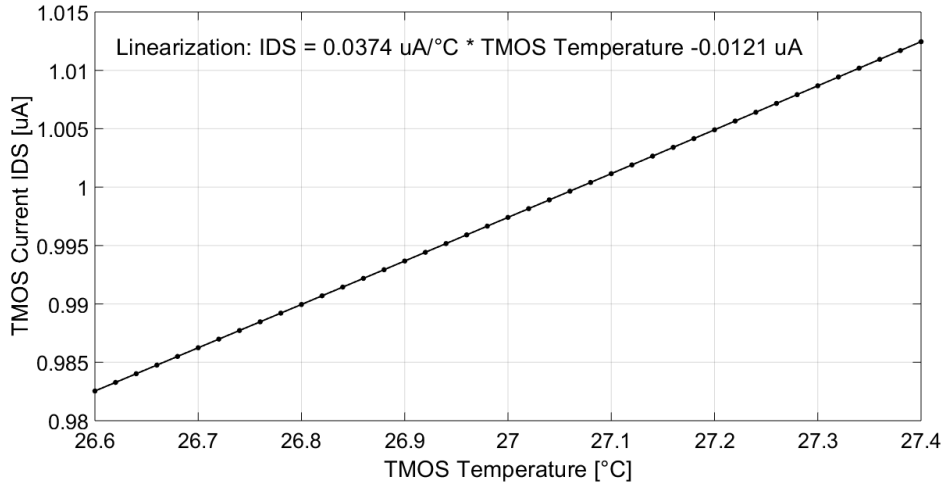

Figure 1.10: Simulated TMOS current I_{DS} as a function of a ±0.4 °C TMOS temperature variation around room temperature, which corresponds to a ± 20°C target object temperature variation.

temperature variation ΔT_{TMOS} was considered proportional to the target object temperature variation ΔT_{target} by a transfer factor TF

$$\Delta T_{TMOS} = TF \ \Delta T_{target} \tag{1.25}$$

TF was derived as the slope of the linearized expression of 1.21, considering T_d=300.15 K (i.e. 27 °C), T_s ranging from 280.15 to 320.15 K (i.e. from 7 to 47 °C), d_{sd} equal to 3 cm and a disk-like target object with 2.11-cm radius. Expression 1.21 and its linearization are plotted as a function of the desired target temperature in Fig. 1.9. For the employed TMOS, TF is roughly equal to 0.02: the TMOS temperature range corresponding to a target object temperature ranging from 7 to 47 °C is, therefore, from 26.6 to 27.4 °C.
The simulated TMOS I_{DS} current is reported in Fig. 1.10: it yields excellent linearity as the squared linear correlation coefficient is 0.999995.
The current sensitivity with respect to the target temperature variation, $S_{I,\ target}$, relying on (1.15)-(1.25), is defined as

$$S_{I,\ target} = TF \ \frac{dI_{DS}}{dT} = TF \ S_{I,\ TMOS} \tag{1.26}$$

From simulations $S_{I,\ TMOS}$ is equal to 37.4 nA/°C and $S_{I,\ target}$ is equal to 0.748 nA/°C. The simulated results employing the standard 130-nm CMOS

PDK well matched the TMOS characterization measurements previously performed by STMicroelectronics, as well as the theoretical model, thus validating the choice of employing the standard 130-nm CMOS PDK, although the TMOS is fabricated in 130-nm CMOS-SOI, in order to investigate the sensor performance.

Chapter 2

Integrated micromachined thermopile

In this work, an integrated micromachined thermopile sensor developed by STMicroelectronics was characterized and employed.
The proposed miniaturized micromachined thermopile sensor was designed in order to achieve the maximum available active area and number of thermocouple elements, while taking into account the membrane reliability and stability, thus maximizing its responsivity.
Due to its high Seebeck coefficient and its easiness of integration, p/n polysilicon was employed as conductor material for the thermocouples.
The number of thermocouple elements placed in series, equal to 160, was limited by the lithography rules once the sensor lateral dimension was fixed in order to maximize the absorbing area while maintaining the membrane stable and not mechanically stressed. The absorbing membrane for radiation consists of a 0.8 mm $\times$ 0.8 mm central aluminum plate, embedded in a dielectric membrane released by the silicon substrate through a back dry etch.
Each thermocouple element (leg) length was limited to 250 μm, resulting in a thermopile output resistance equal to 540 kΩ.
Fig. 2.1(a) and Fig. 2.1(b) illustrate a schematic view of the thermopile sensor, showing both the cross section and the longitudinal section of the polysilicon legs, respectively, as well as their connections to the aluminum plate. A microphotograph of the sensor is reported in Fig. 2.2.
The proposed thermopile sensor achieves a measured responsivity value equal to 180 V/W, which is almost double with respect to typical thermopile-based thermal sensors. For the proposed thermopile sensor, the measured time constant τ is equal to 13 ms. As the considered thermopile sensor has an output

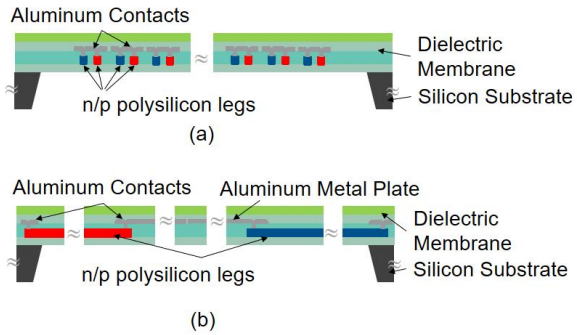

Figure 2.1: (a) Schematic cross section view and (b) schematic longitudinal view of the thermopile legs and the connection to the aluminum plate. The schematic is not in scale (© 2019 IEEE) [23].

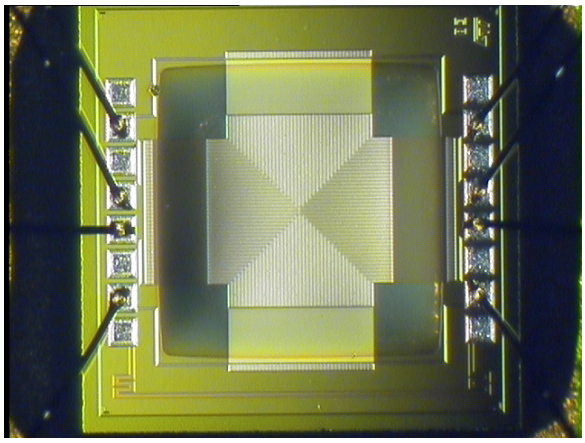

Figure 2.2: Microphotograph of the proposed micromachined thermopile sensor (© 2019 IEEE) [23].

resistance equal to 540 kΩ, its noise density at 25 °C is 94 nV/$\sqrt{Hz}$, with a NEP equal to 0.52 nW/$\sqrt{Hz}$.
However, electronic noise is not the dominant noise source: because of its high responsivity, in fact, the proposed thermopile detector is very sensitive to background temperature fluctuations, which act as disturbances and environmental noise. Furthermore, with a 120° FOV, the sensor always picks up thermal radiation from the entire surroundings and not only from the target object. A solution to reduce environmental noise is limiting the FOV by adding a perforated metal cap on the sensor, as illustrated by the conceptual representation

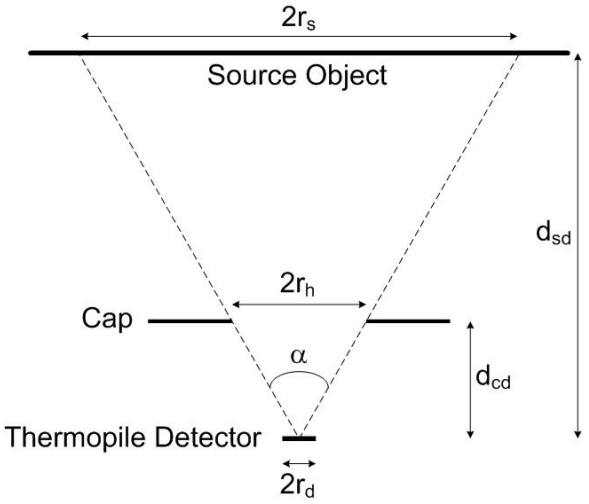

Figure 2.3: Schematic representation of the FOV angle detrmined by the cap on the detector (© 2019 IEEE) [23].

of Fig. 2.3. Relying on trigonometry, the FOV angle is calculated as:

$$\alpha = 2\ arctan\left(\frac{r_h}{d_{cd}}\right) \tag{2.1}$$

where r_h is the cap hole radius and d_{cd} the distance of the cap from the detector.
Provided that the target object fills the entire detector FOV, the model described by equations (1.9)-(1.10)-(1.11) still holds, with $A_s{=}\pi r_s^2$ and r_s given by:

$$r_s = d_{sd}\ tan\left(\frac{\alpha}{2}\right) \tag{2.2}$$

The proposed thermopile device, packaged in a TO-5, is shown in Fig. 2.4, both without and with the metal cap.
Tab. 2.1 illustrates the comparison between the proposed sensor and other state-of-the-art thermopile-based thermal detectors, summarizing the different figures-of-merit.
The proposed thermopile sensor features by far the highest responsivity, with the largest number of thermocouple elements and an active area size comparable to the ones of the other reported detectors. The featured noise density is the highest, as the thermopile output resistance is the largest. However, thanks to the excellent responsivity, the NEP is still very competitive with the ones of the other sensors. Moreover, the penalty in noise density, due to

Table 2.1: Comparison with state-of-the-art thermopile sensors (© 2019 IEEE) [23]

Parameter	**This work**	**SBT [30]**	**Thermopile in air [31]**	**TS118-5 [32]**	**S25-TO-18 [33]**
Thermocouple material	n-poly/p-poly	n-poly/aluminum	n-poly/p-poly	BiSb/NiCr	silicon
Number of thermocouple elements	160	80	96	100	20
Active area [mm^2]	0.8 x 0.8	–	–	0.7 x 0.7	0.25 x 0.25
Thermopile output resistance [kΩ]	540	173	306	50	23
Responsivity [V/W]	180	38.66	88.5	100	111.5
Noise density at 25°C [$nV/\sqrt{Hz}$]	94	53	71	29	19.4
NEP at 25°C [$nW/\sqrt{Hz}$]	0.52	1.37	0.80	0.29	0.17
Time constant [ms]	13	5.3	–	40	16 (in Argon)
FOV [degrees]	120	–	–	–	88-103
Optical filter	no	–	–	yes	yes

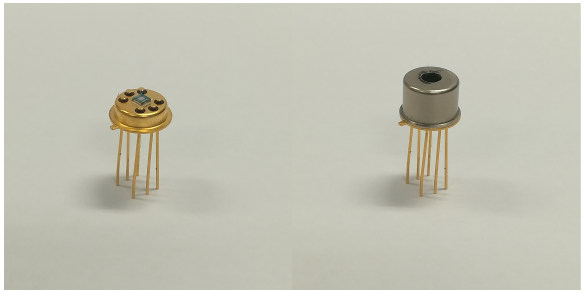

Figure 2.4: Packaged thermopile sensor, without and with the perforated metal cap [29].

the thermopile material, is compensated by the advantages that polysilicon gives in terms of compatibility with standard CMOS processes. The time constant is comparable with the ones of the other reported thermopiles. It is to be noted that the figures-of-merit achieved by the proposed thermopile sensor are obtained without the employment of any optics (e.g. filters) which could further enhance the performance.

2.1 Thermopile characterization measurements

The proposed thermopile sensor was thoroughly characterized through measurements considering a black body radiator as target object. The employed black body radiator is the SR-800R 4D/A model by CI Systems [34], which features a 4 in $\times$ 4 in area and almost ideal emissivity, equal to 0.99. As the thermopile is self-powered, no biasing was required. A Keithley 2001 multimeter, coupled with a LabView program, was used to acquire the thermopile output voltage.
In order to measure the thermopile time constant, the black body radiation was mechanically chopped and the sensor output signal was measured and normalized with respect to its steady-state value. The measurements were repeated for different chopping frequencies, ranging from 0.1 to 25 Hz: the results are reported in Fig. 2.5. By means of interpolation, the frequency f for which the output signal is $2^{-1/2}$ of its steady-state value was identified. The time constant τ is determined as

$$\tau = \frac{1}{2\pi f} \tag{2.3}$$

As f is 12 Hz, the thermopile time constant τ is 13 ms.

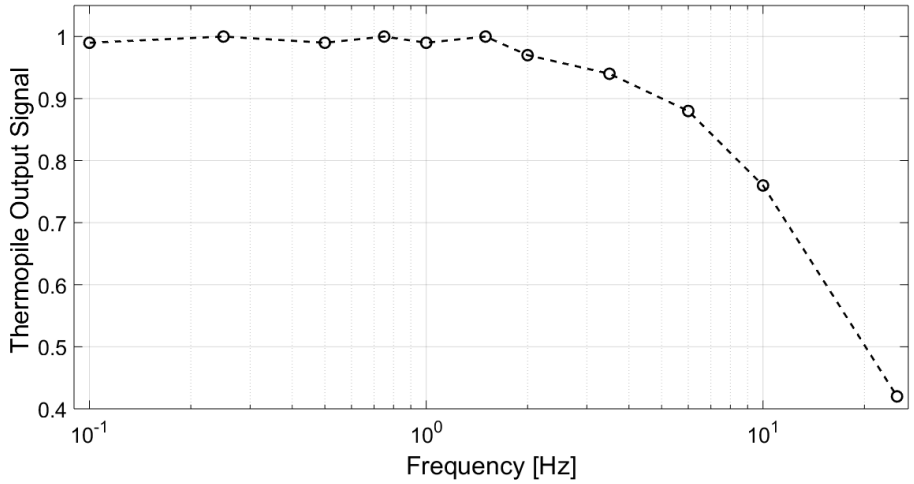

Figure 2.5: Measured thermopile output signal for different black body radiation chopping frequencies. The signal is normalized to its steady-state value. The sensor FOV is 120° (© 2019 IEEE) [23].

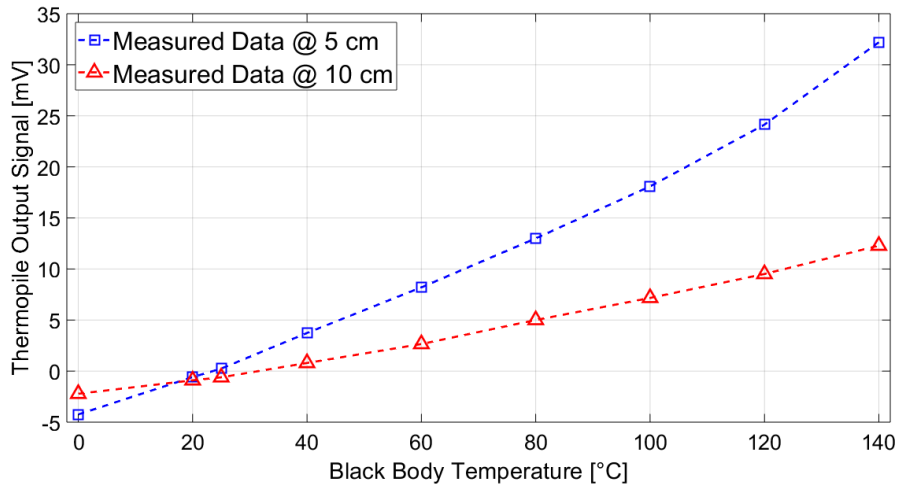

Figure 2.6: Measurement results considering different distances between the sensor and the black body radiator. The FOV is 120° (© 2019 IEEE) [23].

The sensor response to non-chopped radiation sources was also investigated. The temperature of the black body radiator was varied from 0 to 140 °C,

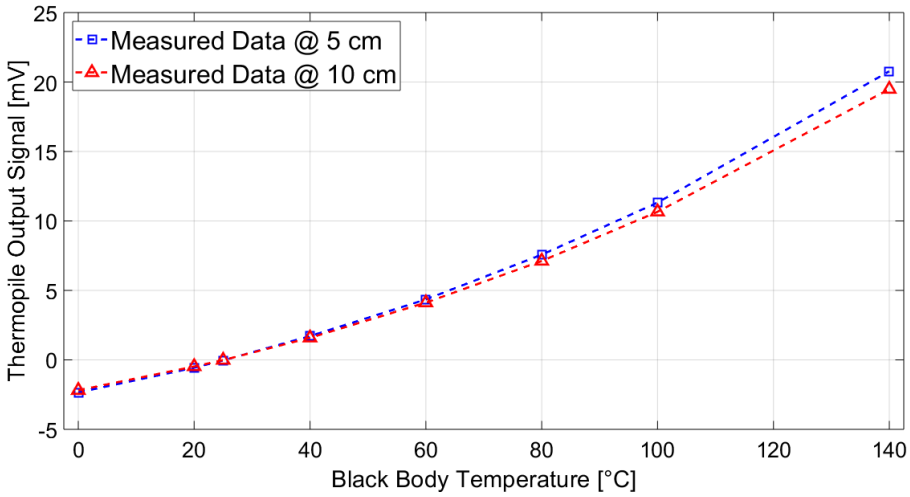

Figure 2.7: Measurement results considering different distances between the sensor and the black body radiator, with a thermopile cap determining a 51.64° FOV angle (© 2019 IEEE) [23].

placing the sensor at different distances, at an ambient temperature approximately equal to 25 °C. Fig. 2.6 illustrates the measurement results for 5-cm and 10-cm distances, always considering a 120° FOV (no cap applied).
The measurements were repeated applying the perforated metal cap on the thermopile sensor. The inner surface of the cap was covered in black opaque paint in order to avoid reflections. The hole diameter was 3 mm and the distance between cap and detector was 3.1 mm. In this way, the FOV was reduced to 51.64°, as derived applying (2.1). The measurements results are reported in Fig. 2.7. Linearizing around room temperature, i.e. 20°, the derived sensitivity is roughly 90μV/°.
The measurements with reduced FOV exhibit almost no dependence on the distance between the sensor and the radiator. This is to be expected as, in the considered case, the FOV is completely filled by the target object. In fact, considering the modeled thermopile output signal and applying (2.2), provided that, as it is verified in this case, $r_d << d_{sd}$, the following expression holds true

$$F_{sd}\ A_s \approx \frac{2\ d_{sd}^2\ tan^2\left(\frac{\alpha}{2}\right)\ r_d^2\ \pi^2}{2\ d_{sd}^2\ \left(tan^2\left(\frac{\alpha}{2}\right)+1\right)} = \frac{tan^2\left(\frac{\alpha}{2}\right)\ r_d^2\ \pi^2}{tan^2\left(\frac{\alpha}{2}\right)+1} \tag{2.4}$$

The model well fits the measurements both for unlimited and reduced FOV, as

Table 2.2: Goodness of the fit for the proposed thermopile sensor response model at different source distances

Distance	R^2 (120° FOV)	R^2 (51.64° FOV)
5 cm	0.99817	0.99995
10 cm	0.99712	0.99994

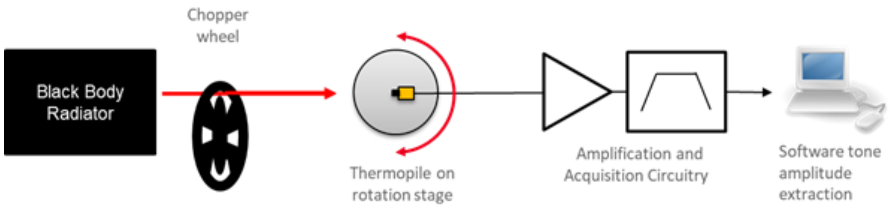

Figure 2.8: Schematic representation of the measurement setup employed for characterizing the sensor responsivity as a function of the radiation incident angle [29].

it is illustrated in Tab. 2.2, where R^2 represents the coefficient of correlation between the modeled and the measured data. The modeled data were derived from equations (1.9)-(1.10)-(1.11), calculating r_s from (2.2), considering $\alpha = 51.64°$, when the metal cap is applied.
The thermopile responsivity as a function of the radiation incident angle was also investigated, considering the thermopile without the metal cap and a measurement setup as follows. The infrared radiation emitted by the black body at 300 °C was focused on the thermopile active area. The thermopile sensor was positioned on a controlled rotation stage, in order to change the relative angle between the black body source and the sensor, thus varying the radiation incident angle. The optical excitation signal was chopped at 40 Hz, that is much higher than the thermopile cutoff frequency (12 Hz), in order to provide rejection for the low frequency noise contributed by air movements, due to air convection, instruments cooling fans and people movements. Fig. 2.8 illustrates the experimental setup schematic.

The characterization was performed considering two different orientations of the device under test as reported in Fig. 2.9(a). The measured response for the different incident angles θ, normalized to the maximum measured value, considering both orientations, is reported in the photo-metric diagram of Fig. 2.9(b). The obtained photo-metric diagram can be well fitted with $cos(\theta)$, as shown in Fig. 2.9(b): the thermopile surface can be in fact considered a

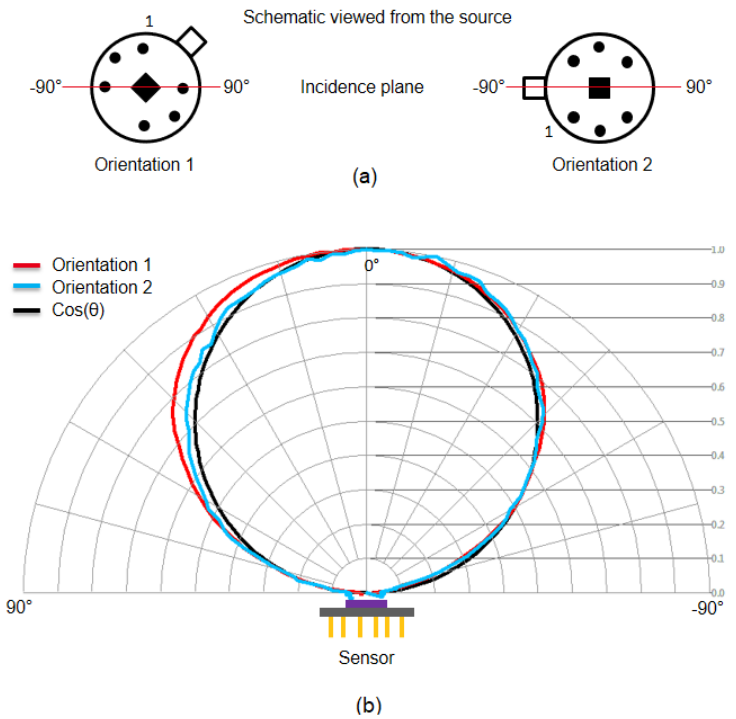

Figure 2.9: (a) Considered orientations of the thermopile sensor, (b) photometric diagram [29].

lambertian surface, since no filters or lenses are integrated on the thermopile active surface [35]. The response can be considered independent from the orientation.

Chapter 3

Thermopile sensor readout circuit

The thermopile output voltage signal is of the order of hundreds of μV, a few mV at most, and behaves substantially as a DC, as temperature varies very slowly and can be assumed constant during the time interval (few seconds) needed to perform the measurement: hence, the readout circuit must provide amplification, while limiting the amplifier offset and noise at low frequency.
Specifications for contact-less human body temperature measurements, requiring repeatability and accuracy within ± 0.3 °C, are the ones set for the readout circuit design. As presence detection sensors require similar, but less strict, specifications, the resulting system can be employed both for fever detection and security and climate control applications.

3.1 Readout circuit description

As stated in the previous paragraph, low offset and noise at low frequency must be ensured for the amplifier.
In order to limit the amplifier offset, two main solutions exist: the autozero and the chopper stabilization technique [36]. Both techniques also remove the flicker noise of the amplifier. However, due to the folding of high frequency components back to baseband determined by the sampling, the residual noise in the case of the autozero is higher than in the case of the chopper, where no sampling occurs. For this reason, the chopper solution was preferred.
A chopper amplifier [37] consists of a regular amplifier preceded and followed by a modulator, or chopper. The modulator is implemented by means of

switches controlled by complementary and non-overlapping phases. The input signal is modulated at the chopping frequency, amplified and then modulated back to baseband, while the amplifier offset and low frequency noise are modulated only once, thus appearing at the output at the chopping frequency and its odd harmonics, which can be subsequently removed by low-pass filtering. Provided that the chopping frequency is higher than the $1/f$ noise corner frequency of the amplifier, the flicker noise is completely removed and the baseband noise is almost equal to the thermal noise. Because of spikes due to the charge injection mismatch of the switches, a residual offset still remains [38]. The residual offset is proportional to the chopping frequency: therefore a trade-off between residual offset and noise arises.
To reduce this offset, while still maintaining good noise cancellation, the chopping frequency for the designed readout circuit was chosen approximately equal to the noise corner frequency of the chopped amplifier [36, 38]: this was possible as the noise corner frequency of the amplifier, roughly equal to 2 kHz, is much higher than the signal frequency. The bandwidth requirement for the amplifier is, therefore, limited only by the chopping frequency.
As high accuracy is required in order to perform fever measurements, a closed-loop structure was preferred in order to achieve a more accurate control of the amplification factor, unlike other amplifiers specifically designed for thermopile sensors [39], which instead adopted an open-loop architecture.
Typically, chopper amplifiers employ a fully-differential structure with relatively low input impedance. However, given the sensor characteristics, the usual fully-differential architecture cannot be employed in this case and a single-ended architecture was adopted instead.
A fully differential structure, in fact, would give rise to a number of drawbacks. The amplification factor in closed loop would depend on the thermopile output resistance and, as that is equal to 540 kΩ and cannot be reduced, the required value for the feedback resistance, in order to achieve the desired amplification factor, should be in the order of tens of MΩ, thus occupying extensive silicon area. More importantly, some current would flow through the thermopile, therefore resulting in the sensor experiencing the Peltier effect [15–17], which determines a temperature variation when current flows through the thermopile. This would cause an obvious degradation of the temperature measurement, that is clearly in contrast with the high accuracy required by the application. Furthermore, the adopted single-ended configuration allows the proper setting of the common-mode voltage: the thermopile considered in this work, in fact, is a two terminal device and if the thermopile signal voltage was to be applied differentially at the input, as it would be required by other

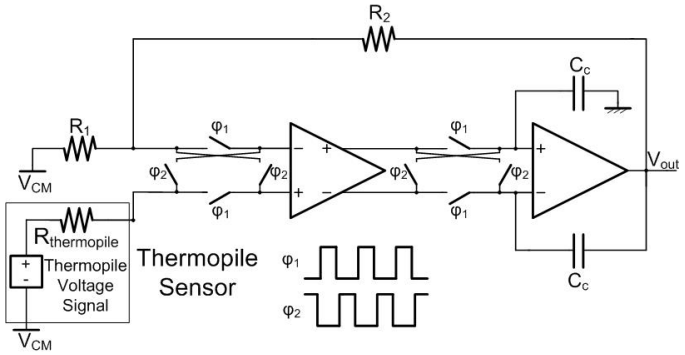

Figure 3.1: Proposed single-ended chopper amplifier architecture (© 2019 IEEE) [23].

works on state-of-the-art chopper amplifiers suitable for thermocouple-based sensors [40–42], two thermopiles in series should be employed instead of one. The proposed single-ended negative-feedback non-inverting configuration [23, 43], illustrated in Fig. 3.1, solves all the fully-differential structure drawbacks: the amplification factor is given by A=1+R_2/R_1 and does not depend on the thermopile output resistance, no current flows through the thermopile, due to the ideally infinite input impedance seen by the sensor, and the common mode voltage setting is straightforward.

In order to achieve the required 100-dB open loop gain, two amplifying stages were employed. Since the second-stage offset and noise are divided by the first-stage gain when referred to the input, being therefore less significant, only the first-stage amplifier is chopped. The first-stage fully-differential architecture allows maintaining the ease of the classic chopper structure, while the second stage provides the fully-differential to single-ended conversion.The modulators are implemented through CMOS switches, controlled by complementary and non-overlapping phases provided by a standard disoverlap circuit. Capacitances C_c, equal to 220 fF, ensure compensation. The nominal power supply is 1.2 V and the common-mode voltage, V_{CM}, is 600 mV. Resistances R_1 and R_2, equal to 1 and 99 kΩ, respectively, set the amplification factor to 100.

Fig. 3.2 shows the schematic diagram of the designed amplifier: the first stage amplifier is implemented through a folded cascode configuration, while the second stage consists of a simple differential pair with active load. The same biasing circuit, illustrated in Fig. 3.2(c), is used for both amplifying stages. The biasing current I , set to 70 μA, is provided externally. In the first stage, reported in Fig. 3.2(a), only one couple of cascode transistors is used, as, be-

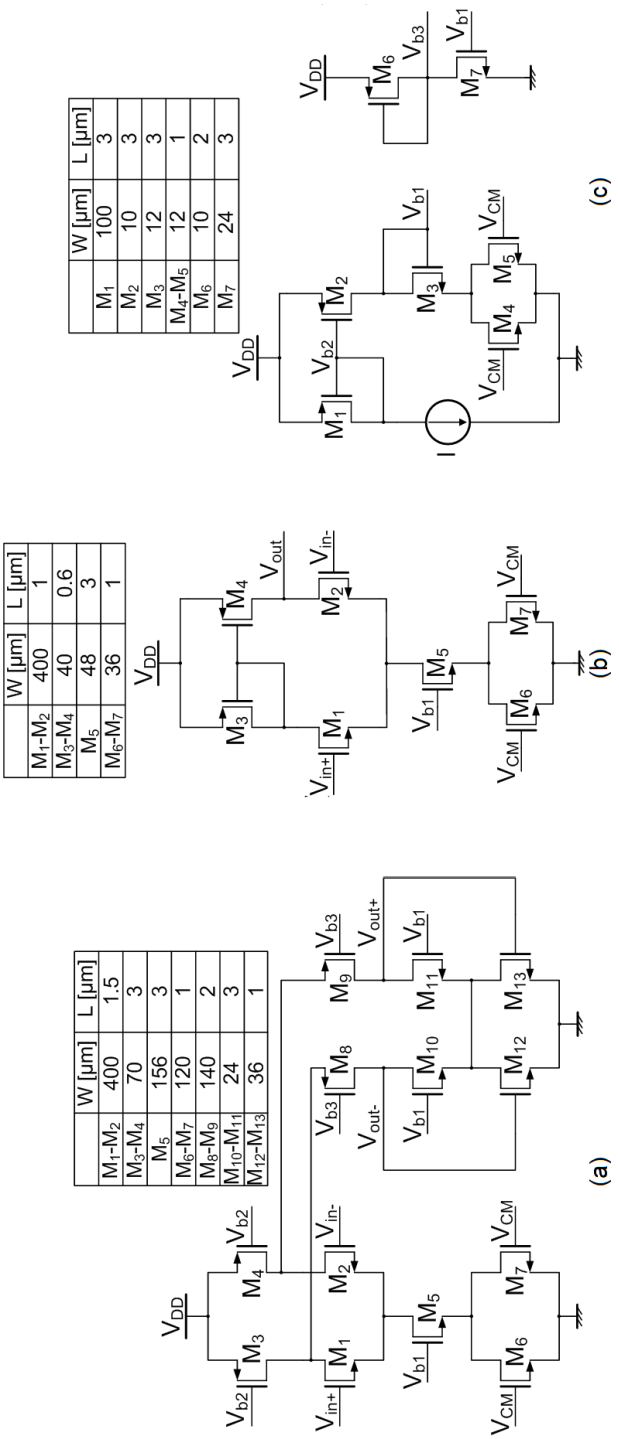

	W [µm]	L [µm]
M_1-M_2	400	1.5
M_3-M_4	70	3
M_5	156	3
M_6-M_7	120	1
M_8-M_9	140	2
M_{10}-M_{11}	24	3
M_{12}-M_{13}	36	1

	W [µm]	L [µm]
M_1-M_2	400	1
M_3-M_4	40	0.6
M_5	48	3
M_6-M_7	36	1

	W [µm]	L [µm]
M_1	100	3
M_2	10	3
M_3	12	3
M_4-M_5	12	1
M_6	10	2
M_7	24	3

Figure 3.2: Schematic diagram of (a) first stage, (b) second stage, and (c) bias circuit (© 2019 IEEE) [43].

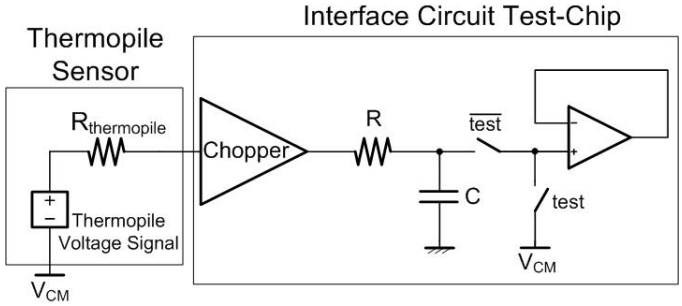

Figure 3.3: Schematic diagram of the interface circuit test-chip prototype and its connection to the thermopile sensor (© 2019 IEEE) [23].

cause of the limited supply voltage of 1.2 V, there was not enough headroom for a stack of five transistors in the output branch to guarantee a design robust against mismatches. In the second stage, shown in Fig. 3.2(b), transistors M_6 and M_7 were added to the usual differential pair with active load structure for matching purposes, since the biasing circuit comprises transistors M_4 and M_5, which are part of the common mode feedback implementation of the first stage. In both amplifying stages, the input differential pair transistors M_1 and M_2 operate in the subthreshold region: this gives a well known advantage in terms of offset [44].

The circuit, implemented in a standard 130-nm CMOS process by STMicroelectronics, was integrated in a test chip prototype with a passive low-pass filter and an output buffer, as illustrated in Fig. 3.3. The filter, whose cut-off frequency is 5 Hz, removes the modulated offset, moved at the chopping frequency and its odd harmonics due to the chopper action, while the buffer drives the output pad. Two CMOS switches were added in order to enable a test mode for the output buffer, during which the offset of the buffer is measured, so it can be taken into account when the signal measurement is performed. In this way, the measurement of the residual offset of the chopper amplifier only can be derived. A die photo of the interface circuit prototype is reported in Fig. 3.4.

The passive filter was employed in this first realization as it guaranteed more ease and speed of design and the interest was on the chopper structure itself. However, future realizations will be optimized by employing an active filter.

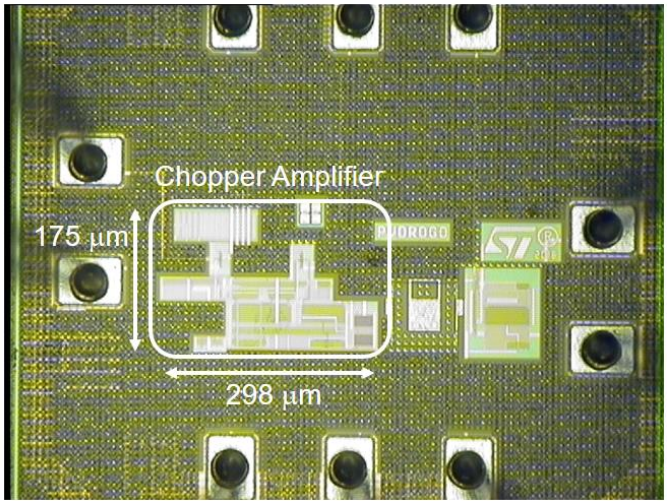

Figure 3.4: Microphotograph of the proposed interface circuit (© 2019 IEEE) [23].

3.2 Readout circuit measurement results

The interface circuit was implemented in a standard 130-nm CMOS process and integrated in a 0.820 × 0.738 mm^2 test-chip prototype. The measurement set-up for the circuit characterization was as follows. An Agilent E3631A power supply provided the supply voltage, equal to 1.2 V, while a Hewlett Packard 3245 universal source supplied the common-mode voltage, V_{CM}, equal to 600 mV. The bias current, equal approximately to 70 μA, was regulated through a variable resistor on-board. A toggle switch was used to control the signal enabling the test phase to measure the buffer offset. The clock signal was supplied by a Tektronix AFG3252 function generator. A Keithley 2000 multimeter was employed in voltmeter mode to measure the circuit output voltage. The batch considered for measurements consisted of 29 samples of the proposed amplifier circuit test-chip prototype: this allowed obtaining an acceptable statistical characterization.
Using the multimeter in ammeter mode, it was possible to measure the supply current for the entire test-chip prototype. The supply current mean value across the 29 samples is 244.49 μA, with 1.18 μA standard deviation. As 14% of the supply current is employed for the output buffer, the proposed chopper amplifier supply current is 210.26 μA, resulting in a power consumption approximately equal to 252 μW.

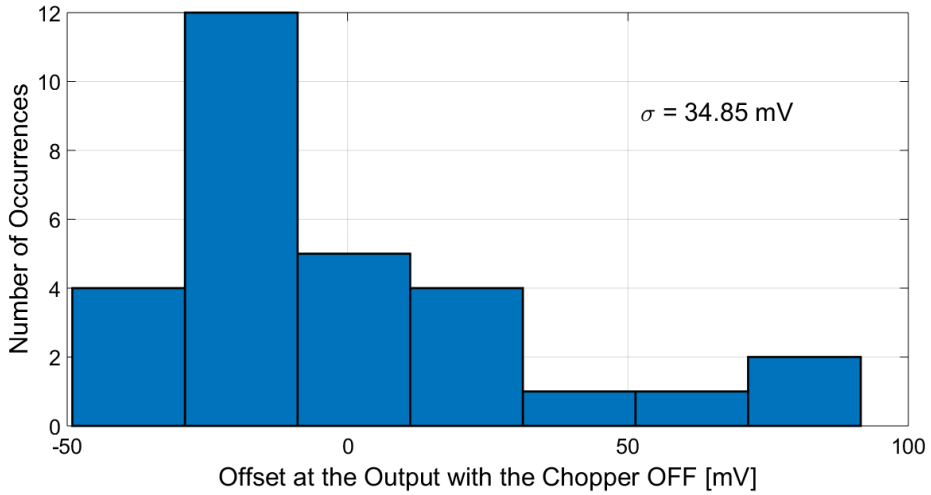

Figure 3.5: Measured offset at the interface circuit output when the chopper is off. σ is the output offset standard deviation (© 2019 IEEE) [23].

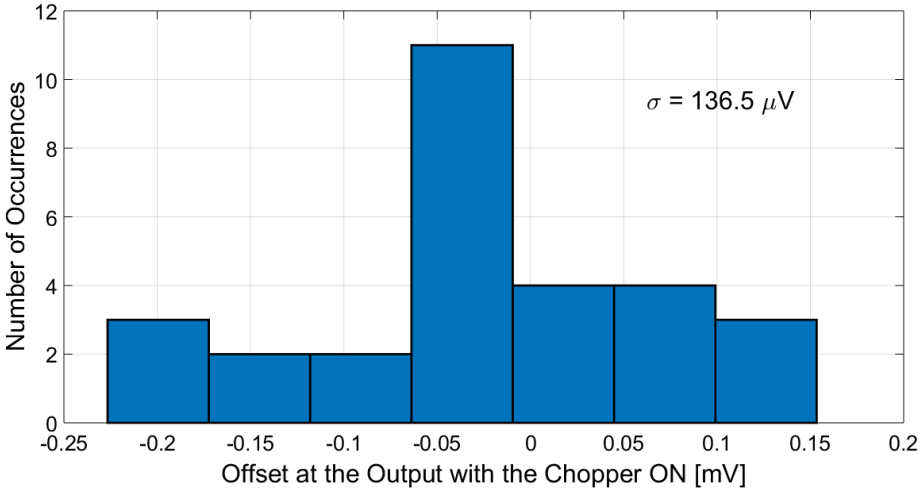

Figure 3.6: Measured offset at the interface circuit output when the chopper is on. σ is the output offset standard deviation (© 2019 IEEE) [23].

To verify the correct operation of the chopper structure and measure the residual offset, only the common-mode voltage, and no signal, was applied to the circuit. First the test phase was enabled in order to measure the output offset

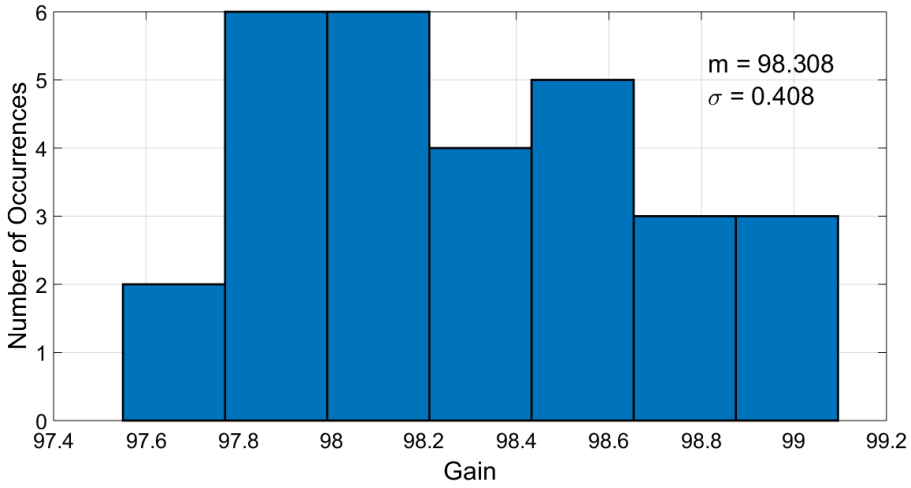

Figure 3.7: Measured gain for the 29 chip samples (© 2019 IEEE) [23].

of the buffer, then the circuit was switched to normal operation and the output offset of the chain, consisting of the chopper amplifier, low-pass filter, and buffer, was measured. The buffer offset was then subtracted from the chain offset: in this way the offset due to the chopper amplifier only was derived. This measurement was performed at first with the clock signal connected to ground (chopper off) and then supplying a 2-kHz 0-1.2-V square wave with the function generator (chopper on). The results, across the 29 samples, with the chopper off and the chopper on are shown in Fig. 3.5 and Fig. 3.6, respectively. The standard deviation values at the output are, with the chopper off and with the chopper on, 34.85 mV and 136.5 μV. To derive the input referred standard deviation value, the standard deviation at the output was divided by the amplifier ideal gain, i.e. 100. The resulting offset standard deviation values at the input are, therefore, 348.5 μV with the chopper off and 1.365 μV with the chopper on. Hence, the chopper reduces the offset standard deviation approximately by a factor 255.

Applying a DC signal approximately equal to 1 mV, precisely 0.893 mV, plus the common-mode voltage, the amplifier gain was derived from the output voltage measurement, always taking into account the buffer offset and subtracting the common-mode voltage. The results are illustrated in Fig. 3.7: the mean gain value, m, is 98.308, with standard deviation σ equal to 0.408. The difference from the ideal desired gain (i.e. 100), due to a process resistance mismatch error, is deemed acceptable. Furthermore, it could be corrected by

Table 3.1: DC linearity characterization for randomly selected samples (© 2019 IEEE) [23]

Sample Number	Linear Correlation Coefficient R	Derived Gain
7	0.999988	97.64
13	0.999989	97.05
20	0.999980	98.27
29	0.999978	98.34

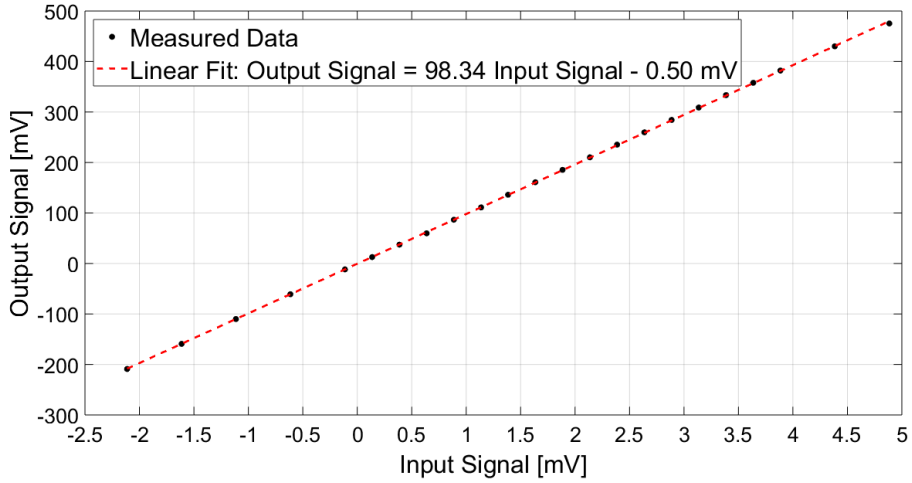

Figure 3.8: Input-output characteristic of the proposed chopper amplifier circuit (sample # 29) (© 2019 IEEE) [23].

trimming.
Four randomly selected samples were fully characterized, varying the applied DC signal approximately from −2 mV to 5 mV, in order to verify the amplifier linearity. The results are reported in Tab. 3.1: the linear correlation coefficients, practically equal to 1, show almost ideal linearity. The input-output characteristic of sample # 29, which was later employed in measurements together with the thermopile sensor, is illustrated in Fig. 3.8.
The output noise of the test-chip prototype was measured, with no signal and only the common-mode voltage applied, employing a Hewlett Packard 3589A Spectrum Analyzer. The result is shown in Fig. 3.9, which clearly verifies the chopper action as a peak is visible at 2 kHz, i.e. the chopping frequency. The other visible peaks are due to 50 Hz power supply disturbances. The measured input referred noise density at 100 Hz is 210 nV/$\sqrt{Hz}$: that, however, is con-

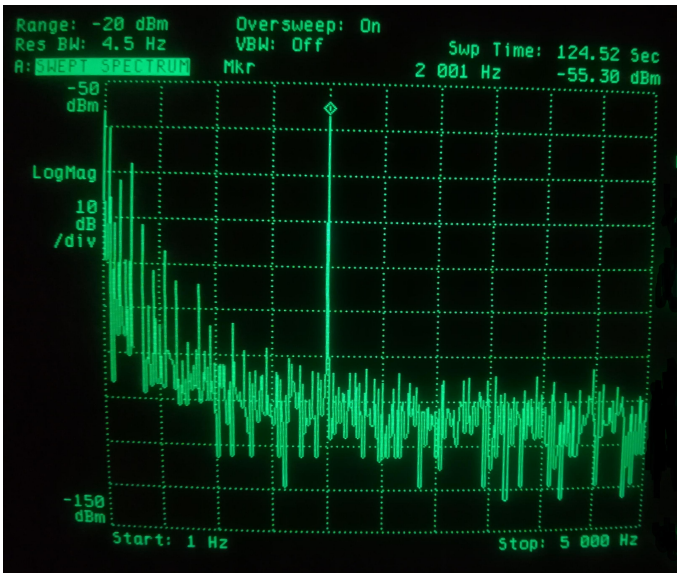

Figure 3.9: Measured output noise power of the proposed amplifier using a Hewlett Packard 3589A Spectrum Analyzer with 4.5 Hz resolution bandwidth (© 2019 IEEE) [23].

tributed also by the filter and by the buffer. As the noise due to the amplifier only, without the filter and buffer, cannot be measured, a *Cadence pnoise* simulation was performed in order to estimate it. The results are illustrated in Fig. 3.10. The simulated low-frequency input referred noise density, due to the amplifier only, is 86 nV/$\sqrt{Hz}$. To verify the reliability of the amplifier noise simulation, a *pnoise* simulation of the entire test chip was performed and the results were compared to the measurement obtained with the spectrum analyzer. The *pnoise* simulation returns the noise power spectral density, while the spectrum analyzer returns the noise power in dBm: in order to be able to compare the results, the simulated noise power spectral density was transformed into noise power, assuming a 4.5 Hz bandwidth as for the resolution bandwidth of the spectrum analyzer, and expressed in dBm. The result is shown in Fig. 3.11: it can be easily seen that the simulation and the measurement well match, apart from the peak at the chopping frequency. The difference in the peak amplitude is due to the fact that in simulations the flicker noise at DC, moved at the chopping frequency, is modeled as infinite and, therefore, ignored: only the noise at the near frequencies (e.g. 1.99 kHz, 2.01 kHz) is reported.
Tab. 3.2 illustrates the comparison between the proposed interface circuit and

Table 3.2: Comparison with state-of-the-art amplifiers suitable for thermocouple-based sensors (© 2019 IEEE) [23]

Parameter	**This work**	**[40]**	**[41]**	**[42]**
Year published	2019	2012	2016	2017
Technology	0.13-μm CMOS (ST)	0.7-μm CMOS	0.6-μ BiCMOS	0.32-μm CMOS (BCD6s ST)
Area [mm^2]	0.605 (0.0522 amplifier only)	1.8	1.626	0.57
Supply voltage [V]	1.2	5	1.8-to-5.5	3.3
Supply current [μA]	244 (210 amplifier only)	143	1650	170
Power consumption [μW]	292.8 (252 amplifier only)	715	2970 (with 1.8 V)	561
Chopping frequency [kHz]	2	30	150	20
Input offset standard deviation [μV]	1.365 (29 samples)	0.65 (12 samples)	–	2 (5 samples)
Input offset worst case [μV]	2.3 (29 samples)	<2 (12 samples)	3.5	–

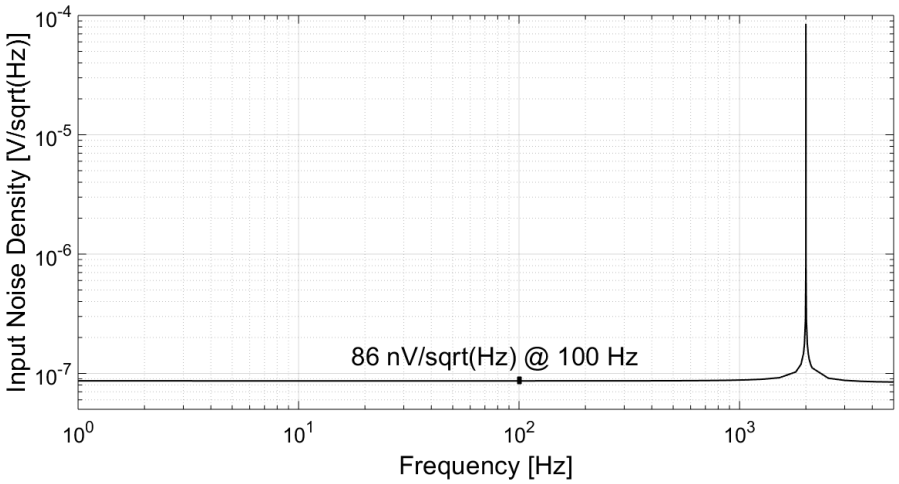

Figure 3.10: Simulated input referred noise density of the proposed amplifier (© 2019 IEEE) [23].

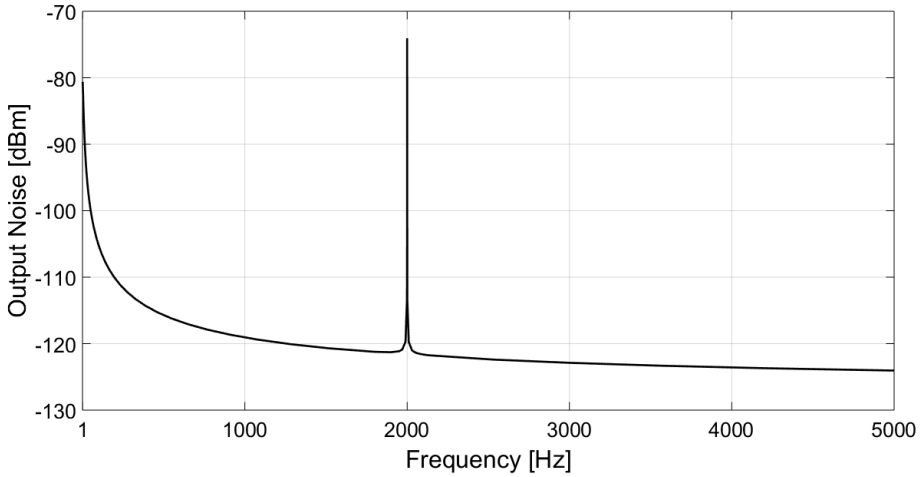

Figure 3.11: Simulated output noise power of the proposed test-chip prototype (© 2019 IEEE) [23].

other state-of-the-art amplifiers suitable for thermocouple-based sensors. The amplifier proposed in this work features the second best standard deviation, while the offset worst case is comparable with or even better than the other works. Moreover, as this work considered the highest number of samples, it

features the best statistical characterization. The power consumption is the lowest, also when considering the buffer: this makes the proposed circuit more suitable to mobile devices applications with respect to the other ones. Furthermore, the chip area is very limited.

3.3 Sensor-readout circuit system measurements

The proposed thermopile sensor and interface circuit, integrated in two separate test chips, were tested together as a system to perform both absolute temperature measurements for fever detection and presence detection for occupancy and intruder monitoring applications.
Although the sensor and the interface circuit are integrated and packaged into two separate chips, they could be packaged together in a cavity-LGA (Land Grid Array) structure, featuring a dedicated substrate design, a molded-cavity structure and a Si-based Infrared (IR) filtering window. Other, more diffused, solutions could be a metallic TO (Transistor Outline) or a ceramic package with an IR optical window as well.
In order to verify the correct operation for different room temperatures, the system, with the sensor having the perforated metal cap applied, was tested in a climatic chamber, employing a black body radiator (SR-800R 4D/A model by CI Systems [34]) as target object, placed at 10 cm from the sensor. The black body temperature was varied in ramp fashion from 20 °C to 50 °C and back, while monitoring the climatic chamber temperature. The system output signal, while applying a common mode voltage equal to 600 mV, was measured in the case of 20 °C and 35 °C ambient temperature in the climatic chamber: the results are illustrated in Fig. 3.12 and Fig. 3.13, respectively. The system output voltage acquisition was performed through a Keithley 2001 multimeter, coupled with a LabVIEW program, at a 5-Hz rate.
The system sensitivity, without removing the buffer offset, can be estimated as

$$S = \frac{Output\ Signal_{(T=50°C)} - Output\ Signal_{(T=20°C)}}{(50-20)°C} \tag{3.1}$$

where T is the target object temperature. It results in S = 6.90 mV/°C and S = 7.03 mV/°C for 20 °C and 35 °C, respectively: the system performance, therefore, is substantially independent of ambient temperature, while considering a typical range of room temperature values.

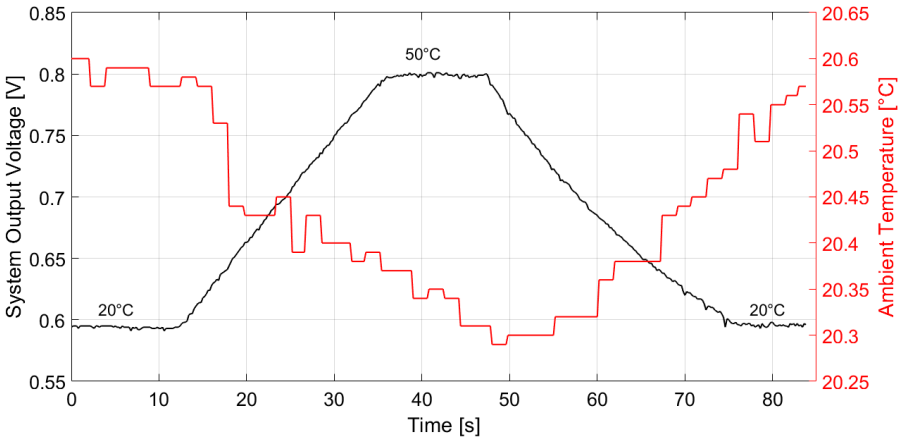

Figure 3.12: Measured thermopile sensor-interface circuit system output with the black body at 10-cm distance and the ambient temperature at 20 °C. The black body temperature is varied in ramp fashion from 20 °C to 50 °C. The buffer offset was not subtracted from the output signal (© 2019 IEEE) [23].

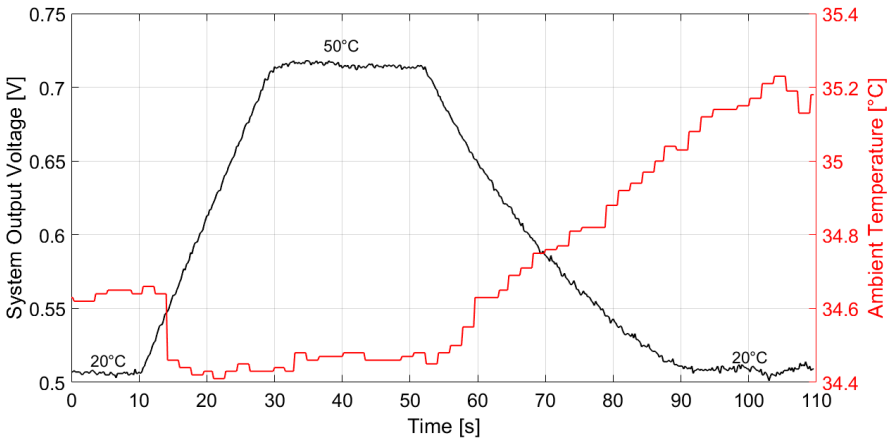

Figure 3.13: Measured thermopile sensor-interface circuit system output with the black body at 10-cm distance and the ambient temperature at 35 °C. The black body temperature is varied in ramp fashion from 20 °C to 50 °C. The buffer offset was not subtracted from the output signal (© 2019 IEEE) [23].

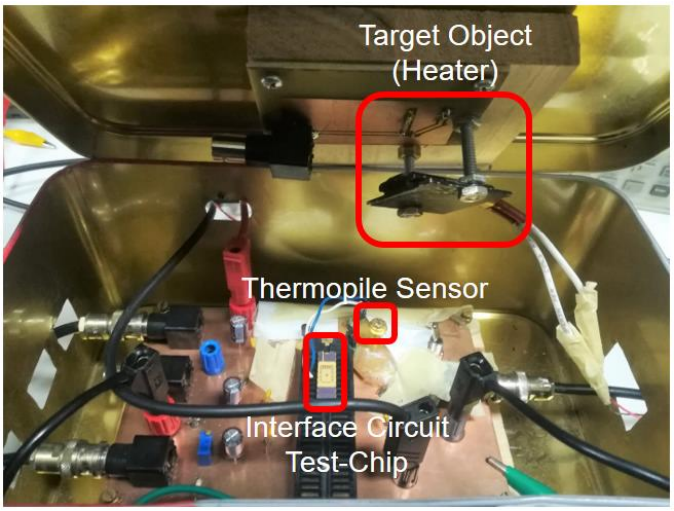

Figure 3.14: Measurement setup with the heater. When measurements are performed the box is closed and heater and sensor are aligned (© 2019 IEEE) [23].

3.3.1 Fever measurement application

The proposed amplifier circuit and the thermopile sensor were tested together as a system to verify the suitability for contact-less temperature measurements and in particular for human body temperature detection.
One terminal of the sensor was connected to the amplifier input, while the other was biased at the common-mode voltage, as was shown schematically in Fig. 3.3. The same measurement set-up as the one for the interface circuit characterization was employed.
A ΩDBK HPG Series PTC heater [45], whose temperature could be regulated by varying the applied voltage, was employed as a target object. The 4 cm × 3.5 cm heater was covered with opaque black paint in order to reduce its reflectivity, thus increasing its emissivity to resemble the one of an ideal black body: the target object emissivity was estimated to be 0.95, that is approximately equal to the average emissivity value for human skin. The board with the amplifier test-chip and the thermopile sensor was inserted into a metal box, in order to reduce disturbances and environmental noise. The heater was attached to the inside of the lid of the box by means of two screws: in this way, once the box was closed, the heater, acting as the target object, was located exactly in front of the sensor. The screws could be moved in order to regulate the distance between the heater and the lid, and therefore between

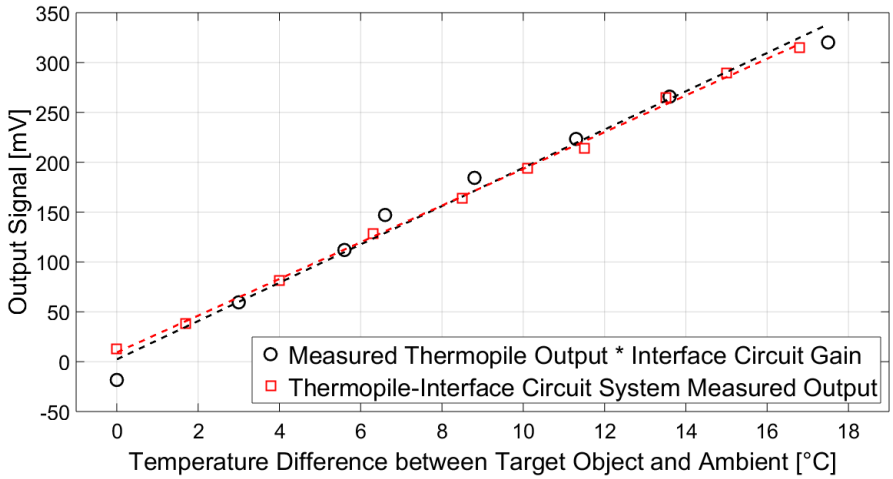

Figure 3.15: Comparison between the thermopile sensor-interface circuit system measured output and the measured thermopile output multiplied by the interface circuit gain. The measurements are performed with the target object at 3 cm distance (© 2019 IEEE) [23].

the heater and the thermopile sensor. The photograph reported in Fig. 3.14 illustrates the described set-up. A *surpeer* Infrared Thermometer (model IR5D) was employed to measure the box, and therefore the ambient, temperature.
Sample # 29 of the proposed amplifier test-chip prototype, which was previously fully characterized, was employed for these measurements. In all the reported results, unless otherwise stated, the common-mode voltage and the buffer offset were measured and subtracted from the output voltage measurement: the reported values, therefore, show only the signal. Each measurement was performed acquiring 100 samples with the multimeter at 1.25-Hz rate (i.e. the *slow rate* of the instrument): the samples were stored in the multimeter buffer, which then returned the average value, that is the value considered for each measurement. Furthermore, the measurements were performed at approximately 25-°C ambient temperature and with no cap on the thermopile sensor (120° FOV).
In order to verify that the thermopile sensor output voltage is correctly amplified by the interface circuit, the measured output voltage at the output of the sensor-interface circuit system was compared with the measured output of the thermopile sensor only, multiplied by the amplifier measured gain. The measurements were performed with the target object, i.e. the heater, at a 3-

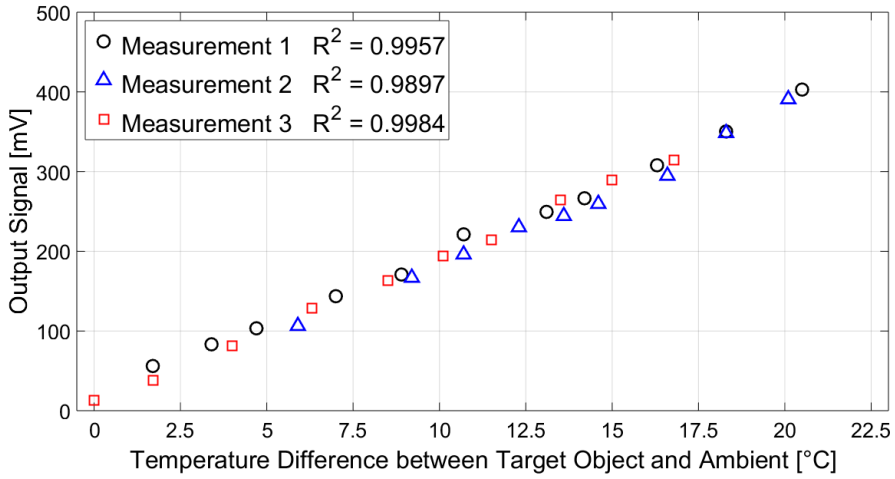

Figure 3.16: Repeated measurements of the thermopile sensor-interface circuit system output with the target object at 3-cm distance. R^2 is the squared linear correlation coefficient (© 2019 IEEE) [23].

Table 3.3: Derived sensitivity for the thermopile sensor-interface circuit system output for different target object distances (© 2019 IEEE) [23]

Distance	**Squared Linear Correlation Coefficient R^2**	**Derived Sensitivity**
1.5 cm	0.9969	35.25 mV/°C
2 cm	0.9951	29.66 mV/°C
3 cm	0.9984	18.40 mV/°C

cm distance from the sensor. As can be seen in Fig. 3.15, the results almost perfectly match.
Repeatability, required for human body temperature detection, was verified by performing several measurements under the same conditions. The results in the case of 3-cm distance between sensor and target object are reported in Fig. 3.16: very good repeatability can be inferred. R^2 is the squared linear correlation coefficient between the temperature difference and the measured signal and, being approximately equal to 1, shows almost ideal linearity in the considered temperature range.
Measurements at different distances were performed to investigate the sensor sensitivity: the results are shown in Fig. 3.17. The sensitivity for the different distances cases is reported in Tab. 3.3. The sensitivity was derived assuming a linear approximation: this was legitimate as the squared linear correlation

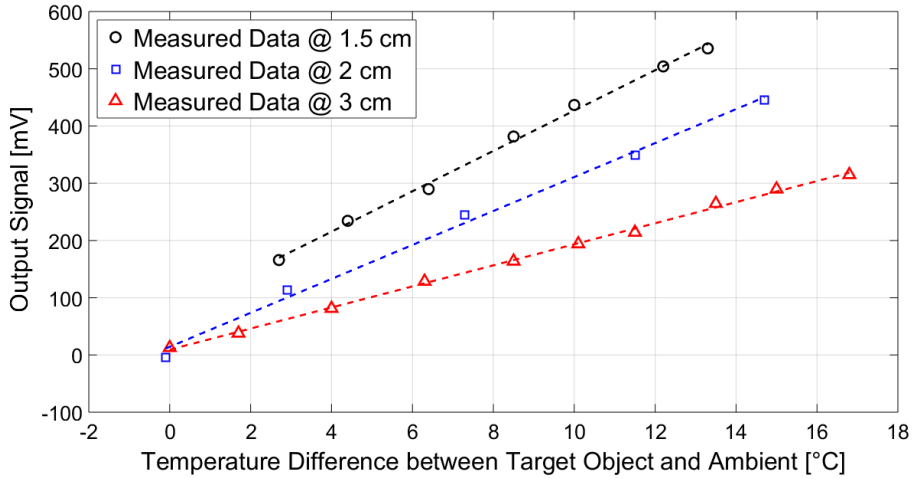

Figure 3.17: Measured thermopile sensor-interface circuit system output with the target object at different distances. The FOV is 120°C (© 2019 IEEE) [23].

Table 3.4: Comparison between measurement results and the expected results considering the thermopile sensor model at different target object distances (© 2019 IEEE) [23]

Distance	**Measured Sensitivity**	**Expected Sensitivity**	R^2
1.5 cm	35.25 mV/°C	37.45 mV/°C	0.9960
2 cm	29.66 mV/°C	28.30 mV/°C	0.9917
3 cm	18.40 mV/°C	18.57 mV/°C	0.9978

coefficient indicates almost ideal linearity. Employing the model described by equations (1.9)-(1.10)-(1.11), the sensitivity values were calculated assuming a circular target object of equivalent area. The calculated values, together with the ones derived from measurements, are reported in Tab. 3.4: the model is a good fit, as proved by the coefficient of determination R^2.
Measurements performed without any thermopile cap suffer from high standard deviation, ranging from 5 to 15 mV, and, therefore, poor measurement accuracy, while accuracy within ±0.3 °C is required for human body temperature detection. This measurement degradation is due to environmental noise: in order to reduce it, a perforated metal cap, as the one used for the thermopile sensor characterization, was added to the thermopile sensor. The cap determined a 51.64° FOV angle.
Fig. 3.18 illustrates the response of the system, with the metal cap, to a tem-

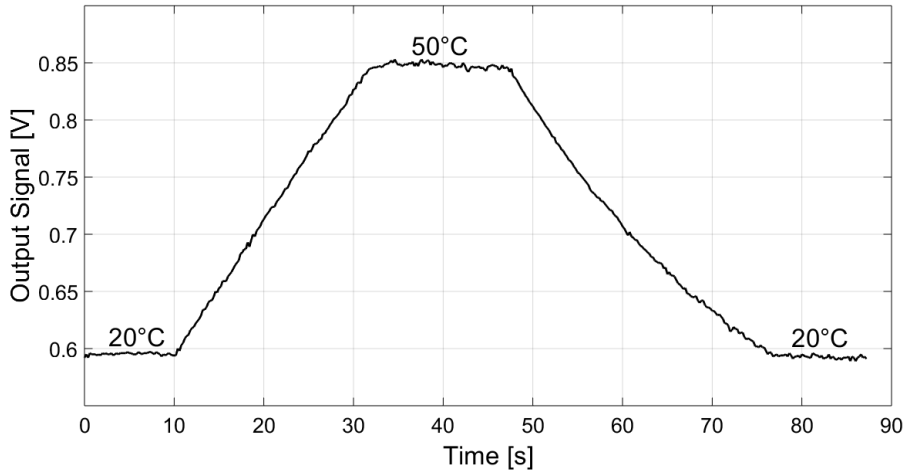

Figure 3.18: Measured thermopile sensor-interface circuit system output with the black body at 5-cm distance, with a cap determining a 51.64° FOV angle. The black body temperature is varied as a ramp from 20 to 50 °C. The buffer offset was not subtracted from the output (© 2019 IEEE) [23].

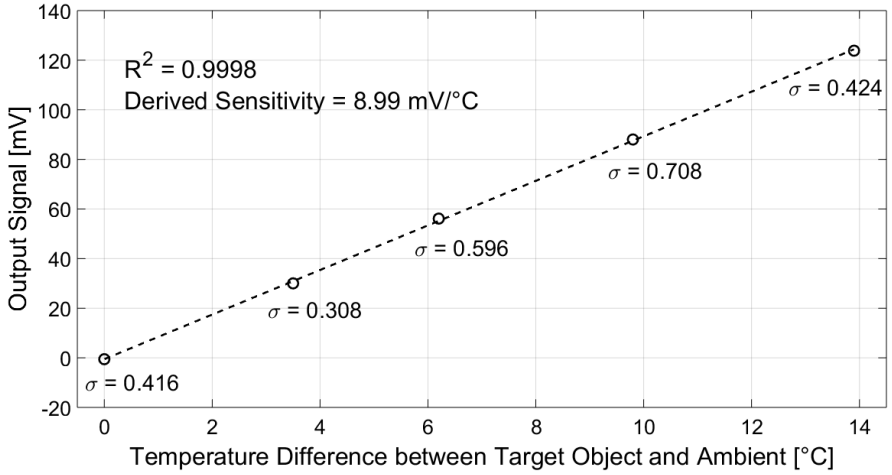

Figure 3.19: Measured thermopile sensor-interface circuit system output with the target object at 3-cm distance, with a cap determining a 51.64° FOV angle. The standard deviation σ associated to each measure is expressed in mV (© 2019 IEEE) [23].

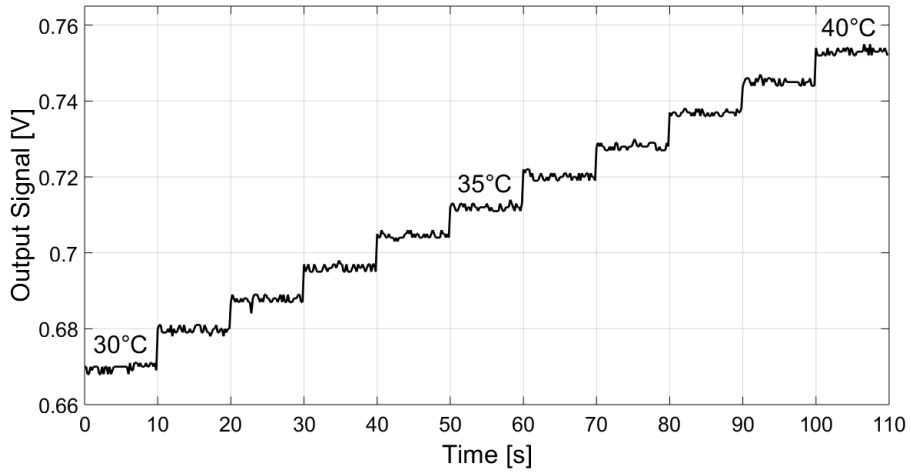

Figure 3.20: Measured thermopile sensor-interface circuit system output with the black body at 5-cm distance, with a cap determining a 51.64° FOV angle. The black body temperature is varied from 30 to 40 °C with 1 °C steps. The buffer offset was not subtracted from the output (© 2019 IEEE) [23].

perature variation of the black body, at an ambient temperature equal to 20 °C. The black body is positioned at 5 cm from the sensor and its temperature varies from 20 to 50 °C in a ramp fashion, while the output signal is acquired through the Keithley multimeter and a LabView program at a 5-Hz sampling rate. It is evident that the cap has no effect on linearity, while it reduces the sensitivity: this is further illustrated in Fig. 3.19, which shows the measurement results with the considered cap and 3-cm distance between the sensor and the heater as target object. As the squared linear correlation coefficient is 0.9998, almost ideal linearity is maintained, while the sensitivity is reduced from 18.40 mV/°C, when no cap is applied under the same conditions, to 8.99 mV/°C. As the effective portion of the object seen by the detector is smaller, the sensitivity reduction is actually expected. As the environmental noise is also limited, however, the measurement standard deviation, σ, diminishes as well: it ranges from 0.308 to 0.708 mV in the reported case. The standard deviation reduction is much more consistent than the sensitivity reduction and, therefore, allows an overall improvement in the measurement accuracy: considering $\pm 2\sigma$, the maximum temperature error is ± 0.16 °C, which is perfectly within the accuracy required for human body temperature detection.

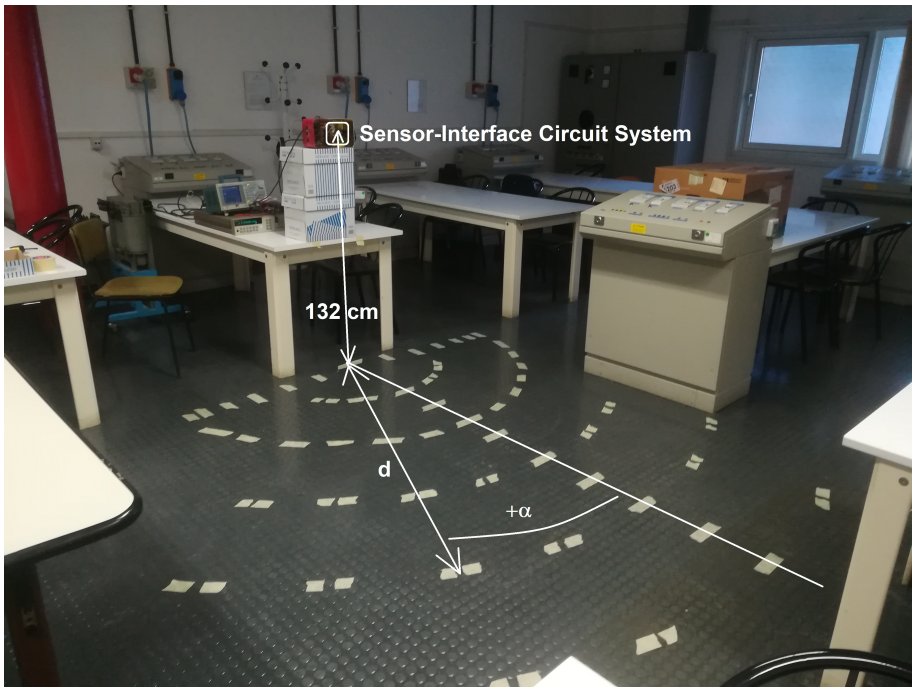

Figure 3.21: Room used for presence detection testing of a stationary subject. The signs on the floor identify the various considered person's locations [29].

The aptness of the system for human body temperature detection is illustrated also in Fig. 3.20, which shows the system response to a black body temperature variation from 30 to 40 °C in 1 °C steps, at 20 °C ambient temperature: the output at different black body temperatures is clearly distinguishable. As for the measurement of Fig. 3.18, the output signal acquisition was performed through the Keithley multimeter and a LabView program at a 5-Hz sampling rate.

3.3.2 Presence and motion detection application

The sensor-interface circuit system was tested for presence detection of stationary subjects, considering a person standing in a room at various distances d and angles α from the sensor. The sensor, with the metal cap, and the interface circuit, inserted in their respective boards and connected together, were placed at a 132-cm height from the ground, facing the room. Several different locations, identified by d and α and signaled on the floor by means of white tape, were considered, as illustrated in Fig. 3.21. The chosen locations are

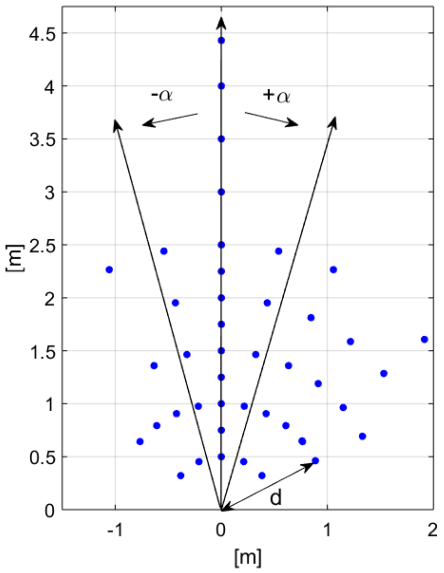

Figure 3.22: Person's locations in the room considered for presence detection testing of a stationary subject [29].

reported in Fig. 3.22.
The supply voltage for the interface circuit, equal to 1.2 V, was provided through an Agilent E3631A power supply, while a Hewlett Packard 3245 universal source supplied the common-mode voltage, equal to 600 mV. The circuit bias current was regulated through a resistor on-board and set equal to approximately 70 μA. A Tektronix AFG3252 function generator supplied the 2-kHz 0-1.2-V square wave clock signal for the chopper. A Keithley 2000 multimeter was employed to measure the system output voltage. The schematic view of the measurement setup is illustrated in Fig. 3.23.
The measurements were performed at 22 °C room temperature, considering a 1.75-m average-build man as the stationary subject. For each identified location, 100 output acquisitions at 1.25 Hz (i.e. the multimeter *slow rate*) were performed considering both the case with the person standing and the empty room case. The measurement results for each case were stored in the buffer of the multimeter, which then returned the average and standard deviation value. The difference between the average in the occupied room case and in the empty room case was then considered as the output signal of interest.
The output signal in the case of a subject at a fixed 1-m distance and different

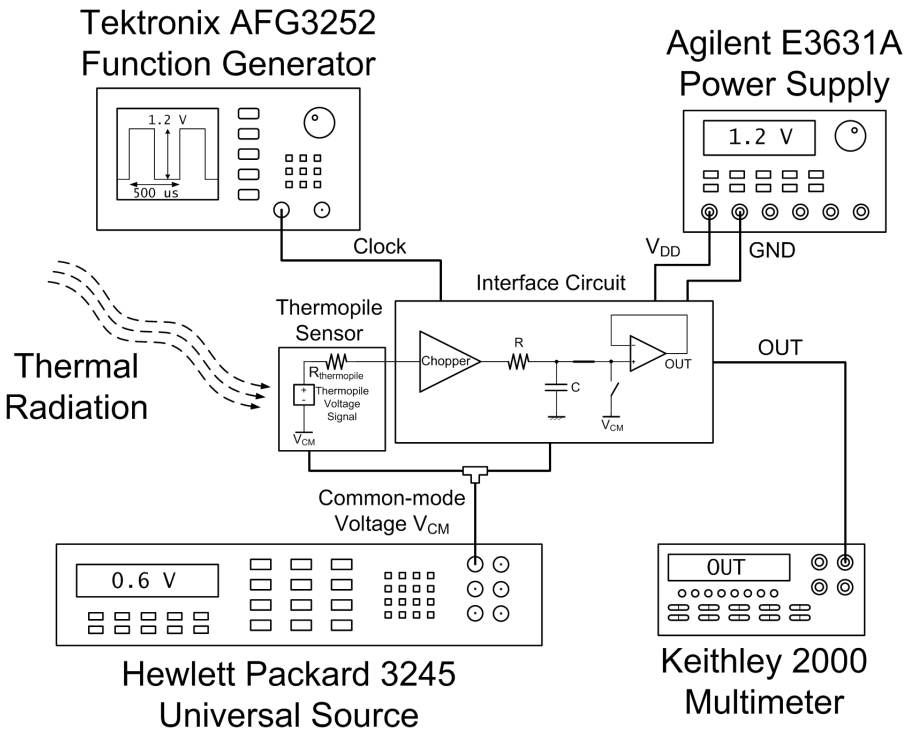

Figure 3.23: Schematic view of the measurement setup [29].

angles from the sensor is reported in Fig. 3.24. The fitted curves for positive and negative values of α share the same shape and are clearly superimposable, therefore the measurements are symmetrical. However, as the curves are not coincident and differ in average for a -13° shift between the positive and the negative angle curves, they are not symmetrical across the line previously identified as corresponding to 0°: this is due to the fact that the chosen 0°-line is not perpendicular to the sensor surface because of alignment inaccuracies during the setup.
In order to have the actual sensor's normal line as reference, the following angle correction was performed:

$$\alpha_{corrected} = \alpha - \theta \tag{3.2}$$

where

$$\theta = \frac{Average\ difference\ between\ positive\ and\ negative\ angle\ curves}{2} \tag{3.3}$$

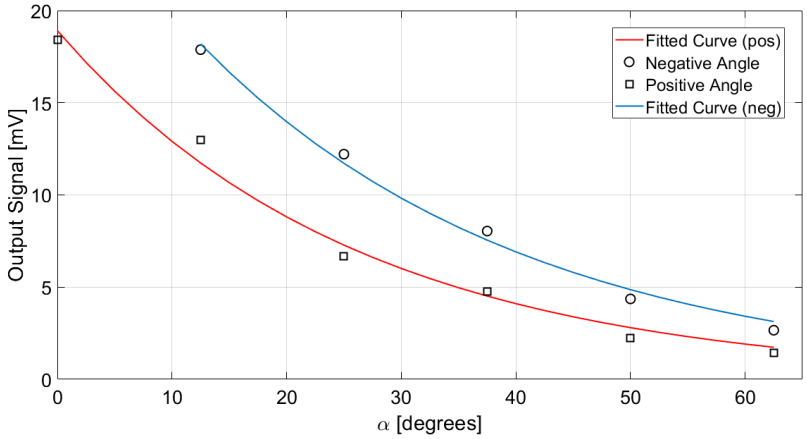

Figure 3.24: Signal in the case of a person standing at d = 1 m from the sensor for different values of α [29].

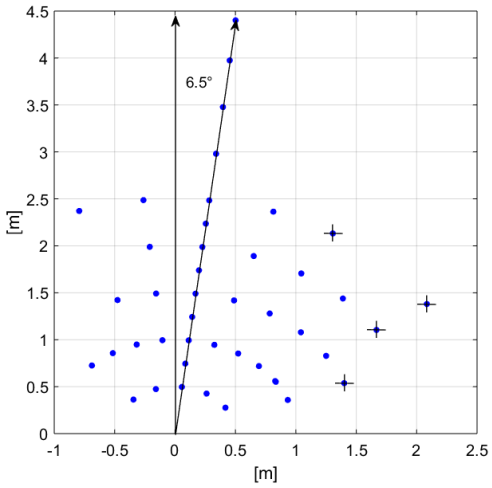

Figure 3.25: Person's locations in the room considered for presence detection testing of stationary subjects, applying the angle correction [29].

$$\theta = \frac{-13^\circ}{2} = -6.5^\circ \tag{3.4}$$

Fig. 3.25 illustrates the standing subject locations referred to the sensor's normal. The points with a cross indicate that the system was not able to

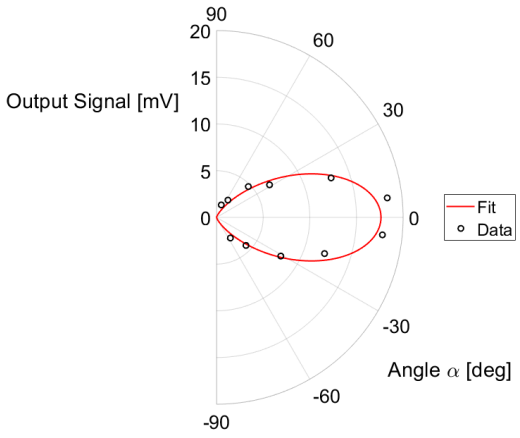

Figure 3.26: Graphical comparison between the derived fit and the measured data in the case of 1-m fixed distance [29].

detect the subject presence in that location. Presence detection was considered achieved if a positive output signal was found considering a $\pm 2\sigma$ variation across the 100 acquired samples for each location. The measured sensor FOV is equal approximately to 120° at 1-m distance.
Taking into account the angle correction, the dependency on both the angle, $\alpha_{corrected}$, and the distance, d, of the subject from the sensor was investigated in order to derive the best fit for the measurement results. The Matlab Curve Fitting Tool was employed in the process.
Considering the results for 1-m fixed distance and different angle values, the identified fit function is

$$Output\ Signal = c_{a1}\ (cos\ \alpha_{corrected})^{c_{a2}} \tag{3.5}$$

where c_{a1} and c_{a2} are equal to 17.63 and 4.766, respectively, considering 95% confidence bounds. The fit yields a correlation with R-squared equal to 0.9621 and a root mean square error (RMSE) equal to 1.262. A graphical representation of the measured data and the derived fit is reported in Fig. 3.26.
The value of c_{a2} well matches with the expected value from the theory: in the case of extended lambertian sources (e.g. the human body) parallel to the detector, in fact, the radiant intensity is proportional to $(cos\ \alpha_{corrected})^4$ [46].
Considering instead the measurements results for a 6.5° fixed angle at various distances, the derived fit function is

$$Output\ Signal = \frac{c_{d1}}{d^{c_{d2}}} \tag{3.6}$$

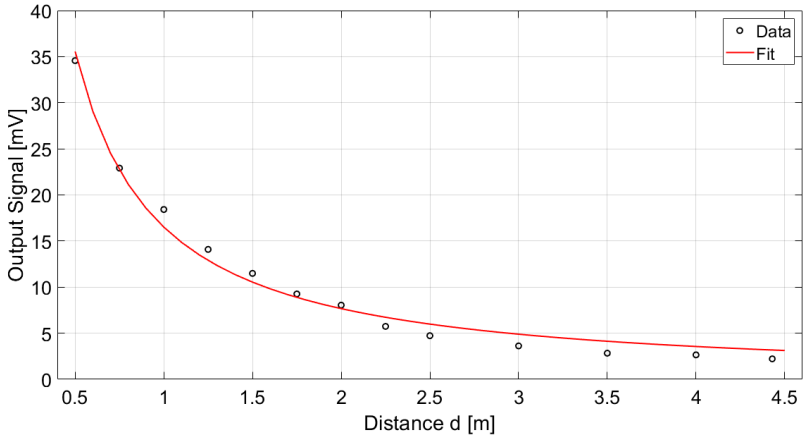

Figure 3.27: Graphical comparison between the derived fit and the measured data in the case of 6.5° fixed angle [29].

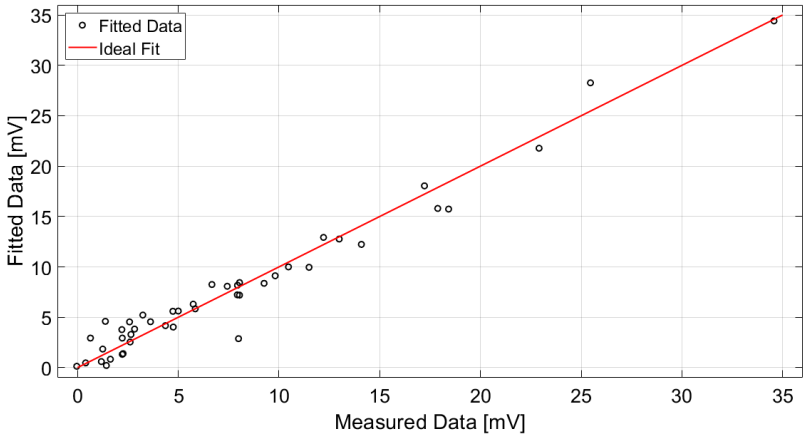

Figure 3.28: Graphical comparison between the derived fit and the ideal fit [29].

where c_{d1} and c_{d2} are equal to 16.51 and 1.107, respectively, considering 95% confidence bounds. The R-squared coefficient and the RMSE are equal to 0.9866 and 1.163, respectively. Fig. 3.27 illustrates a graphical representation of the measured data and the derived fit.
The derived curves well fit the measured data in the fixed-distance/variable-angle and fixed-angle/variable-distance cases; the fit shape in the case of both

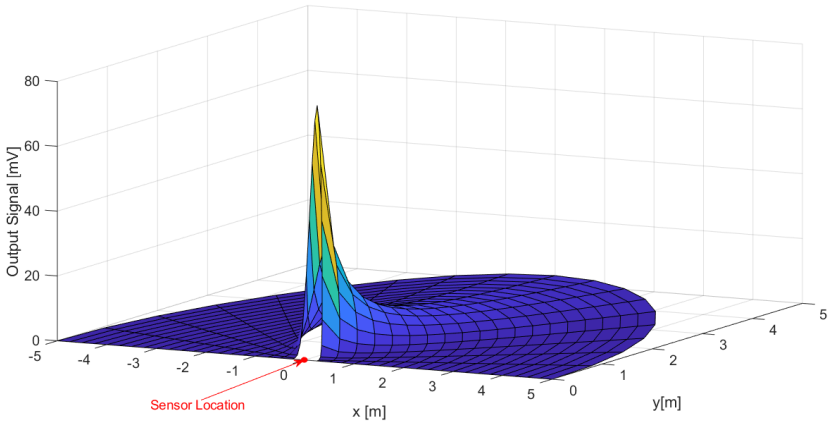

Figure 3.29: 3-D graphical representation of the derived fit in cartesian coordinates [29].

variable angle and variable distance, therefore, was chosen equal to the product between the two curves shapes. The derived fit function is

$$Output\ Signal = c_1\ (cos\ \alpha_{corrected})^{c_2}\ \frac{1}{d^{c_3}} \tag{3.7}$$

where c_1=16.17, c_2=4.222 and c_3=1.129, with 95% confidence bounds. The fit yields 0.9599-R-squared and 1.52-RMSE: it is therefore a good approximation for the measurements results, as shown in Fig. 3.28.
The 3-D representation of the derived fit as a function of the stationary subject location, expressed in a cartesian coordinate system where the y-axis is the normal to the sensor surface, is illustrated in Fig. 3.29.
A 2-D representation of the sensor detection range, derived from the obtained fit, with isolines corresponding to 10 mV, 5 mV, 2 mV and 1 mV output signal acting as delimiters, is reported in Fig. 3.30. The derived FOV well satisfies the specifications for the targeted applications, which require a short-distance (few meters) detection capability. The maximum measured detection distance in the considered setup was 4.43 m. The limit, however, was imposed by the room size: therefore, in order to verify fully the sensor detection capability, the setup was moved to a larger room and the measurements for a 0°-line were repeated, considering a 1.65-m average-build woman as the stationary subject.

Considering a $\pm 2\sigma$ variation as stated before, a positive output signal was found for distances up to 5.5 m.

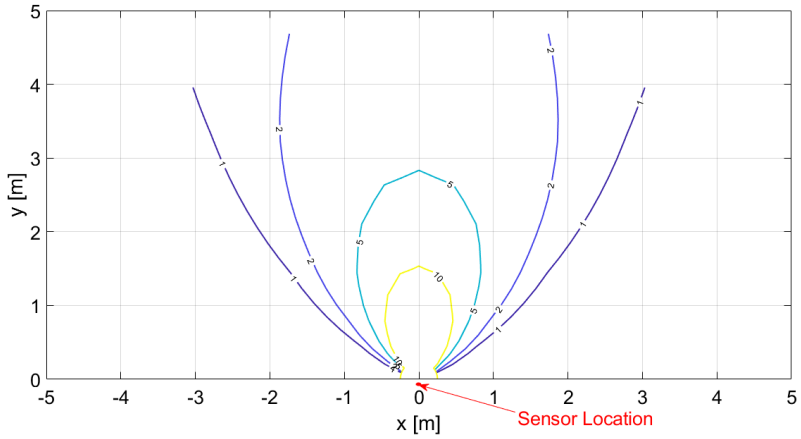

Figure 3.30: 2-D representation of the sensor detection range, obtained from the derived fit. The reported lines are the isolines corresponding to an output signal equal to 10 mV, 5 mV, 2 mV and 1 mV [29].

Employing the Matlab Curve Fitting Tool, adopting the same fit function as for the other measurements set, the fit for the measured output signal as a function of the distance was derived

$$Output\ Signal = \frac{c_{d1}}{d^{c_{d2}}} \tag{3.8}$$

where c_{d1}=25.71 and c_{d2}=1.07, with 95% confidence bounds. R-squared and the RMSE are equal to 0.9627 and 2.995, respectively.
The correlation coefficient, R-squared, between the fit functions of the two measurements sets in the fixed-angle/variable-distance case is 0.9999: the measurements, therefore, are clearly repeatable, even when varying the room setting and the stationary subject.
The system performance in the presence of moving subjects was also tested. The same room setup illustrated in Fig. 3.21 was adopted and a 1.70-m average-build woman was considered as moving subject. The subject moved in a straight line, approximately perpendicular to the sensor's normal, at different distances from the sensor. The measurements were performed acquiring the system output voltage through a Keithley 2000 multimeter, paired with a LabVIEW program. The chosen acquisition rate was 5 Hz when the subject was walking and 10 Hz when the subject was running. A common-mode voltage equal to 600 mV was supplied through the universal source. The ambient temperature was roughly equal to 26.5 °C. Fig. 3.31 illustrates the measurements results when the subject is walking at 1 m from the sensor, which is

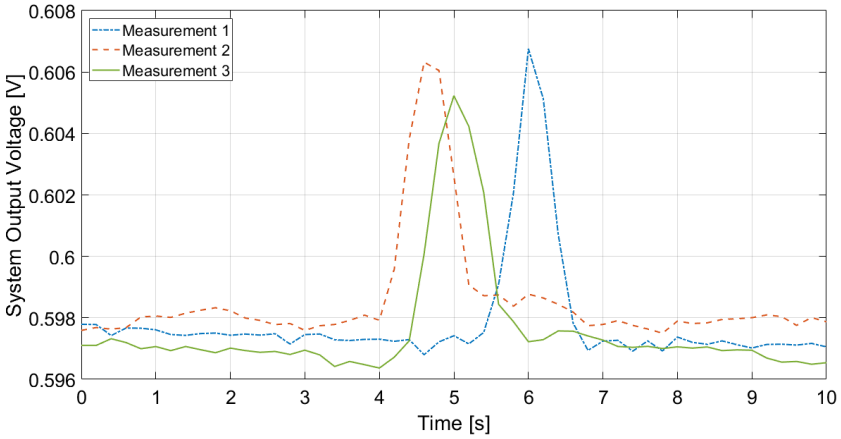

Figure 3.31: Measuremets results in the case of a subject walking at 1 m in front of the sensor. The sensor is located at a 132-cm height from the ground.

located at a 132-cm height from the ground. The system performance is validated as a peak, corresponding to when the subject moves within the sensor FOV, is clearly distinguishable. Different measurements were performed and repeatability was verified.
Furthermore, the system performance was investigated considering a larger distance, different sensor's height from the ground and different subject's speed (walking or running). The results are reported in Fig. 3.32 and Fig. 3.33, which illustrate the measurement results when the subject is, respectively, walking and running at 2.5 m from the sensor, when that is located at 132-cm and 109-cm height from the ground: the peak, which detects the subject presence, is clearly visible in all cases. As expected, the peak lasts longer when the subject is walking as in that case the subject, being slower, remains longer within the sensor FOV. Furthermore, considering the same subject speed, the peak at 2.5 m lasts longer than the one for 1 m: this is due to the fact that the area covered by the sensor at a given distance corresponds to the section of a solid angle and, therefore, the one at 2.5 m is larger than the one at 1 m; hence, the subject remains in the sensor FOV longer.
It is to be noted that the system output voltage when no subject is detected varies of a few mV from one measurement to the other: this is simply due to the fact that the measurements were performed at different moments and, therefore, were subject to temperature variations in both the ambient and the sensor, that, however small, given the sensor excellent responsivity and therefore sensitivity, would result in a voltage difference. However, this is not

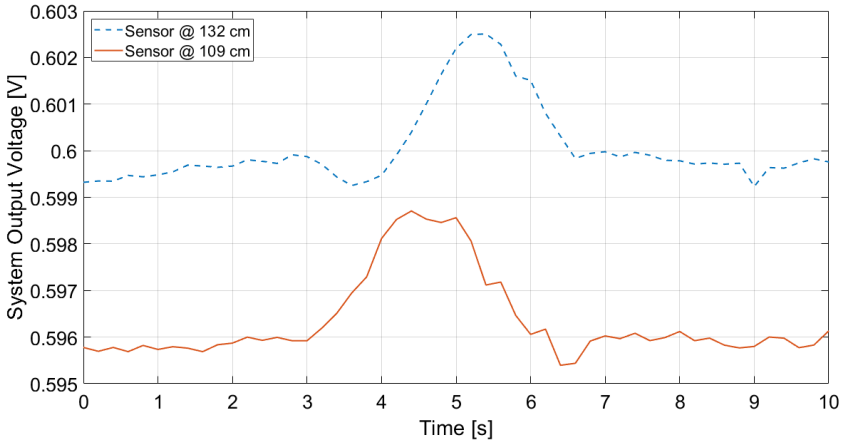

Figure 3.32: Measurement results in the case of a subject walking at 2.5 m in front of the sensor, for different sensor heights.

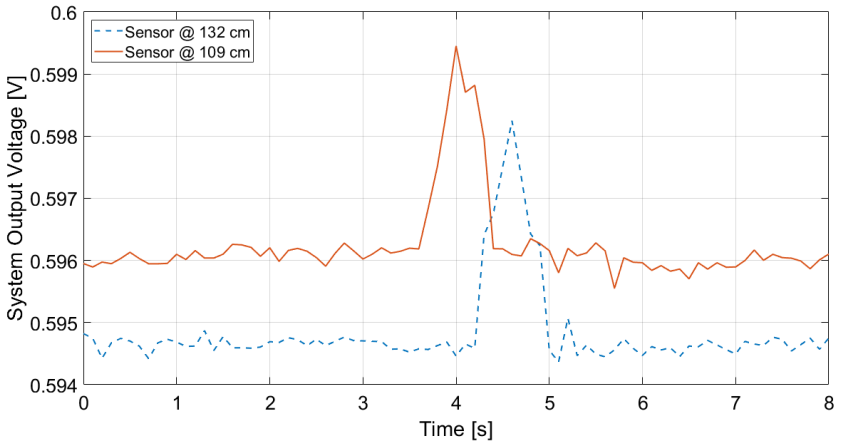

Figure 3.33: Measurement results in the case of a subject running at 2.5 m in front of the sensor, for different sensor heights.

an issue: the peak, in fact, is the one that enables presence detection; we are, therefore, interested in the relative variation of the system output voltage, not in its absolute value.

Chapter 4

TMOS sensor

As stated in Chapter 1, the TMOS performance depends on the transistor operating region, as well as on its configuration. Subthreshold was chosen as operating region, as it yields the best sensitivity value. Regarding the choice of the configuration, different possibilities were investigated relying on characterization measurements previously performed by STMIcroelectronics and on *Cadence* simulations. Voltage-mode, and not current-mode, readout configurations were considered in order to be able to directly compare the TMOS performance with the one of the micromachined polysilicon thermopile, which, given its characteristics, only supports voltage-mode readout. The thermopile measured voltage sensitivity to target temperature variations, which constitutes the benchmark to choose the best configuration for the TMOS, is 90 μV/°C, as reported in Section 3.3.1, considering a heater of 2.11-cm equivalent radius and a 3-cm distance between detector and target object.
For simulating the TMOS, the model of 1.4.2 was employed.
Section 4.1 reports the TMOS configuration analysis which brought to the choice of the configuration adopted in this work, while Section 4.2 illustrates the designed TMOS bias circuit. Section 4.3 reports the TMOS characterization measurement results.

4.1 TMOS configuration analysis

For both two-terminals (2T, diode-like) and three-terminals (3T, with bulk and source connected together in the schematic) configurations, as the signal produced by the TMOS is several orders of magnitude smaller than the DC signal, a fully differential readout circuit configuration is required to cancel the

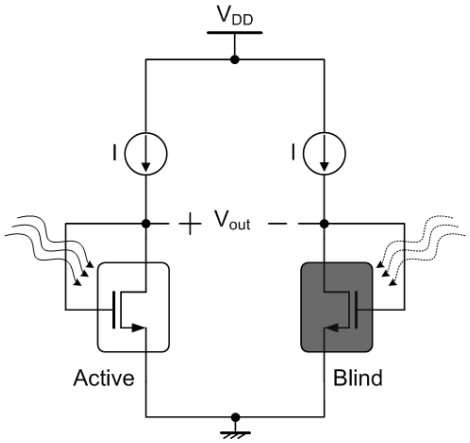

Figure 4.1: 2T TMOS voltage-mode readout configuration.

large common-mode voltage, as well as any self-heating effect [47]. The fully differential readout circuit employs two TMOS sensors: one "active" and one "blind". The active sensor is able to "see" the target object and, therefore, absorb its thermal radiation, while the blind sensor, being covered by a mirror, "sees" only itself and acts as reference. The differential voltage between the drain terminals of the active and blind transistors can then be processed through a low-offset, low-noise amplifier and subsequent analog-to-digital conversion chain.
Considering the voltage-mode readout configuration and the small-signal equivalent circuit for the TMOS, illustrated in Section 1.4.1, the sensitivity to the target temperature variation is given by

$$S_{V,\ target} = -Z_{out}\ S_{I,\ target} \tag{4.1}$$

where Z_{out} is the voltage-mode readout circuit output impedance. Hence, in order to achieve a $|S_{V,\ target}|$ value better then the one of the micromachined thermopile sensor considered as benchmark, i.e. 90 μV/°C, the following condition must hold

$$Z_{out} \geqslant \frac{90\ \mu\text{V/°C}}{S_{I,\ target}} \approx 120\ \text{k}\Omega \tag{4.2}$$

The voltage sensitivity $S_{V,\ target}$, therefore, depends only on the readout output impedance, once the transistor operating point has been chosen: the current sensitivity $S_{I,\ target}$, in fact does not change.
The 2T configuration, employing the active and blind sensors with a diode-like connection, is illustrated in Fig. 4.1: the supply voltage V_{DD} is set to 1.2 V

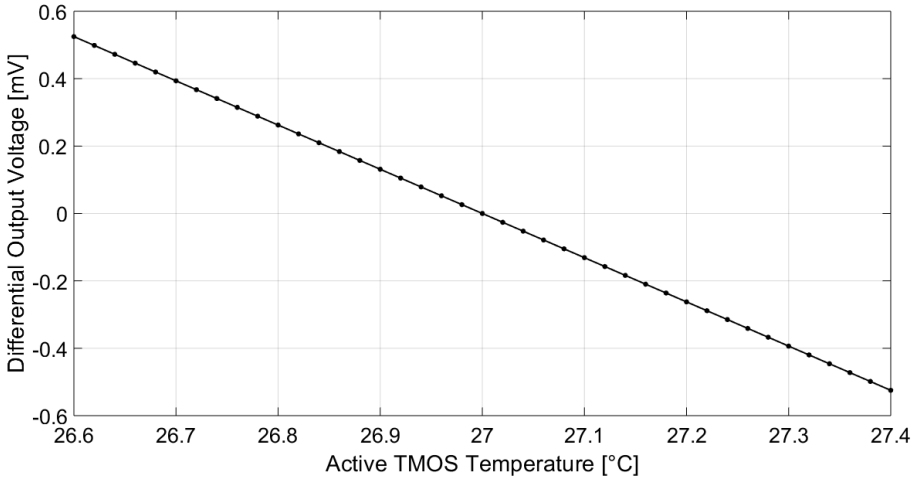

Figure 4.2: Simulated differential output voltage for a 2T voltage readout configuration, in the case of a ±0.4 °C TMOS temperature variation around room temperature, which corresponds to a ±20 °C target object temperature variation.

and the biasing current I to 1 μA. The simulated differential output voltage V_{out}, obtained varying the active TMOS temperature through the MTS option and keeping the temperature of the rest of the circuit constant and equal to 27 °C, is reported in Fig. 4.2. The active TMOS temperature variation, equal to ±0.4 °C around room temperature, corresponds to a ±20 °C target temperature variation. The derived $S_{V,\,TMOS}$ and $S_{V,\,target}$ values are 1.312 mV/°C and 26.24 μV/°C, respectively. The TMOS employing this readout configuration is therefore clearly worse in terms of performance than the thermopile sensor. The readout circuit output impedance Z_{out} in this configuration, in fact, is approximately $1/g_m \approx 35$ kΩ, which is significantly lower than the 120 kΩ required to match the thermopile performance. Hence, even if this configuration has been previously employed in different solutions [47–49], it is not the optimal one as it fails to fully exploit the sensor advantages, in particular its sensitivity.
The 3T configuration, with bulk and source terminals connected together, is reported in Fig. 4.3: the gate voltage V_G, set to 287 mV, determines a transistor biasing current equal to 1 μA, while the resistance R is chosen equal to 600 kΩ, in order to set the common mode voltage to 600 mV. Fig. 4.4 reports the simulated differential output voltage V_{out}, obtained again varying the active

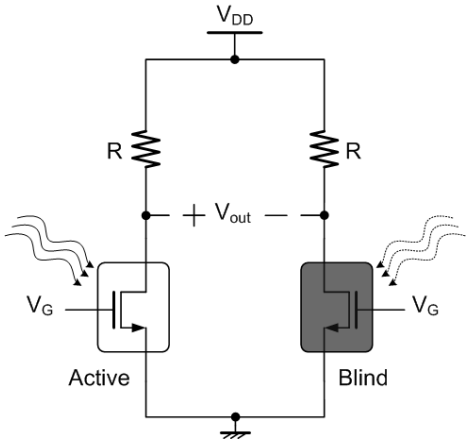

Figure 4.3: 3T TMOS voltage-mode readout configuration.

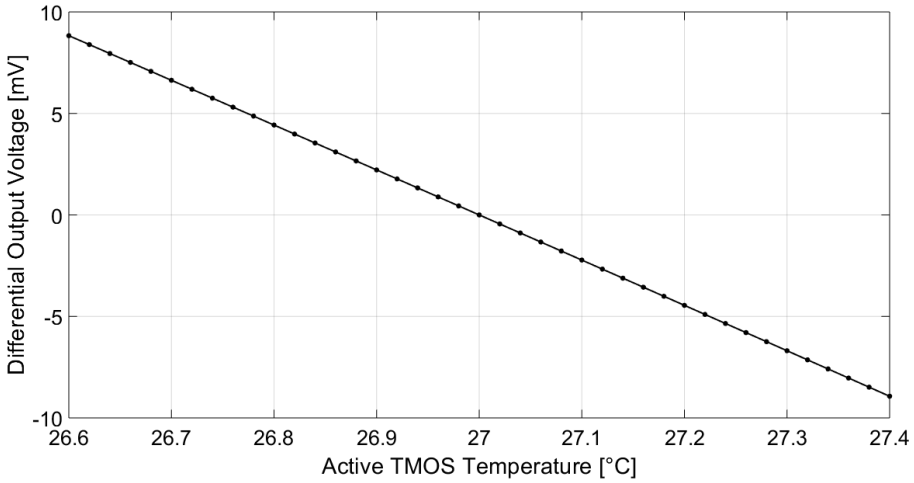

Figure 4.4: Simulated differential output voltage for a 3T voltage readout configuration, in the case of a ±0.4 °C TMOS temperature variation around room temperature, which corresponds to a ±20 °C target object temperature variation.

TMOS temperature through the MTS option while keeping the temperature of the rest of the circuit constant and equal to 27 °C. The derived $S_{V,\ TMOS}$ and $S_{V,\ target}$ values are -22.21 mV/°C and -444.2 μV/°C, respectively. The TMOS in 3T configuration is, therefore, significantly better than the thermopile sensor

Table 4.1: Comparison with Other Readout Configurations for the TMOS

	This work 3T	**This work 2T**	**[47] 2T**	**[48] 2T**
Op. Region	Subth.	Subth.	Sat.	Subth.
$\lvert S_{V,\ TMOS}\rvert$ [mV/°C]	22.17	1.31	4.00	15.00
V_{DD} [V]	1.2	1.2	2.5	2.5
$I_{DS,\ TMOS}$ [μA]	1	1	50	–
Consumption [μW]	2.4	2.4	250	–

assumed as benchmark: in the 3T case, in fact

$$Z_{out} = R//r_o \approx R = 600\ k\Omega \tag{4.3}$$

as r_o is larger than 55 MΩ.
This configuration, which has been previously considered only for current-mode readout [47], therefore clearly proves to be the most performing also for voltage-mode, as, contrary to the 2T, it successfully exploits the transistor internal gain. Furthermore, employing resistances instead of an active load guarantees a benefit also in terms of noise. The voltage sensitivity $S_{V,\ TMOS}$, moreover, is sufficiently stable with respect to temperature, as illustrated in Fig. 4.5. $\frac{d^2 I_{DS}}{dT^2}$ is approximately equal to -648 μV/°C^2, which corresponds to 2.9%/°C, obtained as $\frac{d^2 I_{DS}}{dT^2} / \frac{dI_{DS}}{dT}$. The only drawback of this configuration is the fact that the gate voltage V_G must be precisely set and controlled in order to obtain the desired bias current and common-mode voltage. To solve this problem, a current sink can be added to bias the transistors, as shown in Fig. 4.6: in this way the common source node has the freedom to move when the gate voltage varies, while maintaining the bias current, and consequently the common mode-voltage, constant, thus ensuring a more robust design.
The voltage-mode readout circuit configuration with the current sink, illustrated in Fig. 4.6, where $V_{DD} = 1.2$ V, $R = 600$ kΩ, $I = 2$ μA and $V_G = 520$ mV is, therefore, the optimal one as it allows well controlling the transistor operating point, while maintaining the voltage sensitivity value high. The derived TMOS voltage sensitivity $S_{V,\ TMOS}$ is -22.17 mV/°C ($S_{V,\ target} = -443.4$ μV/°C), substantially the same of the 3T configuration with the common source connected to ground, while $\frac{d^2 I_{DS}}{dT^2}$ is further reduced to 74 μV/°C^2, which corresponds to 0.3%/°C, yielding even better voltage sensitivity stability with respect to temperature. A low-offset low-noise amplifier and an analog-to-digital converter to enable the signal processing complete the readout system.
A comparison between the proposed optimal 3T configuration and different

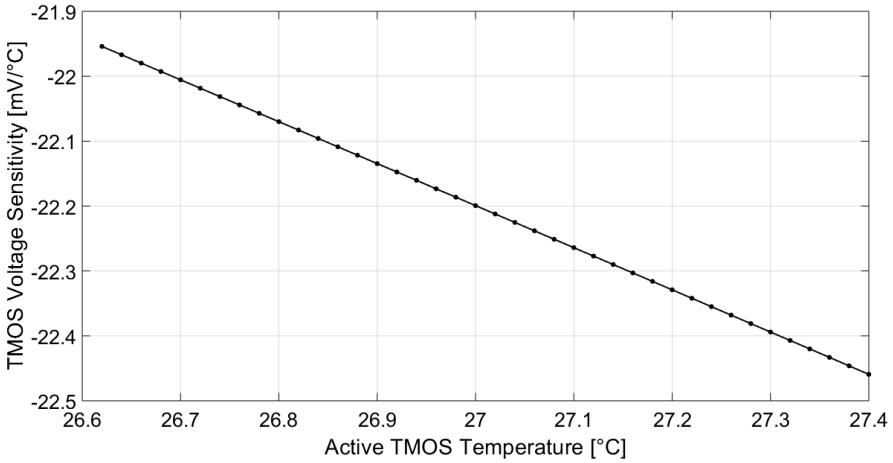

Figure 4.5: Simulated voltage sensitivity $S_{V,\,TMOS}$ for a 3T voltage readout configuration, in the case of a ±0.4 °C TMOS temperature variation around room temperature, which corresponds to a ±20 °C target object temperature variation.

configurations employed in other works is reported in Tab. 4.1. The proposed 3T configuration features by far the highest voltage sensitivity, even when compared to [48] which actually employs nine TMOS in series to enhance the sensitivity to nine times the one of a single TMOS element. Furthermore, the power dissipation is very low, thus making the proposed configuration ideal for integration in mobile and wearable devices.

4.2 TMOS bias circuit

As the bias circuit of Fig. 4.6 was identified as the optimal one, it was employed in the test chip design, as shown in Fig. 4.7. M_1 and M_2 transistors implement the current sink, mirroring 1:1 the current I_{TMOS}, which is provided externally and set equal to 2 μA, thus biasing each device at 1 μA. Resistors R, integrated on-chip, are equal to 600 kΩ, thus resulting in the desired 600-mV common-mode voltage.
In order to correct the mismatch between the two TMOS devices, a current digital-to-analog converter (DAC) was added to adjust one of the TMOS devices gate voltage, while keeping the other's gate voltage fixed: the switches controlled by the $ctrl_{DAC}$ signal allow choosing to adjust either the active of

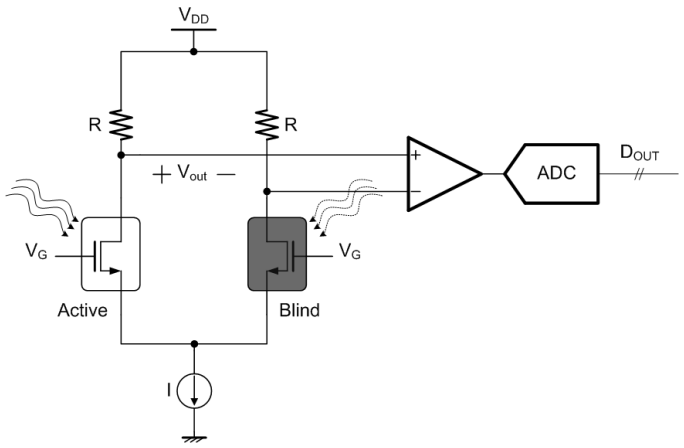

Figure 4.6: Optimal TMOS voltage-mode readout configuration.

the blind TMOS gate voltage, depending on the sign of the mismatch. The fixed gate voltage is set to V_{REF}, provided externally and set to 520 mV, while the adjusted gate voltage is equal to $V_G = V_{REF} + R_{DAC}I$, where I is the current provided by the DAC with the selected binary code.
The DAC features 9 bits, b_0-b_8, which are used to enable the switches and, therefore, the currents mirrored by transistors M_{b0}-M_{b8}. The reference current, I_{DAC}, is set equal to 256 nA and is provided externally. The transitors ratios are:

$$M_{b8} : M_0 = 1 : 1 \tag{4.4}$$

$$M_{b7} : M_0 = \frac{1}{2} : 1 \tag{4.5}$$

$$M_{b6} : M_0 = \frac{1}{4} : 1 \tag{4.6}$$

$$M_{b5} : M_0 = \frac{1}{8} : 1 \tag{4.7}$$

$$M_{b4} : M_0 = \frac{1}{16} : 1 \tag{4.8}$$

$$M_{b3} : M_0 = \frac{1}{32} : 1 \tag{4.9}$$

$$M_{b2} : M_0 = \frac{1}{64} : 1 \tag{4.10}$$

$$M_{b1} : M_0 = \frac{1}{128} : 1 \tag{4.11}$$

$$M_{b0} : M_0 = \frac{1}{256} : 1 \tag{4.12}$$

In order to correct the mismatch, the proper binary code is selected so that, with the gate voltage adjustment, the TMOS drain voltages, V_{outT1} and V_{outT2}, are equal when no signal is applied, i.e. when the active device does not see a target object.
Choosing R_{DAC} equal to 14 kΩ allows correcting for a ±190 nA current mismatch between the active and blind TMOS, in order to avoid saturating tha amplifier, with a current resolution, I_{res}, equal to 0.37 nA. Multiplying the current resolution by the output impedance, R, the voltage resolution is obtained:

$$V_{res} = I_{res}\ R = 0.370 \text{ nA } 600 \text{ k}\Omega = 0.222 \text{ mV} \tag{4.13}$$

The maximum residual drain voltage mismatch error, therefore, is $V_{res}/2$, which, considering the simulated sensitivity to the target object temperature obtained in Section 4.1 (i.e. -443.4 μV/°C), corresponds to 0.25 °C. The residual mismatch error, however, is not an issue as it can be solved by calibration provided in the digital domain after the analog-to-digital conversion.

4.3 TMOS characterization measurements

In this work, a TMOS consisting of a 660 μm × 660 μm large pixel area, made up by a 8 x 8 mosaic matrix of 60 μm × 60 μm sub-pixels connected in-parallel, is considered. Each pixel features a 77.4-μm width 15.8-μm length N-type transistor, fabricated in 130-nm CMOS-SOI and thermally isolated by a post-process dry etching on wafers.
The MOS are embedded on a dielectric membrane that is anchored to the bulk through two dielectric arms. The active and the blind sensors are packaged together under vacuum, employing a wafer bonding process thanks to the MEMS technology: the gas inside the cavity can be selected as well its pressure in a range from 100 μbar to 100 mbar. The achieved vacuum levels eliminate the thermal losses due to conduction, increasing the sensor efficiency.
To carry out the etching process, the sensor wafer is first bonded with the cap wafer and then attached from the back after appropriate masking and lithography at the active area of the device. Finally the MEMS structure is completed with a silicon cap on the back so that the active part remains encapsulated into vacuum. After the active part realization in CMOS technology, one of the two pixel matrices is protected from IR radiation by a metal rectangle de-

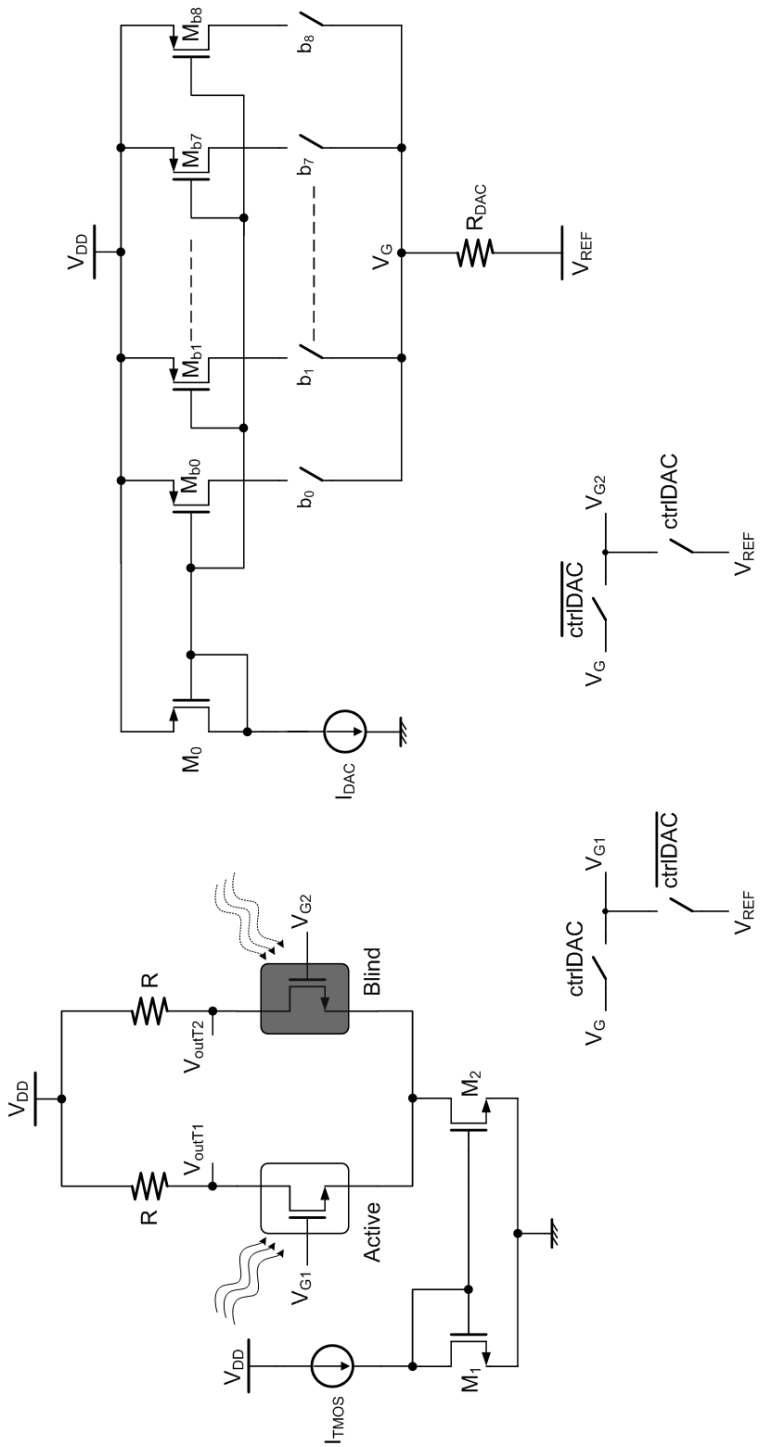

Figure 4.7: TMOS bias circuit with current DAC for mismatch correction.

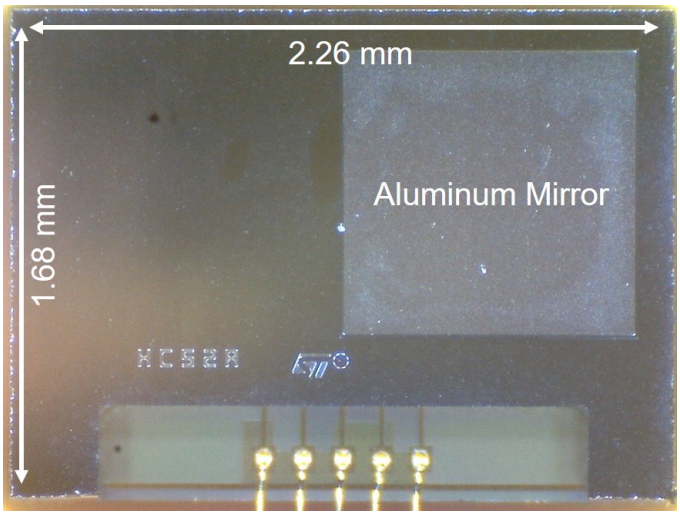

Figure 4.8: Packaged TMOS sensor micrograph.

posited on the front of the silicon cap, thus realizing the blind sensor. Smart Wafer Level Packaging (WLP), with vacuum, integrated optical window and, if required, filters and optics, can be performed at a standard CMOS fab at great cost reduction.
Fig. 4.8 shows the packaged sensor micrograph.
The TMOS performance can be modeled employing the equations reported in Subsection 1.4.2, considering G_{th} equal to 1.25 10^{-7} W/K, n equal to 1.4, V_T equal to 0.34 V, $\frac{dV_T}{dT}$ equal to -1 mV/K, and taking into account the transistor operating point determined by the bias circuit. The TMOS emissivity value equal to 0.3 was evaluated estimating the TMOS absorption efficiency, which is lowered by the optical losses introduced by the typical reflectance characteristics of the silicon cap. The derived TMOS responsivity value is, therefore, -1.85 kV/W.
The sensor FOV, without caps or additional optics, is 120°.
The expected sensor response time, calculated relying on the thermal parameters of the TMOS model, is 87 ms. The response time value was verified through measurements exposing the sensor to the radiation emitted by an IR LED source [50], as schematically shown in Fig. 4.9. The LED was controlled by V_S, in order to feature a square-wave shaped radiation profile in time. The rise and fall times of the LED source are less than 4 ms, therefore negligible with respect to the expected response time. The square wave frequency was varied from 100 mHz to 3 Hz and it was observed that the TMOS output

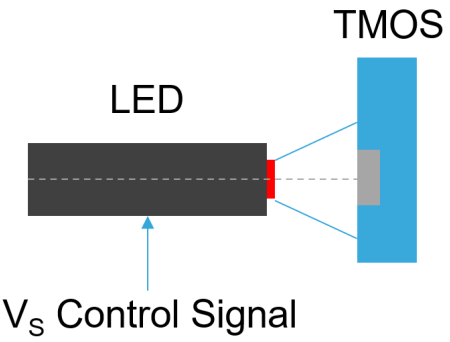

Figure 4.9: Schematic view of the setup for the response time measurements.

signal followed the input IR signal up to 1.8 Hz: the TMOS response time τ was, therefore, estimated as

$$\tau = \frac{1}{2\pi f} = \frac{1}{2\pi\ 1.8Hz} = 87\ \text{ms} \tag{4.14}$$

which is not far from the expected value derived from the thermal model parameters.
The TMOS sensor was tested with the proposed bias circuit, fabricated in a standard 130-nm CMOS process. The DAC bits were programmed with an Arduino Mega board through I^2C protocol thanks to the integrated digital interface on the test-chip. In order to correct the TMOS mismatch error, the DAC code was adjusted to get zero differential drain voltage while employing a mirror as target object: in this way the sensor was seeing only itself and, therefore, there was no temperature difference between the active and the blind device. The supply voltage provided by an Agilent E3631A power supply was equal to 1.2 V, the fixed gate voltage supplied by a Hewlett Packard 3245 universal source was equal to 520 mV and the bias currents were regulated through variable resistors on board. The differential TMOS drain voltage was acquired with a Keithley 2000 multimeter. Fig. 4.10 report the measured TMOS differential drain voltage for different DAC codes: it can be seen that for the considered sample the uncalibrated sensor (DAC code = 0) features an offset equal to -1.6 mV, that is reduced to 19 μV with DAC code = 8.
In order to verify the TMOS operation as thermal detector, the sensor was tested exposing it to the thermal radiation emitted by a target object. The same heater employed for the thermopile case was employed as target and

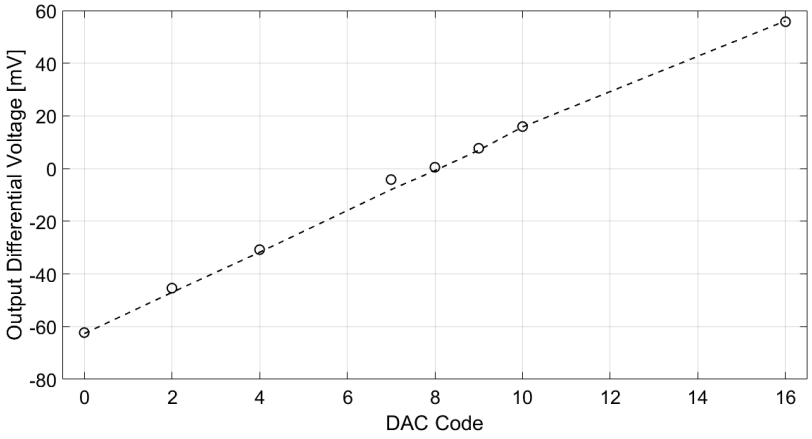

Figure 4.10: Measured TMOS differential voltage for different DAC codes.

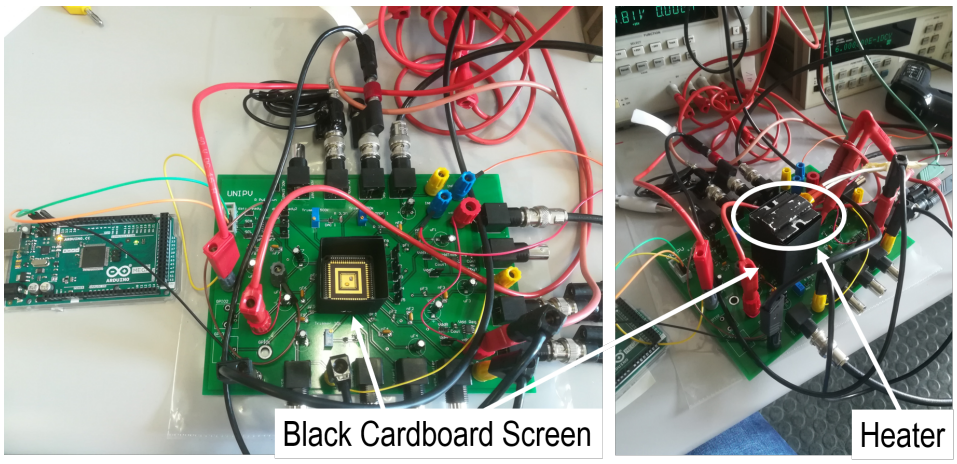

Figure 4.11: Employed measurement setup.

no additional cap or optics was placed on the sensor. The heater was positioned at a 3-cm distance from the chip, which was surrounded by a black cardboard screen in order to shield the sensor from unwanted radiation from other objects. The heater temperature and the cardboard screen temperature, considered as ambient temperature, were measured with a *surpeer* IR thermometer. Fig. 4.11 illustrates the described measurement setup.
The measured TMOS performance is illustrated in Fig. 4.12.
The sensor characteristic in the considered temperature range is highly linear,

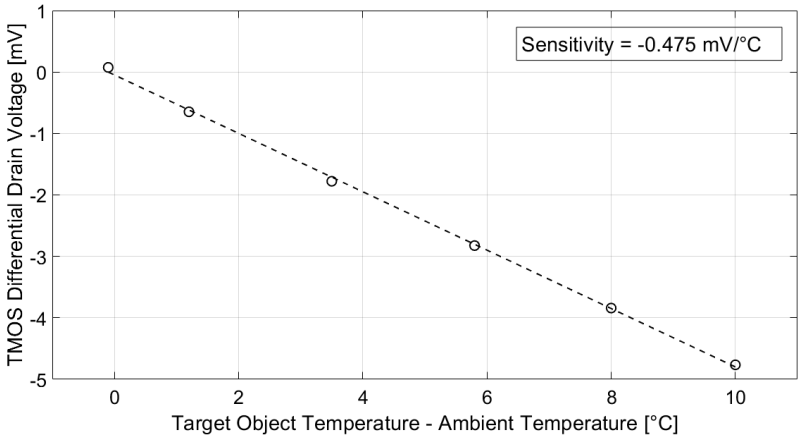

Figure 4.12: Measured TMOS differential drain voltage with the target at 3-cm distance and ambient temperature equal to 30 °C .

featuring a squared linear correlation coefficient, R^2, equal to 0.999267.
The measured sensitivity value, -0.475 mV, well matches the sensitivity value derived from simulations supposing $TF = 0.02$. Furthermore, the model illustrated in Section 1.4.2 well approximates the sensor performance as the regression index between the measured and the estimated results is equal to 0.983303. The regression index is calculated as

$$Regression\ Index = 1 - \frac{{\sigma_{err}}^2}{{\sigma_{var}}^2} \tag{4.15}$$

where ${\sigma_{err}}^2$ is the variance of the error between measured and estimated values and ${\sigma_{var}}^2$ is the variance of the observed variable.

Chapter 5

TMOS readout circuit

Having adopted for the TMOS the bias circuit described in Chapter 4, a voltage-based readout circuit was designed taking into account, as for the thermopile-based sensor case, the specifications set for contact-less human body temperature measurements, i.e. repeatability and accuracy within ± 0.3 °C. As the specifications for contact-less temperature detection are stricter, the system could also be employed for presence and motion detection.

5.1 Readout circuit description

The interface circuit must provide amplification while limiting the offset and noise at low frequency, in order not to mask the TMOS signal, which substantially behaves as a DC. For these reasons, as for the thermopile interface circuit, a chopper-based architecture was employed. The readout chain is illustrated in Fig. 5.1: it consists of a modulator, a fully differential instrumentation amplifier, a filter which performs also the demodulation operation, an analog-to-digital converter (ADC) and two buffers that can be enabled to measure directly the analog output.
The modulator, which moves the input signal from baseband to the chopping frequency, is implemented through four CMOS switches, controlled by complementary phases ϕ_1 and ϕ_2, provided by a standard disoverlap circuit. The chopping frequency is 1 kHz. Instead of employing an analogous structure for the demodulator, the demodulation operation is performed by the filter [51], which also allows setting the common mode voltage, $V_{CM,new}$, for the differential signal independently from the one set by the amplifier.
The filter operation is explained in detail considering the single-ended ver-

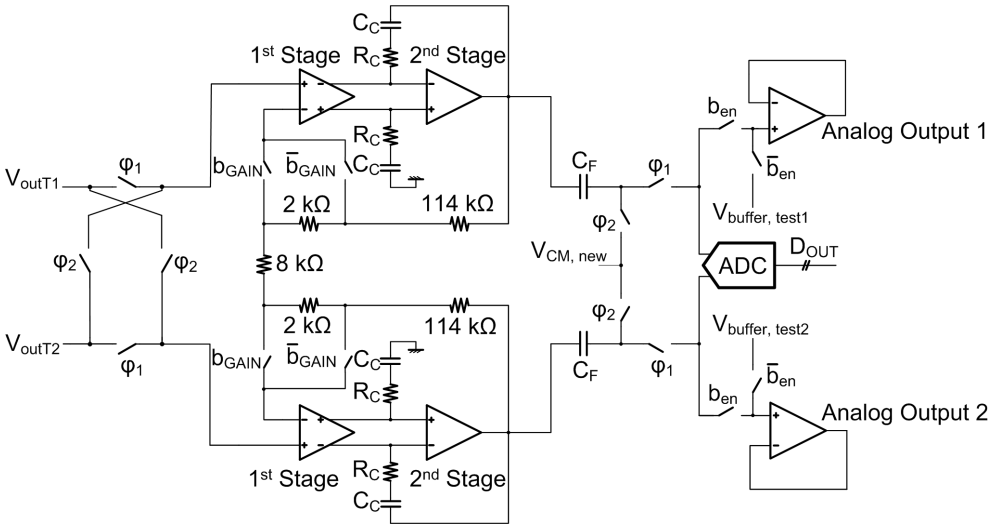

Figure 5.1: TMOS readout circuit chain.

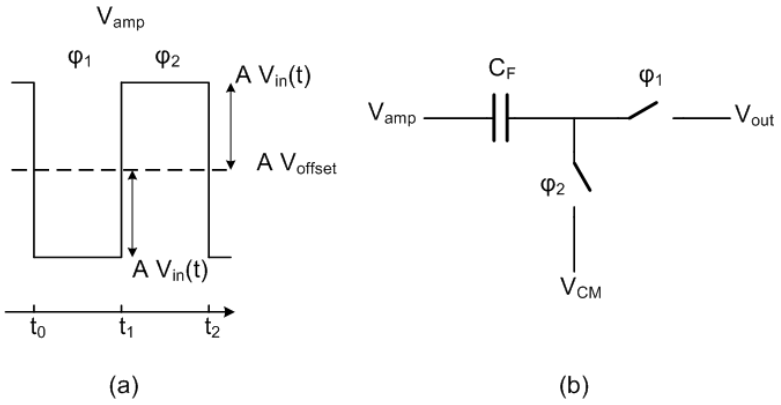

Figure 5.2: (a) Timing diagram of the filter input signal, (b) employed filter single-ended version.

sion reported in Fig. 5.2(b) and the timing diagram for V_{amp}, illustrated in Fig. 5.2(a), which corresponds to the output voltage of a single-ended amplifier preceded by a modulator, i.e. the single-ended version of the proposed interface circuit. V_{in} is the input signal of the modulator-amplifier cascade, which corresponds to the TMOS drain voltage in the considered application. As the input signal is transformed into a square-wave at the chopping frequency by the modulator, while the offset component is a DC term, the goal of the filter

is to reject the DC while revealing the peak-to-peak amplitude of the square wave. During phase ϕ_1 the amplified modulated signal is sampled on capacitor C_F:

$$V_{C_F} = V_{amp} - V_{CM} = -A\ V_{in}(t_1) + A\ V_{offset} - V_{CM} \tag{5.1}$$

where A is the amplifier gain, V_{offset} the amplifier input-referred offset and V_{CM} the desired common mode voltage.
During phase ϕ_2 capacitor C_F acts as a level shift, giving rise to an output voltage equal to

$$V_{out}(t_2) = V_{amp} - V_{C_F} \tag{5.2}$$

$$V_{out}(t_2) = A\ V_{in}(t_2) + A\ V_{offset} - [-A\ V_{in}(t_1) + A\ V_{offset} - V_{CM}] \tag{5.3}$$

$$V_{out}(t_2) = A\ V_{in}(t_2) + A\ V_{in}(t_1) + V_{CM} = 2\ A\ V_{in} + V_{CM} \tag{5.4}$$

as the input signal V_{in} is substantially constant. The filter, therefore, provides an additional gain of 2.
Taking into account also the 1/f amplifier noise term, V_f, the output voltage becomes

$$V_{out}(t_2) = A\ [V_{in}(t_1) + V_{in}(t_2) - V_f(t_1) + V_f(t_2)] + V_{CM} \tag{5.5}$$

which corresponds to a $A(1-z^{-1})$ high pass filter of $V_f(t)$ in the sampled data domain, as it is obtained by the autozero method.
By doubling the structure of Fig. 5.2, the fully differential version employed for the designed interface circuit, reported in Fig. 5.1, is obtained.
The fully differential instrumentation amplifier consists of two stages: the first stage amplifiers are implemented through a folded cascode structure, while the second stage amplifiers are constituted simply by a differential pair with active load. The achieved overall simulated DC gain equals to 100dB. Switches controlled by b_{GAIN} select the resistive feedback network, thus implementing a closed-loop gain of 20 or 30, resulting in an overall amplification factor of 40 or 60, considering also the gain provided by the filter. Resistors R_C and capacitors C_C ensure compensation.
The ADC is based on a conventional 12-bits fully differential successive approximation register (SAR) architecture with ±950-mV differential full scale. Switches controlled by b_{EN} are employed to enable the buffers in order to measure the analog output. While the TMOS biasing and the analog readout block were designed specifically for the TMOS sensor, the ADC was a standard SAR block designed by STMicroelectronics and already available.
A digital interface allows programming the DAC, setting the gain, enabling the buffers and reading the ADC output through the I^2C protocol.

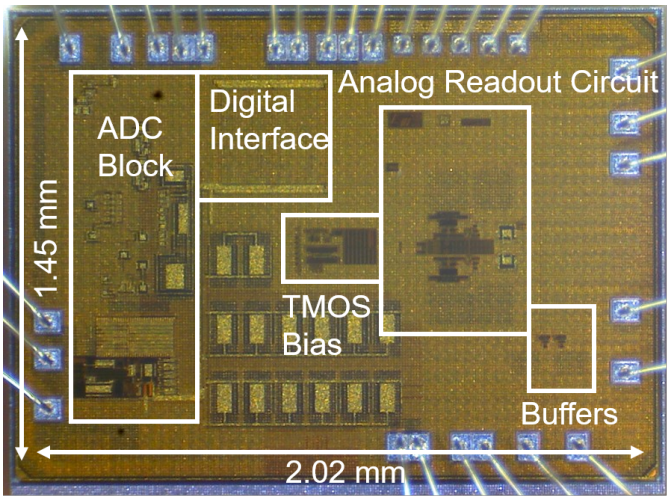

Figure 5.3: Interface circuit test-chip micrograph.

The readout circuit was implemented in a standard 130-nm CMOS process by STMicroelectronics and packaged together with the TMOS sensor chip in a ceramic package. A die photo of the readout circuit is reported in Fig. 5.3.

5.2 Readout circuit measurement results

The 1.45 $\times$ 2.02 mm^2 interface circuit test-chip prototype was characterized considering a batch of 10 samples. The measurement setup was as follows. Two Agilent E3631A power supplies provided the supply voltages, equal to 1.2 V for the analog readout circuit part, 1.8 V for the ADC block and the digital interface and 5 V for the on-board level-shifters employed to allow communications with the Arduino Mega employed to program the test-chip through the I^{2}C protocol. A Hewlett Packard 3245 universal source supplied the common-mode voltage, while the amplifier bias current, equal to 10 μV, was provided and regulated through a variable resistor on-board. Keithley 2000 multimeters in voltmeter mode were employed to measure the circuit analog outputs. The ADC references, clock and phases were generated on chip in the ADC block. The 1-kHz 0-1.2-V square wave chopper clock signal was provided by a Tektronix AFG3252 function generator.
To verify the effectiveness of the chopper-based structure the residual offset was measured: no signal was applied at the amplifier input, setting both inputs and the filter common-mode voltage equal to 600 mV through the universal

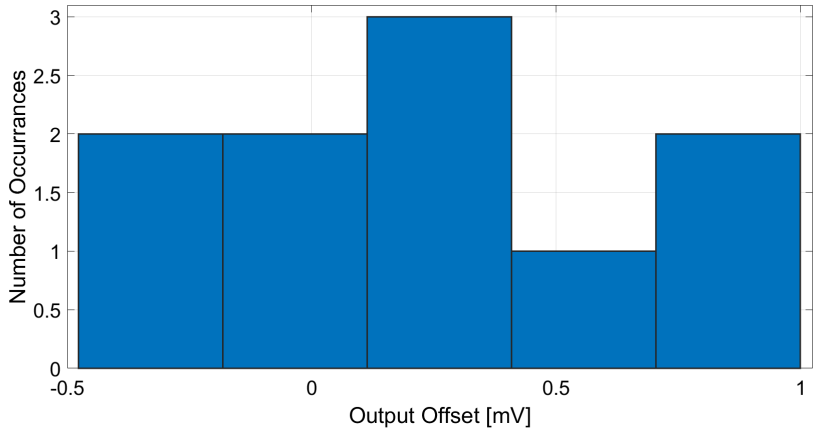

Figure 5.4: Measured offset at the analog interface circuit output.

Table 5.1: DC linearity and gain characterization for randomly selected samples

Sample Number	**Linear Correlation Coefficient** R	**Derived Gain**
2	0.999979	39.89
5	0.999995	39.58
8	0.999988	39.59

source. The test-chip was programmed through the Arduino board setting the overall gain equal to 40, enabling the analog output buffers and disabling the ADC, in order to test only the analog part of the interface circuit. The analog outputs were measured through the multimeters and the differential output was derived. The output buffers were characterized, setting b_{EN} low, and their offset voltages were subtracted from the derived differential output. The obtained residual offset values are reported in the histogram of Fig. 5.4. The input-referred offset standard deviation, equal to 9.171 μV, is significantly lower than the TMOS sensitivity measured in Section 4.3 (i.e. -475 μV) and thus the error due to the residual offset is negligible.
The gain and DC linearity of the analog readout were verified fully characterizing three randomly samples: a differential DC signal, ranging from -12.5 to 12.5 mV was applied to the interface circuit input with the universal source and the analog output voltages were measured through the multimeter, always taking into account the buffer offsets and subtracting them. The selected gain was 40. The results are reported in Tab. 5.1. The linear correlation coef-

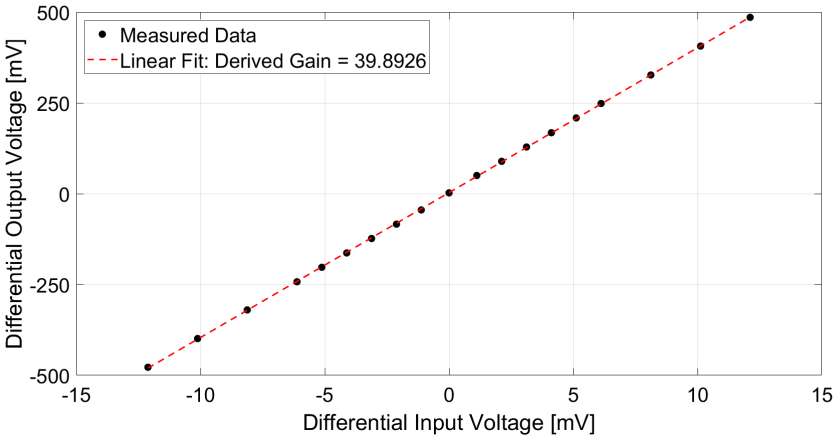

Figure 5.5: Measured input-output characteristic of the analog part of the proposed interface circuit with gain equal to 40.

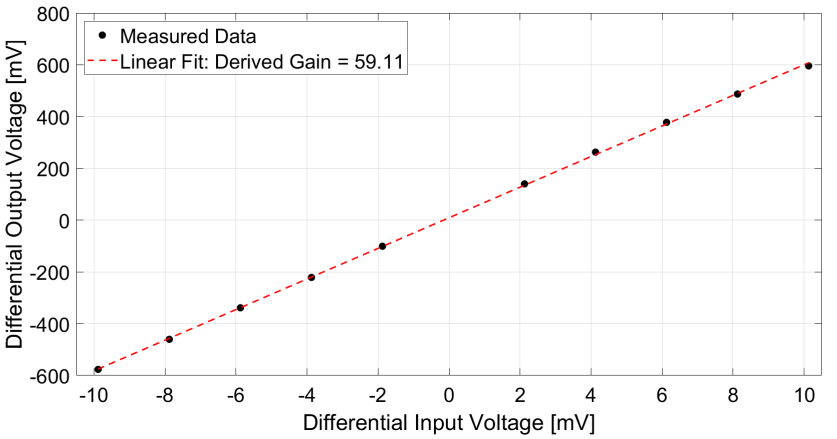

Figure 5.6: Measured input-output characteristic of the analog part of the proposed interface circuit with gain equal to 60.

ficient substantially equal to 1 shows almost ideal linearity, as required by the application were the signal is practically at DC. The measured input-output characteristic, with the gain set to 40, of sample # 2 is illustrated in Fig. 5.5, while the input-output characteristic, with the gain set to 60, is illustrated in Fig. 5.6.

The ADC functionality was verified characterizing it as a stand-alone block

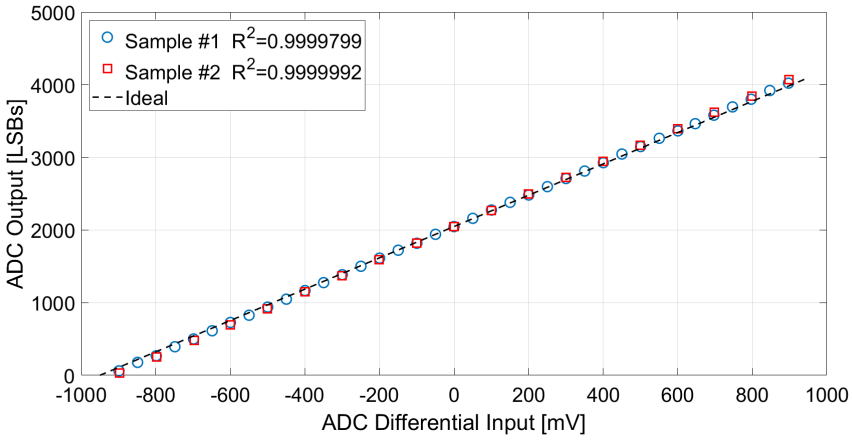

Figure 5.7: Measured input-output ADC characteristic (sample # 1 and sample # 2).

exploiting the supported test-mode: in that case the ADC differential input is supplied externally through two pads, as the filter output is not connected to the ADC input.
The ADC differential input was supplied applying a DC differential signal with the universal source, covering the ADC full scale, with the common-mode voltage set to 950 mV. The resulting ADC conversion was read employing Arduino after having been written in specific registers in the chip digital interface.
The measured input-output characteristics for two ADC samples are reported in Fig. 5.7, along with ideal ADC characteristic: the measured characteristics well match the ideal one as the squared linear correlation coefficient, R^2, is practically equal to 1.

5.3 Sensor-readout circuit system measurement results

The proposed TMOS sensor and its bias and interface circuit, integrated into two separate chips and bonded on the same ceramic package, as shown in Fig. 5.8, were tested together as a system to perform both human body temperature measurements and motion and presence detection.

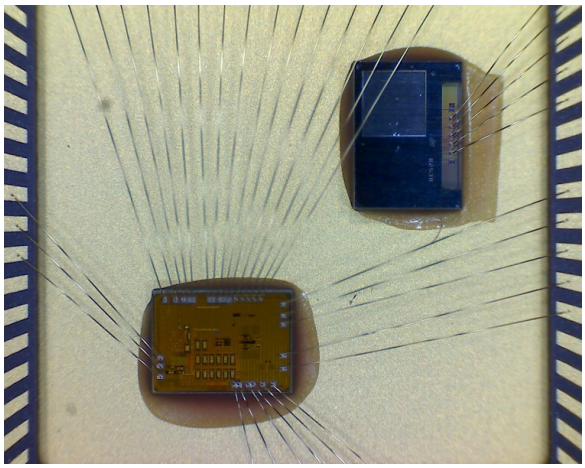

Figure 5.8: Photograph of the packaged test-chip.

5.3.1 Fever measurement application

The measurement setup is illustrated schematically in Fig. 5.9: the test-chip was programmed employing an Arduino Mega; the 1-kHz 0-1.2-V clock square wave was supplied by a Tektronix AFG3252 function generator; Agilent E3631A power supplies provided the supply voltages for the TMOS biasing (1.2 V), the analog interface readout (1.2 V) and the ADC and digital block (1.8 V); a Hewlett Packard 3245 Universal Source supplied the common-mode voltage (600 mV) and the V_{REF} voltage (520 mV) for the TMOS gate biasing; Keithley multimeters were employed to acquire the analog outputs; the TMOS drain terminals were connected to the interface circuit inputs and the bias currents, both for the TMOS bias circuit and for the amplifier, were regulated through on-board resistors.
The same 4 cm $\times$ 3.5 cm heater described in Chapter 3 and Chapter 4, with 0.95 emissivity and an equivalent radius of 2.11 cm, was employed as target object. As for the TMOS characterization measurements featured in Chapter 4, a black cardboard was used to screen sensor from unwanted thermal radiation in the surroundings. A *surpeer* IR thermometer was employed to measure the cardboard screen and, therefore, ambient temperature.
The TMOS sensor was calibrated programming the DAC bits though the Arduino board, in order to correct the mismatch error as illustrated in Chapter 4. The gain was set equal to 40, unless stated otherwise.
At first the measurements were focused only on the readout analog outputs, as the TMOS biasing and the interface analog block were the ones specifi-

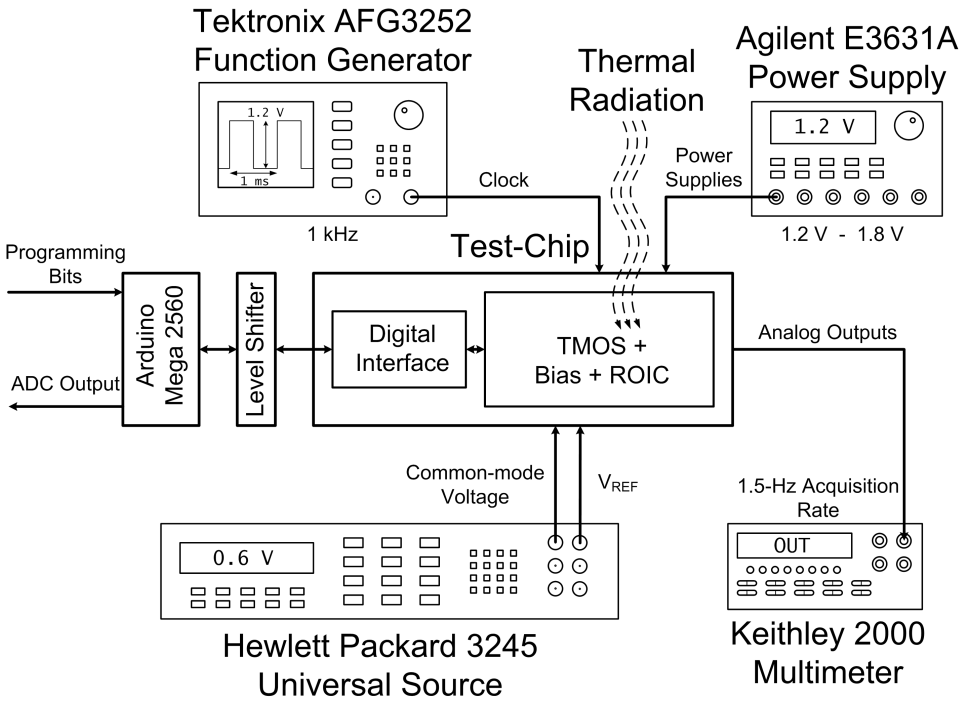

Figure 5.9: Measurement setup.

cally designed for the sensor. The analog buffers were characterized and their offset voltages subtracted from the output voltage measurements. Each measurement was performed acquiring 50 samples with the multimeter at 1.25-Hz rate: the samples were stored in the multimeter buffer, which then returned the average value, that is the value considered for each measurements.
The ambient temperature was approximately equal to 25 °C.
In order to verify that the TMOS sensor output differential voltage is correctly amplified by the analog interface, the measured voltage at the sensor-interface circuit analog output was compared with the measured TMOS output multiplied by the readout circuit gain. The measurements were performed with the heater placed at 3-cm distance from the sensor. No additional caps or optics were placed on the TMOS, resulting in a 120° FOV. As illustrated in Fig. 5.10, the results almost perfectly match.
Measurements considering different distances between sensor and target object were performed to further investigate the sensor sensitivity: the results are reported in Fig. 5.11. As expected, as the heater does not completely fill the detector FOV (i.e. 120°), the sensitivity depends on the distance.

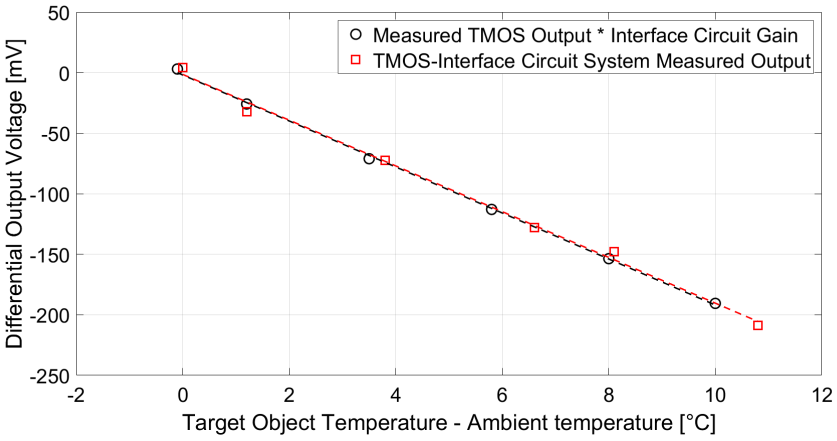

Figure 5.10: Comparison between the TMOS sensor-interface circuit system measured analog output and the measured TMOS output multiplied by the interface circuit gain. The measurements are performed with the target object at 3-cm distance.

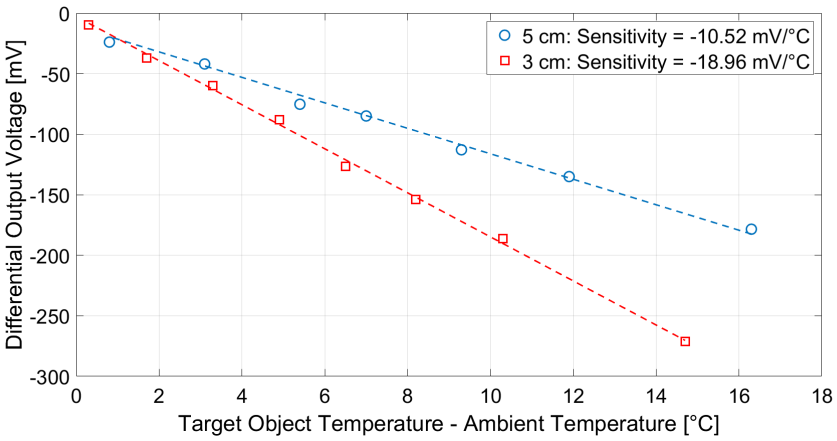

Figure 5.11: Measured TMOS sensor-interface circuit system analog output with the target object at different distances. The FOV is 120°.

In order to verify that, as expected relying on the model illustrated in Subsection 1.4.1 and on the expression (2.4) which holds through independently from the type of thermal detector, the sensitivity does not vary with distance, provided that the target object completely fills the sensor FOV, a perforated

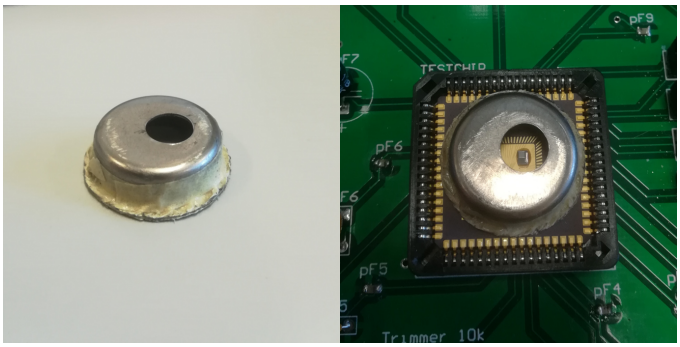

Figure 5.12: Perforated metal cap determining a FOV equal to 50.33°.

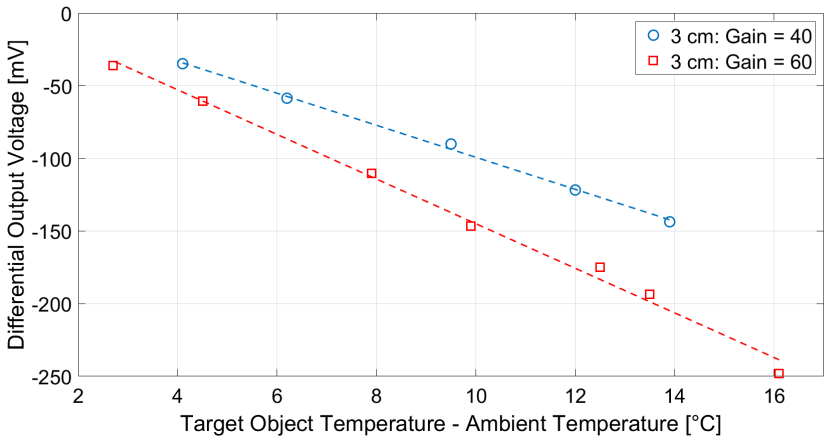

Figure 5.13: Measured TMOS sensor-interface circuit system analog output with the target object at 3-cm distance for different gain values. The FOV is 50.33°.

metal cap was applied in order to limit the FOV. The employed cap, whose inner surface was covered in black paint to avoid reflections, is shown in Fig. 5.12. Relying on trigonometry, as illustrated in Fig. 2.3, the FOV determined by the perforated metal cap was calculated and results equal to 50.33°.
Fig. 5.13 illustrates the TMOS sensor-interface circuit system analog output with the target object at 3-cm distance for different gain values, while employing the perforated metal cap. Almost ideal linearity is achieved: the squared linear correlation coefficient, R^2, in fact, is equal to 0.997814 and 0.993703 for 40 and 60 gain, respectively.
Having selected a gain equal to 40, the measurements results considering the

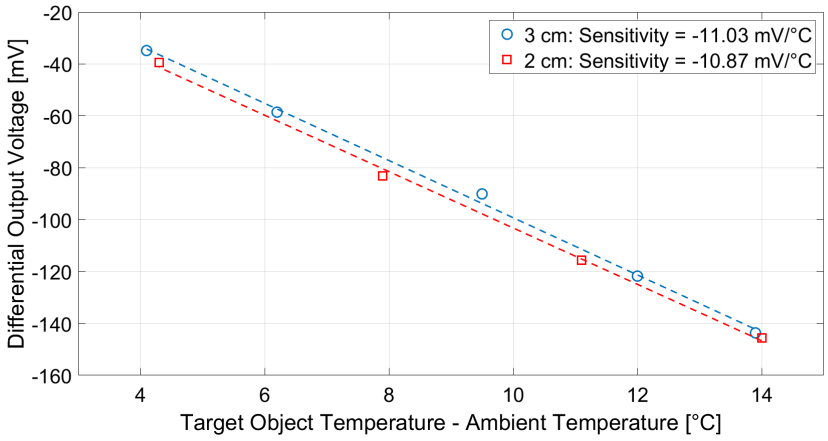

Figure 5.14: Measured TMOS sensor-interface circuit system analog output with the target object at different distances. The FOV is 50.33°.

sensor with the metal cap limiting its FOV and different heater-detector distances are reported in Fig. 5.14. As expected there is no dependence on the distance, as in this case the target fills completely the detector FOV, thus making the system suited for contact-less body temperature detection when the target-sensor distance is within a few centimeter range, as usually happens for the typical case of forehead fever measurements.
Repeatability, required for human body temperature measurements, was verified by performing several measurements under the same conditions: the results for the case of 3-cm distance and 50.33° FOV are illustrated in Fig. 5.15: very good repeatability can be inferred.
For deriving the sensitivity values, a linear approximation was considered: this is verified to be legitimate as the squared liner correlation coefficient, R^2, practically equal to 1, proves almost ideal linearity in the considered temperature range.
In order to determine the system accuracy, the noise was measured with the active sensor not exposed to IR radiation by acquiring with the multimeter 100 samples at 1.25-Hz rate at the analog output and measuring the standard deviation, equal to 608 μV. Considering 3σ, i.e. 1.824 mV, and the typical -10.95-mV/°C sensitivity, it corresponds to a 0.17 °C accuracy at fixed distance from the target, which is within the specification for medical devices.
The complete system functionality, including the ADC, was verified considering the case of the target object at 3-cm distance and 50.33° FOV: the digital sensor-interface circuit output is reported in Fig. 5.16.

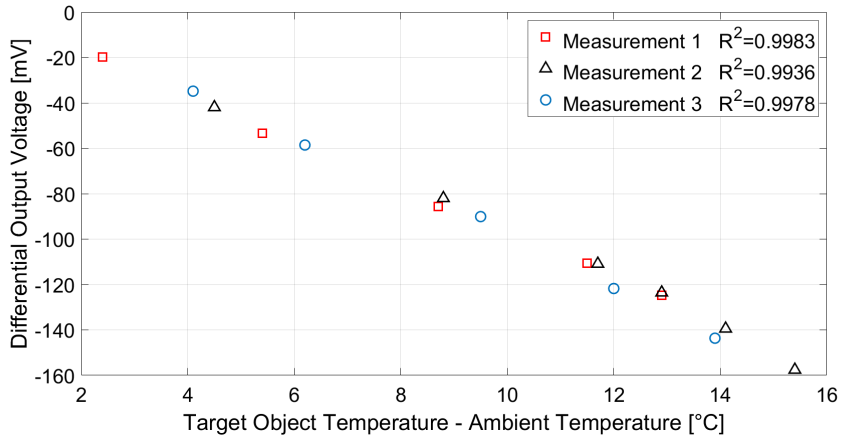

Figure 5.15: Repeated measurements of the TMOS sensor-interface circuit system analog output with the target object at 3-cm distance. The FOV is 50.33°. R^2 is the squared linear correlation coefficient.

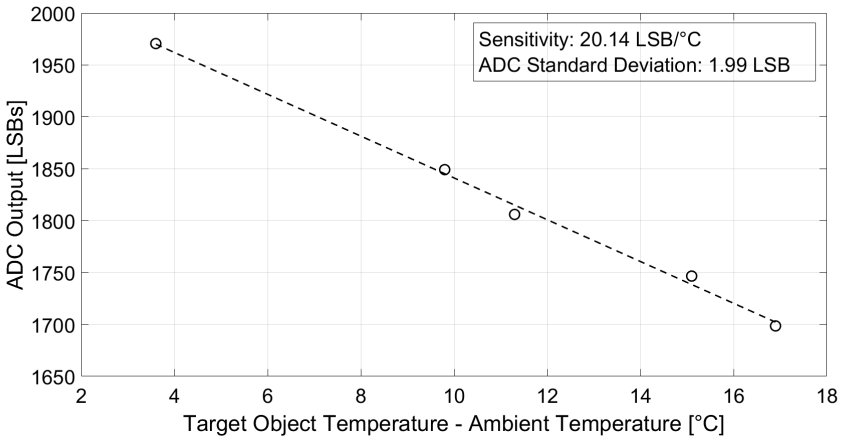

Figure 5.16: Measured TMOS sensor-interface circuit system digital output with the target object at 3-cm distance. The FOV is 50.33°.

Employing the multimeter in ammeter mode the supply currents for the TMOS biasing, the analog readout, the ADC and the digital block were measured: the TMOS biasing and the analog readout (1.2 V supply voltage) feature 183.6 μW power consumption, while the ADC and digital block (1.8 V supply voltage) feature 380.5 μW power consumption. As the ADC block was not designed tai-

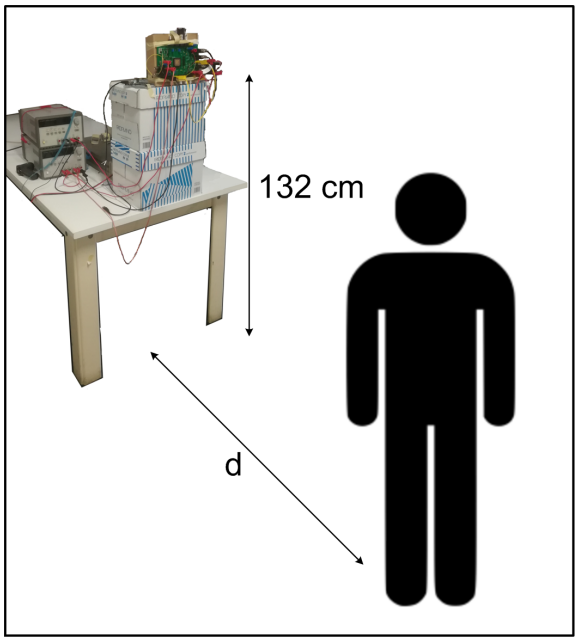

Figure 5.17: Schematic view of the employed measurement setup.

lored on the considered sensor and application, the power consumption could be reduced by optimizing the ADC.

5.3.2 Presence and motion detection application

The system suitability for presence detection of stationary subjects was tested considering a person standing at various distances in front of the sensor, on the normal line to the sensor surface. The system package, inserted in its dedicated board, was placed at a 132-cm height from the ground. The setup is schematically illustrated in Fig. 5.17.
The system supply and reference voltages and the chopper clock were provided as for the human body temperature measurement application, as illustrated in Subsection 5.3.1. The sensor offset was minimized calibrating the DAC bits and the differential analog output was acquired through a Keithley 2000 multimeter, always taking into account the buffers offset.
The measurements were performed at 25 °C room temperature, considering a 1.80-m average-build man as the stationary subject. For each selected distance, 50 output acquisitions at 1.25 Hz were performed considering both the case with the person standing and the empty room case. The difference between

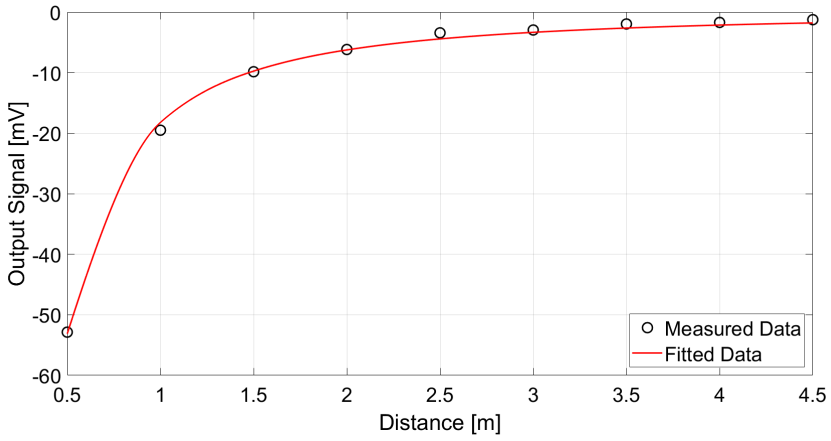

Figure 5.18: Measurement results for different subject distances.

the average in the occupied room case and in the empty room case was considered as the output signal of interest. The measurement results are reported in Fig. 5.18.
As the correlation coefficient, R^2, between the absolute value of the measured data for the TMOS-based system and the measured data for the thermopile-based system, is 0.97008, the fit function employed for the thermopile case proves to be a good approximation also for the TMOS-based system. The fit function derived employing the Matlab Curve Fitting Tool, therefore, is

$$Output\ Signal = \frac{c_{d1}}{d^{c_{d2}}} \tag{5.6}$$

where c_{d1} and c_{d2} are equal to -18.22 and 1.544, respectively, considering 95% confidence bounds, and d is the sensor-subject distance. The negative c_{d1} coefficient is due to the fact that the sensor sensitivity is negative. The R-squared coefficient and the RMSE are equal to 0.9983 and 0.7395, respectively. The derived fit curve is illustrated along with the measured data in Fig. 5.18. Considering a $\pm 2\sigma$ variation across the 50 acquired samples for each distance, a negative output signal, confirming the subject's detection, is found up to 4.5 m.
The system suitability for detection of moving subjects was also tested. The same room setup adopted for the detection of stationary subjects was employed and a 1.7-m average-build woman was considered as moving subject. The subject moved along a straight line, perpendicular to the sensor's normal, at different distances from the sensor. The measurements were performed at

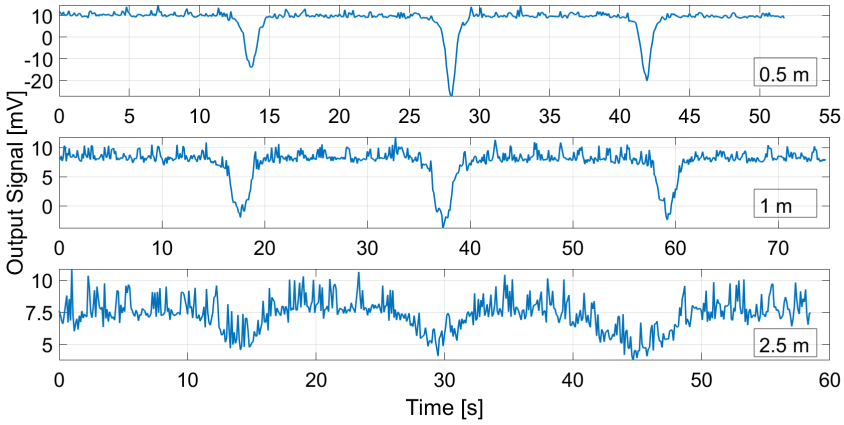

Figure 5.19: Measurement results in the case of a subject walking in front of the sensor at different distances.

27.7 °C acquiring the system output voltage through a Keithley 2000 multimeter coupled with a LabView program. The chosen acquisition rate was 10 Hz. Fig. 5.19 and Fig. 5.20 illustrate the measurement results when the subject is walking and running, respectively. A negative peak when the subject moves within the sensor FOV is clearly visible. As for the thermopile-based system case, the peak lasts longer when the subject is walking as in that case the subject, being slower, remains longer within the sensor FOV.
The system suitability as proximity detector, for example for operating consumer appliances (hand dryers, sanitizing gel and soap dispensers, toilet flush, water taps) without touching them, was also verified by moving one hand in front of the sensor at different distances. The measurement results are illustrated in Fig. 5.21.

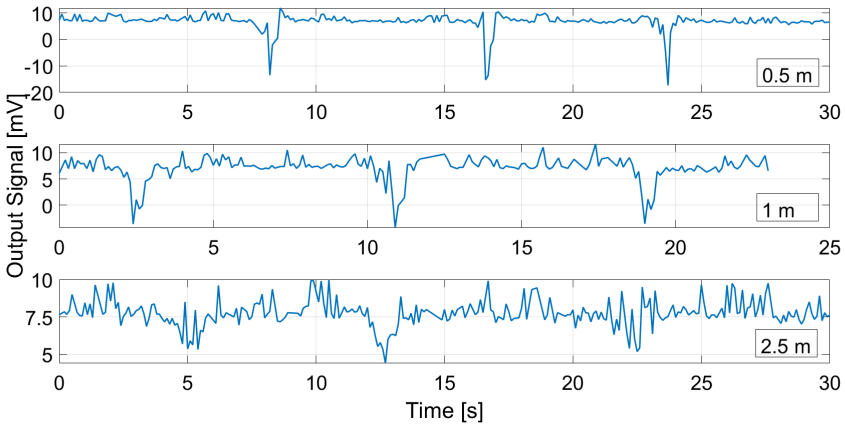

Figure 5.20: Measurement results in the case of a subject running in front of the sensor at different distances.

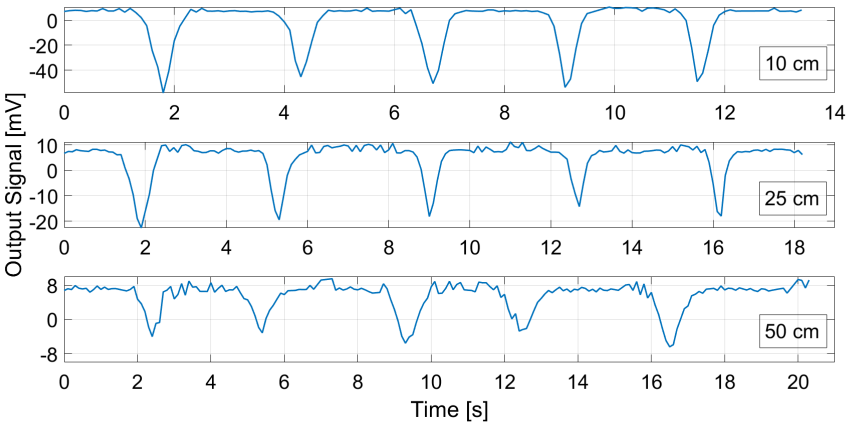

Figure 5.21: Measurement results in the case of a hand placed in front of the sensor at different distances.

Conclusions

In this work, two different kinds of thermal detectors and their interface circuits, specifically tailored on the sensor characteristics, have been presented. Both sensor solutions, differently than PIR and bolometers presents nowadays on the market, allow integration, being compatible with CMOS processes, and large-scale low-cost production, thus satisfying the requirements for thermal detectors targeting smart homes, IoT, mobile and wearable devices applications, which have considerably grown in recent years. In particular, due to the COVID-19 pandemic, the demand for contact-less fever detection devices has increased. The market for thermal detector systems, however, is not limited to contact-less absolute temperature applications, but comprises presence, proximity and motion detection systems, employed in a wide range of fields (security, climate control, monitoring of manufacturing processes, appliances and consumer products).
The proposed thermal sensor-interface circuit systems have been characterized both for contact-less human body temperature measurements and for presence and motion detection. Tab. 5.2 summarizes and compares the characteristics of the proposed systems. Both interface circuit systems were fabricated employing a standard 130-nm CMOS process by STMicoelectronics; the thermopile-based interface circuit features a smaller area, however that is reasonable as the TMOS interface includes also the sensor biasing circuit, which is not required for the thermopile as it is self-biased.
The overall power consumption for the TMOS system is higher than the thermopile-based one, however the power consumption due to the TMOS biasing and analog block alone is significantly lower then the thermopile-based system, which comprises only the amplifier, the passive filter and the output buffer. Since the ADC and digital block were not tailored for this application, their design could be optimized in order to minimize the power consumption. The employed chopping frequencies are comparable, as are the sensors FOV, limited by the perforated metal caps.
Although the sensor active area is smaller then the one of the thermopile,

the TMOS sensor, exploiting the advantages in terms of internal gain given by being an active device, features a responsivity value orders of magnitude larger then the thermopile. Also the input-referred sensitivity (i.e. the sensitivity at the output divided by the readout gain) is better in the TMOS case, considering the same target-detector distance and similar FOVs.
Always considering 3-cm distance and FOV $\approx 50°$, the TMOS system features better accuracy. Both systems however satisfy the ± 0.3 °C accuracy specifications required for human body temperature measurements.
Both systems are suitable for presence detection of both stationary and moving subjects in a few meters range. The measured maximum distance for the TMOS-based system is smaller than the one for the thermopile-based system, however as the ambient temperature was higher, considering that the subject body temperature was roughly the same, it is reasonable that the temperature difference between subject and reference (i.e. ambient) was smaller, thus determining a smaller output signal. Furthermore no cap or screen was applied to the TMOS, therefore its FOV was unlimited and the subject occupied a smaller portion of it, with respect to having a limited FOV by a cap, as for the themopile case.
Both systems suitability for detection of moving subjects was also verified.
Although the TMOS response time is significantly larger than the one of the thermopile, that does not represent a problem as temperature varies very slowly and in the case of motion detection a response time lower that 100 ms is sufficient.
Both proposed systems represent excellent alternatives for low-cost, small and portable IR detector solutions and their versatility, both as absolute temperature measurements sensor and motion/presence detectors, allows their employment for a wide range of application. The TMOS-based system performance in particular, exploiting its advantage in terms of internal gain being an active device, looks promising for realizing a new generation of thermal detectors.

Table 5.2: Comparison between the proposed thermopile-based and TMOS-based systems

Parameter	**Thermopile-based system**	**TMOS-based system**
Technology	130-nm CMOS	130-nm CMOS/ 130-nm CMOS SOI
Area [mm^2]	0.605	2.08 (1.07 TMOS bias and analog readout)
Supply voltage [V]	1.2	1.2 (analog), 1.8 V (ADC and digital block)
Power consumption [μW]	292.8	183.6 (analog), 380.5 (ADC and digital block)
Chopping frequency [kHz]	2	1
Readout gain	100	40
Sensor active area [mm^2]	0.8 × 0.8	0.66 × 0.66
|Sensor responsivity| [V/W]	180	185000
Target-detector distance [cm]	3	3
Sensor FOV [°]	51.64	50.33
Sensitivity [μV/°C (input-referred)]	0.09	−0.274
Accuracy [°C] (3σ)	0.17	0.24
Sensor response time [ms]	13	87
Maximum distance for presence detection [m]	5.5 @ 22 °C	4.5 @ 25 °C

Bibliography

[1] J. R. Mahan, *Radiation Heat Transfer: A Statistical Approach, Volume 1.* John Wiley & Sons Inc., 2002.

[2] Y. Houdas and E. F. J. Ring, *Human Body Temperature: Its Measurement and Regulation.* Springer, 1982, pp. 24–27.

[3] W. L. Wolfe and P. W. Kruse, "Chapter 19: Thermal Detectors," in *Handbook of Optics*, McGraw-Hill, Ed., 1995.

[4] M. Almasri, D. P. Butler, and Z. Celik-Butler, "Self-supporting uncooled infrared microbolometers with low-thermal mass," *Journal of Microelectromechanical Systems*, vol. 10, no. 3, pp. 469–476, check 2001.

[5] P. Neuzil and T. Mei, "A Method of Suppressing Self-Heating Signal of Bolometers," *IEEE Sensors Journal*, vol. 4, no. 2, pp. 207–210, Apr. 2004.

[6] P. Liu, S. K. Nguang, and A. Partridge, "Occupancy inference using pyroelectric infrared sensors through hidden Markov models," *IEEE Sensors Journal*, vol. 16, no. 4, pp. 1062–1068, 2016.

[7] H. H. Kim, K. N. Ha, S. Lee, and K. Lee, "Resident location recognition algorithm using a Bayesian classifier in the PIR sensor-based indoor location-aware system," *IEEE Trans. Syst., Man, Cybern. C, Appl. Rev*, vol. 39, no. 2, pp. 240–245, 2009.

[8] Q. Hao, F. Hu, and Y. Xiao, "Multiple human tracking and identification with wireless distributed pyroelectric sensor systems," *IEEE Syst. J.*, vol. 3, no. 4, pp. 428–439, 2010.

[9] P. Zappi, E. Farella, and L. Benini, "Tracking motion direction and distance with pyroelectric IR sensors," *IEEE Sensors Journal*, vol. 10, no. 9, pp. 1486–1494, 2010.

[10] Q. Sun, J. Shen, H. Qiao, X. Huang, C. C., and F. Hu, "Static Human Detection and Scenario Recognition Via Wearable Thermal Sensing System," *Computers*, vol. 6, no. 3, 2017.

[11] L. Wu and Y. Wang, "A Low-Power Electric-Mechanical Driving Approach for True Occupancy Detection Using a Shuttered Passive Infrared Sensor," *IEEE Sensors Journal*, vol. 19, no. 1, pp. 47–57, 2019.

[12] H. Liu, Y. Wang, K. Wang, and H. Lin, "Turning a pyroelectric infrared motion sensor into a high-accuracy presence detector by using a narrow semi-transparent chopper," *Appl. Phys. Lett.*, vol. 111, no. 24, 2017.

[13] L. Wu, Y. Wang, and H. Liu, "Occupancy detection and localization by monitoring nonlinear energy flow of a shuttered passive infrared sensor," *IEEE Sensors Journal*, vol. 18, no. 21, pp. 8656–8666, 2018.

[14] A. Rogalski, *Infrared Detectors, Second Edition: Chapter 5.* CRC Press, Taylor & Francis Group, 2006.

[15] D. M. Rowe, *Thermoelectrics Handbook: Macro to Nano.* Taylor & Francis Group, 2006.

[16] H. J. Goldsmith, *Introduction to Thermoelectricity, Second Edition.* Springer, 2016.

[17] A. Rogalski, *Infrared Detectors, Second Edition.* CRC Press, Taylor & Francis Group, 2011.

[18] Z. Olgun, O. Akar, H. Kulah, and T. Akin, "An Integrated Thermopile Structure With High Responsivity Using Any Syandard CMOS Pocess," in *Proceedings of 1997 International Conference on Solid-State Sensors and Actuators (TRANSDUCERS)*, June 1997.

[19] A. Schaufelbühl, N. Schneeberger, U. Münch, M. Waelti, O. Paul, O. Brand, H. Baltes, C. Menolfi, Q. Huang, E. Doering, and M. Loepfe, "Uncooled Low-Cost Thermal Imager Based on Micromachined CMOS Integrated Sensor Array," *Journal of Microelectromechanical Systems*, vol. 10, no. 4, pp. 503–510, Dec. 2001.

[20] H. Zhou, P. Kropelnicki, and C. Lee, "CMOS Compatible Midinfrared Wavelength-Selective Thermopile for High Temperature Applications," *Journal of Microelectromechanical Systems*, vol. 24, no. 1, pp. 144–154, Feb. 2015.

[21] P. G. Datskos and N. V. Lavrik, *Encyclopedia of Optical Engineering, volume 1.* Marcel Dekker Inc., 2003.

[22] "A Simple DC Radiometer, Application Brief by *Dexter Research Center*," Online https://www.dexterresearch.com/?module=Page&sID=technical-library.

[23] E. Moisello, M. Vaiana, M. E. Castagna, G. Bruno, P. Malcovati, and E. Bonizzoni, "An Integrated Micromachined Thermopile Sensor with a Chopper Interface Circuit for Contact-less Temperature Measurements," *IEEE Transactions on Circuits and Systems I: Regular Papers*, vol. 66, no. 9, pp. 3402–3413, Sep. 2019.

[24] L. Gitelman, S. Stolyarova, S. Bar-Lev, Z. Gutman, Y. Ochana, and Y. Nemirovsky, "CMOS-SOI MEMS Transistor for Uncooled IR Imaging," *IEEE Transactions on Electron Devices*, vol. 56, no. 9, pp. 1935–1942, Sep. 2009.

[25] A. Zviagintsev, S. Bar-Lev, I. Brouk, I. Bloom, and Y. Nemirovsky, "Modeling the Performance of Mosaic Uncooled Passive IR Sensors in CMOS–SOI Technology," *IEEE Transactions on Electron Devices*, vol. 65, no. 10, pp. 4571–4576, Sept. 2018.

[26] E. Socher, B. S. M., and Y. Nemirovsky, "Temperature Sensitivity of SOI-CMOS Transistors for Use in Uncooled Thermal sensing," *IEEE Transactions on Electron Devices*, vol. 52, no. 12, pp. 2784–2790, Dec. 2005.

[27] A. Zviagintsev, I. Brouk, I. Bloom, and Y. Nemirovsky, "Self-Heating Effects in CMOS-SOI-NEMS Transistors for Uncooled Passive IR Sensors," in *Proceedings of 2015 IEEE International Conference on Microwaves, Communications, Antennas and Electronic Systems (COMCAS)*, Nov. 2015.

[28] A. Zviagintsev, I. Bloom, I. Brouk, and Y. Nemirovsky, "Modeling the Performance of Nano Machined CMOS Transistors for Uncooled IR Sensing," *IEEE Transactions on Electron Devices*, vol. 64, no. 11, pp. 4657–4663, Nov. 2017.

[29] E. Moisello, M. Vaiana, M. E. Castagna, G. Bruno, P. Malcovati, and E. Bonizzoni, "An Integrated Thermopile-Based Sensor with a Chopper-Stabilized Interface Circuit for Presence Detection," *Sensors*, vol. 19, no. 18, p. 3999, Sep. 2019.

[30] D. Xu, B. Xiong, Y. Wang, and Y. Li, "Robust Array-Composite Micromachined Thermopile IR Detector by CMOS Technology," *IEEE Electron Device Letters*, vol. 32, no. 12, pp. 1761–1763, Dec. 2011.

[31] H. Zhou, P. Kropelnicki, J. M. Tsai, and C. Lee, "CMOS-based thermopile using vertically integrated double polycristalline silicon layers," in *Proceedings of IEEE 26th International Conference on Micro Electro Mechanical Systems (MEMS)*, Jan. 2013.

[32] "Datasheet of TS118-3 Thermopile Sensor by *Measurement Specialties*," Online http://lusosat.org/hardware/200612916515751780.pdf.

[33] "Datasheet of s25 to-18 thermopile sensor by *Dexter Research Center*," Online https://www.dexterresearch.com/?module=Page&sID=s25-to-18.

[34] Online http://www.laseroptronic.it/doc/SR-800R.pdf.

[35] B. E. A. Saleh and M. C. Teich, *Fundamentals of photonics*. John Wiley & Sons Edition, 1991.

[36] C. C. Enz and G. C. Temes, "Circuit Techniques for Reducing the Effects of Op-Amp Imperfections: Autozeroing, Correlated Double Sampling, and Chopper Stabilization," *Proceedings of the IEEE*, vol. 84, no. 11, pp. 1584–1614, Nov. 1996.

[37] C. C. Enz, E. A. Vittoz, and F. Krummenacher, "A CMOS Chopper Amplifier," *IEEE Journal of Solid-State Circuits*, vol. 22, no. 3, pp. 335–342, June 1987.

[38] A. Bakker, K. Thiele, and J. H. Huijsing, "A CMOS Nested-Chopper Instrumentation Amplifier with 100-nV Offset," *IEEE Journal of Solid-State Circuits*, vol. 35, no. 12, pp. 1877–1883, Dec. 2000.

[39] C. Menolfi and Q. Huang, "A Low-Noise CMOS Instrumentation Amplifier for Thermoelectric Infrared Detectors," *IEEE Journal of Solid-State Circuits*, vol. 32, no. 7, July 1997.

[40] Q. Fan, J. H. Huijsing, and K. A. A. Makinwa, "A 21 nV/$\sqrt{Hz}$ Chopper-Stabilized Multi-Path Current-Feedback Instrumentation Amplifier with 2 μV Offset," *IEEE Journal of Solid-State Circuits*, vol. 47, no. 2, pp. 464–475, Feb. 2012.

[41] V. Ivanov and M. Shaik, "A 10MHz-Bandwidth 4μs-Large-Signal-Settling 6.5nV/$\sqrt{Hz}$-Noise 2μV-Offset Chopper Operational Amplifier," in *Proceedings of International Solid-State Circuit Conference 2016 (ISSCC)*, Feb. 2016.

[42] F. Butti, M. Piotto, and P. Bruschi, "A Chopper Instrumentation Amplifier With Input Resistance Boosting by Means of Synchronous Dynamic Element Matching," *IEEE Transactions on Circuits and Systems-I: Regular Papers*, vol. 64, no. 4, pp. 753–764, Apr. 2017.

[43] E. Moisello, M. Vaiana, M. E. Castagna, G. Bruno, E. Bonizzoni, and P. Malcovati, "A Chopper Interface Circuit for Thermopile-Based Thermal Sensors," in *Proceedings of International Symposium on Circuits and Systems (ISCAS 2019)*, May 2019.

[44] F. Maloberti, *Analog Design for CMOS VLSI Systems*. Kluwer Academic Publishers, 2001, pp. 234–235.

[45] Online https://uk.rs-online.com/web/p/enclosure-heating-elements/7256465/.

[46] A. Rogalski, *Infrared Detectors*. CRC Press, 2010.

[47] A. Zviagintsev, I. Bloom, I. Brouk, and Y. Nemirovsky, "Voltage and Current Integrated Readout for Uncooled Passive IR Sensors based on CMOS-SOI-NEMS Technology," in *Proceedings of IEEE* 28_{th} *Convention of Electrical and Electronics Engineers in Israel (IEEEI)*, Dec. 2014.

[48] A. Zviagintsev, T. Blank, S. Bar-Lev, I. Brouk, I. Bloom, and Y. Nemirovsky, "CMOS-SOI-NEMS Uncooled Infrared Presence Sensor," in *Proceedings of 2016 IEEE International Conference on the Science of Electrical Engineering (ICSEE)*, Nov. 2016.

[49] T. Saraf, I. Brouk, S. Bar-Lev, A. Unikovsky, T. Blank, P. K. Radhakrishnan, and Y. Nemirovsky, "CMOS-SOI-MEMS Uncooled Infrared Security Sensor with Integrated Readout," *Journal of the Electron Devices Society*, vol. 4, no. 3, pp. 155–162, May 2016.

[50] Online https://eoc-inc.com/wp-content/uploads/2019/06/JSIR350-4-AL-R-D6.0-0-0.pdf.

[51] F. Geusa, A. Agnes, and F. Maloberti, "Use of chopper-notch modulator in chopper amplifiers for replica images cancellation," in *Proceedings of*

2008 IEEE International Conference on Electronics, Circuits and Systems (ICECS), Nov. 2008.